Propriétés statistiques des AGN de faibles luminosités

Isabelle Gavignaud

UNIVERSITÉ TOULOUSE III – PAUL SABATIER

U.F.R. PHYSIQUE CHIMIE AUTOMATIQUE

THÈSE

pour obtenir le grade de

DOCTEUR DE L'UNIVERSITÉ TOULOUSE III
(SCIENCES)

Discipline : Astrophysique

par

Isabelle JARRY GAVIGNAUD

Propriétés statistiques des AGN de faibles luminosités

Soutenue le 25 Septembre 2006 devant le Jury :

Pr Alain Blanchard ..... Président
Pr Lutz Wisotzki ..... Rapporteur
Dr Guy Mathez ..... Directeur de thèse
Dr Palle Møller ..... Co-directeur de thèse

Laboratoire d'Astrophysique de Toulouse et de Tarbes – UMR 5572
Observatoire Midi–Pyrénées
14, avenue Edouard Belin
31400 Toulouse
FRANCE

Contents

List of Tables

List of Figures

Acknowledgement

My deepest personal thanks go to Guy Mathez, who introduced me to the fascinating universe of quasars and who assisted me through the ph.D. project despite the distance with a never failing attention, patience and enthusiasm.

I would like as well to express my gratitude to Palle Møller, who accepted to co-supervise my ph.D. since my arrival at ESO Garching in July 2003. His support as well as his curiosity and self-questioning approach have been very constructive for me. I enjoyed the TGIF (Thank God It's Friday) meetings and the traditional Beer Garden session following proposal deadlines.

I would like to acknowledge ESO for granting my ph.D. studentship. I take the opportunity to thank Danielle Alloin, Bruno Leibundgut and Markus Kissler Patig who were and are conferring to ESO students all possible support for their success.

The sample of AGN I used for this work is issued from the impressive effort of the VIRMOS consortium whose PI is Olivier Le Fèvre. It was a very nice opportunity for me to be part of the VVDS collaboration. Many thanks in particular to Angela Bongiorno for her contribution in the work presented here and in our publication. My visits in Bologna were very fruitful in ideas and learning thanks to the remarks and suggestions of Gianni Zamorani. Stephane Paltani contributed as well to the work presented here, providing in particular simulated spectra of QSO. Thank you to Fabrice Lamareille for replacing me in our observing run in Paranal (I greatly recommend the clever perl scripts available on his web page!). Merci to Jean-Pierre Picat for his help on various occasions. From Toulouse, I would like to thank as well Thierry Contini and Roser Pelló.

Thanks to J-G Cuby for passing some of his experience on observing skills and data reduction during his supervision of my voluntary service at the Paranal observatory. In the mountain, I particularly enjoyed working with Pedro Mardones and Sylvain Rondi.

On a more general point of view it is a very long list of persons which supported me during the ph.D. period in Toulouse, Santiago, Garching and finally Potsdam. I apologize in advance for all the persons which I will inevitably forgot to mention, here.

Thank you to Andreas Jaunsen who supervised me at the beginning of the ph.D.

Merci to Cedric Ledoux and Dominique Sluze for interesting discussion. I had great office mates, namely Audrey Delsanti and Giancarlo Pace. I am please now to to share the room SH-207 with Anne-Katharina Jappsen and Spyrios Kitsionas.

In would like to thank Marie Lemoine-Busserole, Marceau Limousin and Virginie Sellet, Mickaël Bazot, Françoise Delplancke and Cécile Faure for their hospitality. Thanks to Petra Nass, Terge Patig, Claire Vetter and Céline Koller for their spontaneous help concerning everyday-life matters in a country where I arrived with no linguistic knowledge.

Many thanks to Thomas, my family and close friends for their constant love and support. In particular, merci to Claire and Jocelyne for their help in correcting my spelling in the french summaries.

A special thanks goes to Asmus Böhm and Spyrios Kitsionas for a carefull reading of this manuscript. At last, I would like to thanks Suzy Collin as well as the two referees of this manuscript, L. Wisotzki and S. Cristiani for their interesting suggestions.

I am looking forward to pursue my research in the emulating working ambient of the galaxy group at AIP.

Je dédicace ce travail à Pierre et Monique Gavignaud, hélas, brutalement et récemment disparus. Je les remercie pour m'avoir fait découvrir les bonnes choses du Sud-ouest comme la chasse aux pradelous, la saison des responchous ou les artichauts au foie salé. Je les remercie aussi pour m'avoir toujours soutenue au cours de mes études. Ils aimaient tous deux la poèsie et pour cette raison je joins ici quelques vers:

Pour avoir mis le pied
Sur le cœur de la nuit
Je suis un homme pris
Dans les rets étoilés.

J'ignore le repos
Que connaissent les hommes
Et même mon sommeil
Est dévoré de ciel.

J. Supervielle

Introduction

Today, to a wide consensus, the Active Galactic Nuclei (AGN) phenomenon is considered to be the manifestation of accretion of matter onto super-massive black holes (SMBHs). However AGN can be as well defined in a more cautious way, as referring to energetic phenomena in the central regions of galaxies which are not attributed to stellar activity.

The following introduction will first summarize the principal observational characteristics which are usually present in the objects classified as AGN, the interpretation given to them and the different selection techniques characterizing AGN surveys. It will then explain the purpose of the work presented here.

1.1 The main classes of AGN

Different sub-classes of objects are regrouped in the family of AGN: quasars, QSOs, Seyfert galaxies, LINERS, BL Lac objects, etc ... The existence of these different names is reflecting the history of AGN discovery rather than a necessary difference in the physical nature of these sub-classes of objects. For this reason, I present here a brief historical summary of the AGN study before presenting the main class of AGN.

1.1.1 Short historic

Seyfert galaxies

Although being a low luminosity class of AGN, Seyfert galaxies were the first to be discovered. It seems that the first AGN spectrum to be taken was, in 1908, the one of the "spiral nebula" NGC 1068. It was noticed to have strong resolved emission lines (Fath 1908; Slipher 1917). But it was Seyfert (1943) who realized first that they were a special class of galaxies presenting an unresolved central bright core with spectra dominated by high excitation nuclear emission lines. Khachikian & Weedman (1974) defined two sub-classes of Seyfert galaxies from their spectral properties: ``[...]The Seyfert galaxies are either in class 1,

in which the Balmer lines are broader than the forbidden lines, or class 2, in which the forbidden lines and Balmer lines are the same width [...]'' This definition is now generalized to permitted emission lines in comparison to forbidden emission lines.

Quasars and QSOs

If the most luminous class of AGN, formed by Quasars and QSOs, has only been discovered 40 years ago, it is because these objects are rare and appeared in direct images to be normal stars, until some of them where remarked as being radio sources.

In the 50s, with the development of the radio techniques a new observational window opened itself to astronomers. Most of the detected radio sources at high Galactic latitude were associated with galaxies. Using interferometric techniques, Matthews & Sandage (1963) reported the first unambiguous coincidence of the radio source 3C 48 with a stellar like object. However they did not find an interpretation for the strange spectrum they obtained. A few months later, Schmidt (1963) identified the emission lines of another stellar-like radio source, 3C 273, with the Hydrogen Balmer series, redshifted by $z = 0.16$. He concluded that this object was either a star with a high gravitational redshift, or an extra-galactic object with a large cosmological redshift. It was then possible to identify the emission lines seen in the spectrum of 3C 48 and to measure its redshift of 0.37. The distance corresponding to this considerable redshift implies a luminosity which is ~ 100 times larger than that of a bright spiral galaxy. Particular attention was immediately drawn to these conclusions and other similar objects were quickly found. Since the physical nature of these objects was not understood, they where called 'quasi-stellar radio sources', which was shortened to 'quasars'. It was realized later – by applying other selection techniques – that most of the objects of this class did not have high radio luminosities. For this reason, the term QSO, standing for 'Quasi-stellar object' was introduced. Nowadays, both terms are in general used regardless of the radio-loudness of these objects or of their morphology.

1.1.2 Nomenclature

Seyfert, Quasars and QSOs

In fact, the only difference between a quasar and a Seyfert galaxy is the luminosity contrast between the compact central source and its host galaxy. As previously reviewed, historically, the appearance of quasars did not suggest identification with galaxies, since only the non-resolved nuclear source was detected. This morphological property (point-like object) has been later used as a selection criterion to find quasars, contributing hence in leaving a large luminosity gap between Seyfert galaxies and quasars. Nowadays both ground based and HST surveys have shown that all quasars with redshift up to 0.5 are embedded in the nucleus of a galaxy (Floyd et al. 2004) and it is clearly established from the similarity of their spectra and of most of their properties which vary continuously from the faintest Seyfert

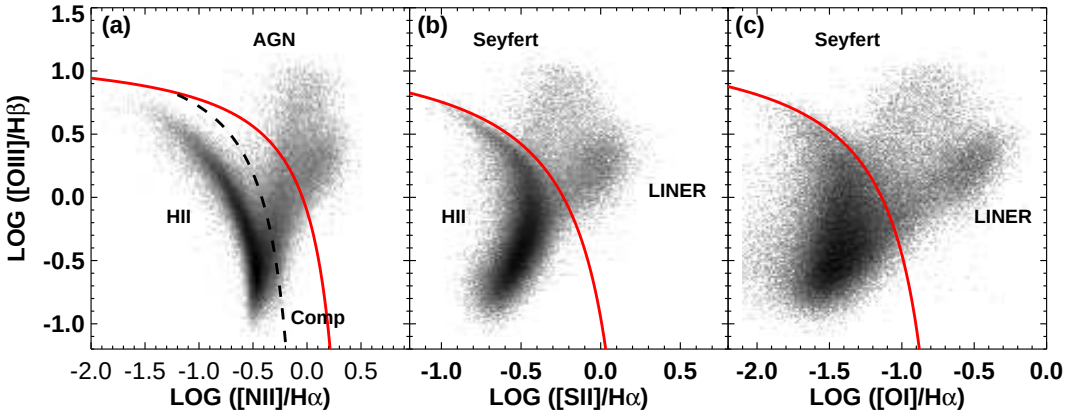

Figure 1.1: Example of diagnostic BPT diagrams for galaxies of the Sloan Digital Sky Survey (Source: Kewley et al. 2006Figure 1).

galaxies to the most luminous quasars that Seyfert galaxies and quasars form a single class of objects.

Traditionnally, following Schmidt & Green (1983), objects with $M_B < -23$ are referred to as quasars or QSOs, while objects with $M_B > -23$ are referred to as Seyfert galaxies.

There are two main classes of Seyfert galaxies and QSOs. The first one, called hereafter type-1 AGN, has two distinct sets of emission lines: one set of lines – referred to as "broad emission lines"– corresponds to permitted atomic transitions and has width of several thousands $\mathrm{km\,s^{-1}}$; the other set of lines –referred to as "narrow emission lines"– correspond to forbidden atomic transitions which have widths of a few hundreds $\mathrm{km\,s^{-1}}$. In the second class, called type-2 AGN, both permitted and forbidden lines are "narrow". Type-1 AGN exhibit a continuum emission which can be well approximated by a power law spectrum but type-2 AGN continua are very faint in the optical wavelength and are dominated by the stellar emission of their host galaxy. For this reason, in optical spectroscopy, one needs to compare the intensity ratio of two pairs of emission lines in order to distinguish type-2 AGN from normal HII regions. Such diagnostic diagrams are referred to as 'BPT' diagrams from Baldwin, Phillips, & Terlevich (1981).

There are examples of AGN with intermediate type where a weak broad-line component is detected underneath prominent narrow lines. A classification scheme was proposed by Osterbrock (1981).

A sub-group of type-1 AGN (10 to 20%) are observed to have broad absorption lines blueward of the emission redshift and are characterized by outflow velocities reaching up to 60 000 $\mathrm{km\,s^{-1}}$. They are referred to as Broad Absorption Line QSOs (BAL QSOs).

The work presented in this thesis is based on a type-1 AGN survey. This is as well the case of most of the studies I will mention in this introduction. For this reason, I will often use the terms "type-1 AGN", "QSO" or "broad line AGN" rather then the more general "AGN" term.

LINERs

"Low-ionization nuclear emission-line region galaxies" or LINERs form a very common class of AGN with very low nuclear luminosities. They might be present in almost half of nearby spiral galaxies (Ho et al. 1994). As Seyfert-2 galaxies, they have narrow emission lines; but relatively strong low-ionization lines, and can be distinguished from HII regions and Seyfert-2 with a BPT diagram. Figure 1.1 gives an example of such diagrams.

OVVs, BL Lac Objects and Blazars:

Optically Violent Variables (OVVs) form a subset of AGN with large flux variability ($\sim 10\%$) within a few days. OVVs are often highly polarized objects. These properties are shared by another class of AGN called "BL Lacertae" (BL Lac) objects which are distinguished by the absence of strong emission or absorption lines in their spectra. OVVs and BL Lacs are referred to as "Blazars" and they are all found to be strong and variable radio sources.

Radio Galaxies:

Strong extragalactic radio sources, if not quasars, are typically identified with giant elliptical galaxies. Some of these objects show emission lines from the nuclear region indicating AGN activity. Analogous to the situation with Seyfert galaxies they come in two types; broad-line radio galaxies (BLRGs) and narrow-line radio galaxies (NLRGs). These can generally be considered to be radio-loud type 1 and type 2 Seyfert galaxies, except that they are not found in spirals like most Seyfert.

X-ray Bright Optically Normal Galaxies (XBONGs):

Recent X-ray surveys unveiled a class of X-ray-bright galaxies which do not show evidence of AGN activity in their optical spectrum. These objects have a large X-ray to optical ratio and a hard X-ray spectrum which excludes X-ray binaries or hot gas as being the X-ray powering sources (Fiore et al. 2000; Hornschemeier et al. 2001; Barger et al. 2001). This category of objects is of particular interest since they constitute a large fraction of the X-ray point-like population ($\sim 50\%$ of the $S_{2-8KeV} > 10^{-15}\mathrm{ergs\,cm^{-2}\,s^{-1}}$) and might contain the population of obscured AGN needed to model the X-ray background (Comastri et al. 2002).

1.2 Observational properties

1.2.1 Small angular size

One of the most striking properties of AGN, is their very small apparent angular size which remains in general unresolved. This is a first indicator of small physical size of the AGN region.

More precisely, this point-like aspect depends on the luminosity contrast of the AGN over its host galaxy and of the observed wavelength. Radio-loud AGN, in addition to an unresolved compact source have often bright extended lobes which can exceed the size of the host galaxy by significant factors. In optical wavelengths, the narrow emission lines region (NLR) of close-by AGN can be resolved and corresponds to a scale of ~ 100 parsecs.

1.2.2 Variability

Flux variability is seen across the entire observable electromagnetic spectrum of AGN on time-scales from minutes[1] to years (Krolik et al. 1991; Edelson et al. 1996). In general, brightness levels slowly increase and decrease in an irregular, non-periodic fashion, with typical flux variations of $\sim 10\%$ on the scale of years. Superimposed on this variation there can be occasional outbursts of varying durations and magnitudes.

Major efforts to study the variability of QSOs, at optical wavelength, pinned down a complex set of correlations with different parameters (luminosity, rest-frame wavelength, redshift, etc ...). Those trends are potential tools to constrain or rule out AGN theoretical models (e.g. Cristiani et al. 1996; Kawaguchi et al. 1998; Vanden Berk et al. 2004, see Helfand et al. 2001 for a review).

More specifically, variability is used to probe the size of unresolved inner regions of AGN: since some AGN are variable over a few-days period, their size can not exceed a few light-days. It is also observed that the broad emission-line fluxes vary with the continuum flux, but with a short time delay (some weeks), whereas the narrow emission-line fluxes do not vary on short time scales. From this it can be inferred that the broad emission lines region (BLR) is a fairly small region of gas which is photoionionized and optically thick to ionizing continuum radiation. At the contrary, the narrow line emission comes from clouds of gas diluting and blurring the continuum variations over large volumes and large recombination timescales.

1.2.3 Radio emission

The radio properties of AGN can be markedly different from one object to the other. Strittmatter et al. (1980) found in the case of QSOs a dichotomy between radio-loud and radio-weak QSOs which was confirmed later by various studies (Kellermann et al. 1989; Miller et al. 1993). This dichotomy could not be explained by a single orientation-based scheme (see 1.3.2). QSOs were then defined as "radio-loud" when their radio-to-optical flux ratio, R, was exceeding a certain value (e.g $R > 10$, Kellermann et al. 1989). The remaining objects are qualified as "radio-quiet". Only 10 to 20% of type-1 AGN are radio-loud. Radio-quiet QSOs are associated with weak diffuse emission while Radio-loud QSOs are of two kinds: flat-spectrum core-dominated sources or steep-spectrum lobe-dominated sources (Miller et al. 1993; Kellermann et al. 1994).

However, there is still a controversy in the literature about the existence of a bimodality in the distribution of radio loudness of QSOs: while Ivezić et al. (2002),

[1] This is only true the X-ray range.

based on the deep radio survey FIRST (Becker et al. 1995) combined with the large optical SDSS surveys, found evidence for a "radio-loud"/"radio-quiet" dichotomy, White et al. (2000), based on the FBQS survey, and Cirasuolo et al. (2003), based on a merged set of QSOs surveys, found a population of radio-intermediate QSOs which suggests that this dichotomy has been overestimated or even does not exists.

1.2.4 Other properties

Apart from being unresolved variable sources, AGN are characterized by a wide spectral range of emission, from the radio to the γ-ray. All AGN seems to be infrared and hard X-ray emitters.

One can as well quote that the optical polarization of QSOs is in general higher than the one observed in stars (from 0.5 to 2%).

1.3 The actual paradigm

1.3.1 Accretion onto a super-massive black hole

The most generally admitted interpretation given to the mechanism behind this huge wealth of energy (up to 10^{48} erg s^{-1}) emitted from such a small volume (a few parsecs) is accretion on to a super-massive black hole (SMBH) and liberation of the gravitational energy associated with the infalling matter through dissipative processes (Zel'Dovich & Novikov 1964; Salpeter 1964; Lynden-Bell 1969; Rees 1984).

Since the gravitational force applied on the gas falling onto the central engine has to be larger or equal than the radiative pressure, one can link the luminosity L emitted by the central engine to its mass M. Under the hypothesis of a spherical symmetry:

$$\frac{L\sigma_e}{4\pi c r^2} \leq \frac{GMm_p}{r^2} \tag{1.1}$$

where σ_e is the Thomson cross section and m_p the proton mass. One can see that this relation is independent of the last parameter r, standing for the distance to the central mass M.

From relation 1.1, a lower limit on the mass of the hypothetical SMBH is obtained considering that the AGN is emitting light at the Eddington limit, i.e. the limit where the radiative pressure is balancing the gravitational potential:

$$M \geq 8 \times 10^5 L_{44} M_\odot \tag{1.2}$$

where L_{44} is the luminosity in units for 10^{44} erg.s^{-1}, typical for a luminous Seyfert galaxy.

A further evidence supporting this interpretation is that SMBH are possibly ubiquitously present in the centers of galaxies. The observational evidence for this is mostly based on gas and stellar kinematics of close-by galactic cores which imply large amounts of non-luminous mass ($10^6 - 10^9 \mathrm{M}\odot$) concentrated in parsec-sized volumes (Richstone et al. 1998).

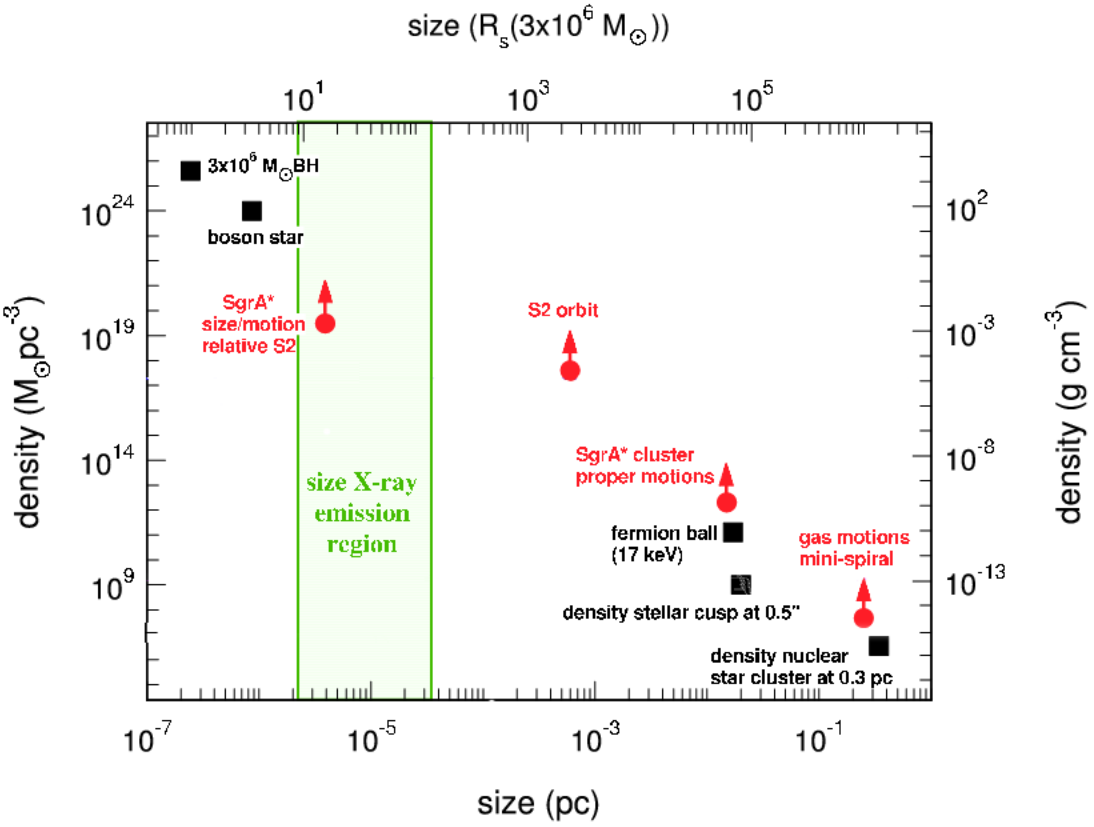

Figure 1.2: Constraints on the nature of the observed dark mass in the Galactic Center (Schödel et al. 2003, Figure 12). The horizontal axis is the size, and the vertical axis the density. Filled circles denote the various limits on the size/density of the dark mass derived from kinematical studies discussed in Schödel et al. (2003) and the grey shaded area marks the constraints on the size of the variable X-ray emission from Baganoff et al. (2001). Large filled squares mark the location of different physical interpretation to the central object. The up-to-date available measurements exclude all configurations but those of a black hole and a boson star.

The Milky Way itself contains such a "dark" object coinciding with the radio and X-ray source Sagittarius A*. The tight constraints of the mass distribution of the galactic center given from the orbit of individual stars close to it (Schödel et al. 2002) and the size of its variable X-ray emission (Baganoff et al. 2001) exclude most of the interpretation for the nature of this objects alternative to the SMBH hypothesis (see Figure 1.2).

The Milky Way however, and most galaxies, do not show significant nuclear activity. This has raised the idea that AGN might be a temporary phenomena ignited at certain times when the central SMBH of a galaxy get fuelled. It is not clear which event would dominate this triggering of AGN: major or minor galaxy mergers? galaxy-galaxy interaction? some inflow process intrinsic to a galaxy? In fact the way in which a highly luminous AGN (e.g. QSO) can be activated probably differs from the way in which a faint AGN (e.g. LINERs) is initiated.

1.3.2 The unified model

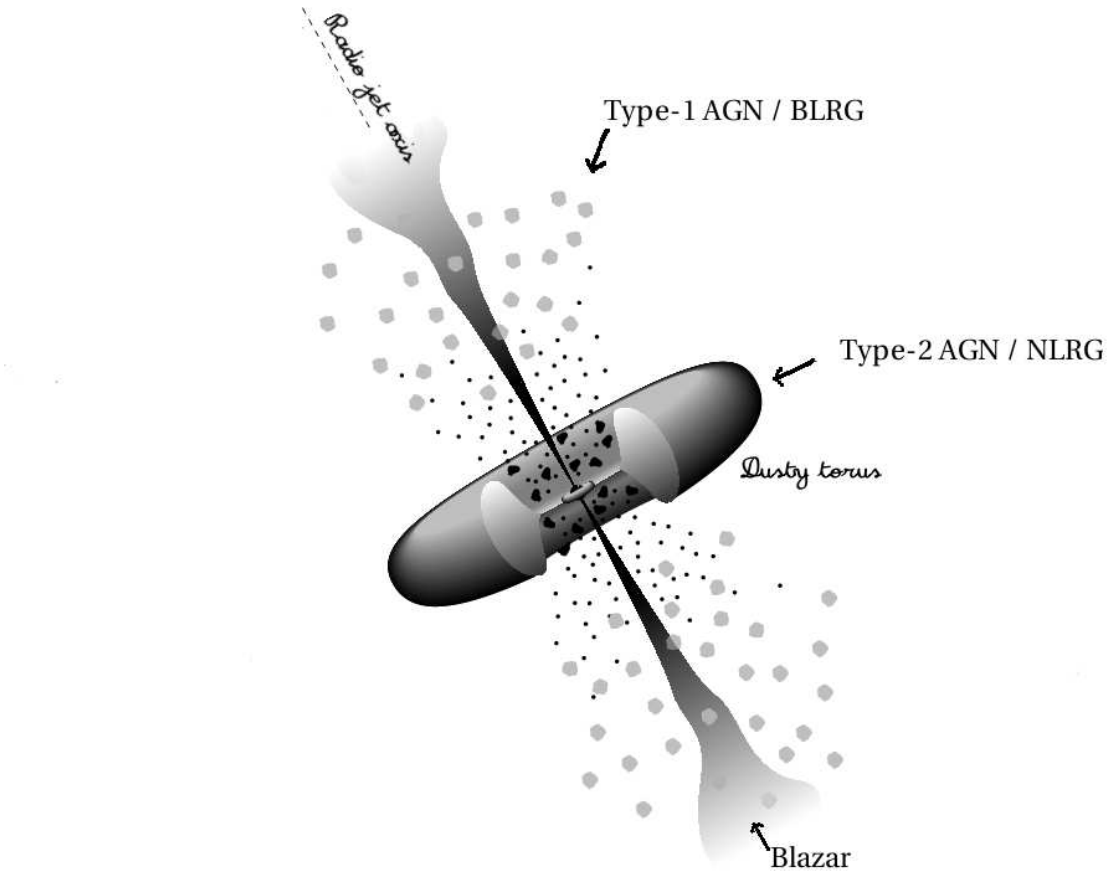

Figure 1.3: Sketch of the unified model in the case of radio-loud AGN (Urry & Padovani 1995). In this scenario a dusty torus is surrounding the broad line region. For an observer looking at the AGN in the plane of the torus, the continuum emission produced by the accretion disk and the broad emission lines coming from dense gas clouds close to the SMBH ($\sim 0.03 - 0.3$ pc), are obscured. Narrow emission lines are emitted from low density clouds ionized by the central source at much larger distances (~ 100 pc) and remain visible in all orientations. Blazars are interpreted as AGN observed from a line of sight close to the radio jet axis. In the case of radio-quiet AGN, the radio jet would be absent.

As reviewed in section 1.1, there is a large variety of AGN phenomena with some overlapping properties. If the same physical process is at work in all of them, the various classes of AGN might only be the result of observational effects.

Although different unification schemes were explored, the actual standard model explains how the different classes of observed AGN can be produced by the same physical object viewed from different angles (Antonucci 1993; Urry & Padovani 1995). In this scenario, there are only two distinct classes of AGN: radio-loud and radio-quiet AGN. Figure 1.3 gives an outline of this model. The basic idea is that the continuum and broad-line emission component of the AGN can or not be obscured by dust depending on the relative orientation of the observer to the accretion disk. The absorbing dust component is in general assumed to form a torus surrounding

the accretion disk and the broad line emission region on a parsec scale. Narrow emission lines are emitted on a much larger scale ($\sim$ 100 pc) and therefore remain visible in all orientations. AGN observed with the accretion disk and BLR obscured by the dust torus will then be seen as type-2, while the ones with a non-obscured accretion disk will be seen as type-1. The large flux and polarization variability of blazars can be interpreted by this scenario, considering that we observe the object close to the axis of the radio jet.

Spectropolarimetry has played an important role in establishing this unified picture: some type-2 AGN were revealed as type-1 AGN when observed in polarized light. This is attributed to scattering of broad-line emission above the poles of the dust torus (e.g. Antonucci 1982; Antonucci & Miller 1985).

The first observation of an AGN with a spatial resolution close to the size of the torus inferred by the models, was recently given by the interferometric mid-infrared observation of NGC 1068's central AGN (Jaffe et al. 2004). These observations reveal a well-resolved warm-dust (320K) structure of the scale of $\sim$3 parsecs surrounding a hot structure (800 K) of 0.7 parsec. However, a much better resolution is still required to distinguish between the heuristic homogeneous torus model from a patchy structure formed by individual clouds that would be needed to explain the dust temperature derived from these observations (Elitzur 2005).

1.4 AGN selection techniques

Determining the properties of the AGN population as a function of redshift requires large and unbiased samples.

The first difficulty for building such catalogs is that AGN are faint and –if one excludes the local LINERS– AGN are rare: at optical wavelengths QSOs constitute only $\sim$1% of the faint population of sources.

For this reason it is necessary to pre-select AGN candidates and make a compromise between a certain preselection efficiency and completeness rate. The efficiency being the fraction of bona fide AGN inside the AGN candidate catalogs and the completeness being the fraction of AGN full-filling the selection prerequisites.

It is important to realize as well that AGN are observed in a large variety of forms, connected by a complex set of overlapping properties. It is therefore not possible to make a census of the complete AGN population in a single homogeneous survey. Obviously the different survey described hereafter are focusing on specific sub-classes of the AGN population. In particular most of them –and this is aswell the case of this thesis– are QSOs surveys.

Before describing some of the main AGN selection techniques, we can remark that the number of known AGN exponentially increased in the recent years, as is illustrated for QSOs in Figure 1.4. Table 1.1 lists some examples of recent AGN surveys for which different selection techniques are used.

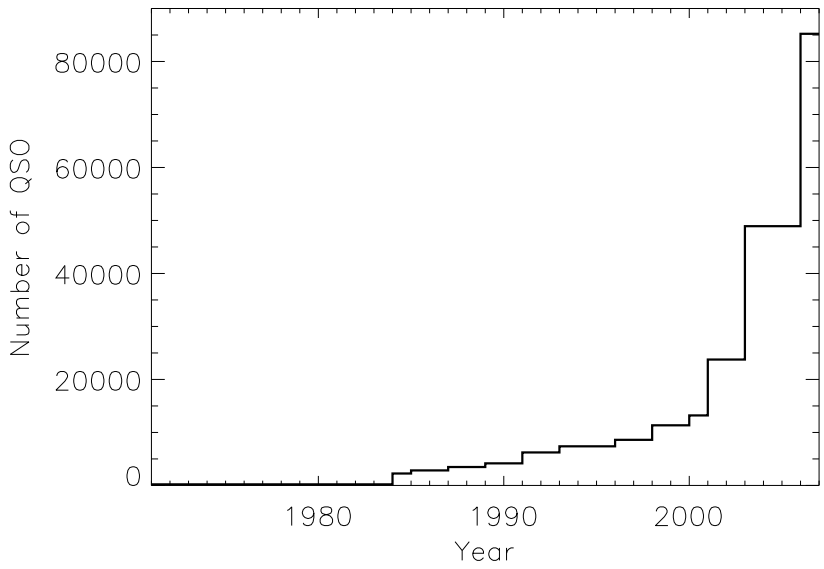

Figure 1.4: Evolution of the number of QSOs published in the Véron & Véron catalog (Veron-Cetty & Veron 2006).

1.4.1 Optical surveys

Multicolor Techniques

In general, QSOs surveys are pre-selecting their candidates with the UV excess technique: quasars are brighter in the ultra-violet than most stars. Combined with a morphological preselection of non-resolved objects, this is the most efficient way to build large samples of QSOs (hereafter UVX). The Two-Degree Field QSO Redshift survey (2Qz) is the largest UV-excess-selected survey, with an efficiency above 50% (Croom et al. 2004). It contains $\sim$ 20000 spectrocopically confirmed QSOs and is the second larger QSOs sample after the SDSS quasar sample (see Table 1.1). The drawback of this technique is a bias at low redshift against the objects for which the host galaxy is detected and resolved. Furthermore, this technique is not able to select QSOs with redshift larger than 2.3 as the Lyman alpha line is shifted out of the UV passband.

Multi-color techniques are now used to overcome this limitation and isolate QSOs from starlight-dominated objects. The currently largest QSO survey, the SDSS QSO survey, desmonstrates the high efficiency of this multi-color preselection [2].

Higher redshift QSOs ($z \gtrsim 5.7$) are targeted by dedicated surveys using near-IR wavelengths (Fan et al. 2006).

To probe the faintest magnitude the COMBO-17 project identifies AGN based on the photometry in a set of 17 filters (Wolf et al. 2003). The spectral-energy-distribution fitting technique developed by this team leads to a good redshift accuracy ($\Delta z \sim 0.03$) without the necessity of spectroscopic follow-up, at the price of a

[2]The complex selection algorithm of the SDSS is mostly based on a multi-color photometric catalog but takes into account radio emission and morphology as well.

small fraction of wrong identification and 'catastrophic' redshift measurements.

In general, QSOs with peculiar spectral energy distributions (SED) will tend to be under-sampled in color selected surveys. This might be the case of BAL QSOs, heavily dust-reddened QSOs or Seyfert-1 galaxies contaminated by their host light contribution.

Slitless spectroscopic survey

Due to their non-stellar continuum and jutting broad emission lines, type-1 AGN can be efficiently selected from slitless spectroscopic surveys as demonstrated by the pioneer work of Markarian (1967) and Smith (1975). Two recent illustrations of this technique are the Large Bright Quasar survey (LBQS, Hewett et al. 1995) and the Hamburg/ESO Survey (HES, Wisotzki et al. 2000).

At the contrary of the UV-excess technique, slitless spectroscopy has the advantage of being very efficient for redshift larger than 2, via the detection of the strong CIV and Lyα emission lines.

Most of slitless spectroscopic surveys are combining two complementary selection techniques: (1) identification of objects with a blue spectral continuum; (2) identification of emission line objects; This results in a completness function which is not varying dramatically with redshift as in the case of UVX selection.

These advantages lead Osmer (1982) to recognize the evidence for a decrease in the space density of quasars at redshifts larger than 3.5.

Another major reward of this technique is its ability to select groups of quasars or lensed quasars, since all observed objects in the field have a spectrum.

A bias can result from the fact that there is no clear limiting magnitude for the detection of emission lines: strong emission lines can be identified in very faint objects. This can be resolved by imposing aposteriori a limiting magnitude from a broad band image. Special care needs also to be taken to avoid confusions in the case of superimposed spectra. In any case, the main limiting factor of slitless spectroscopy is the fact that the sky is integrated over the entire field of view. For this reason, it is crutial to avoid the bright sky emission lines and the spectral range in those survey is volontary limited to $\lambda \lesssim 5500\,\text{Å}$.

Variability and zero proper motion

Since:

1. It seems that –if observed on the scale of a few years– all QSOs are variable with time;

2. QSOs can be distinguished from galactic stars from their lack of proper motion;

variability and zero proper motion, are two alternatives methods to select QSOs.

Although they are expensive in terms of observing time, they carry a strong case: they might lead to the selection of QSOs that would have been missed by other selection criteria, giving thereby an independent handle on their completeness function.

These criteria can complement the traditional UVX techniques to select AGN in crowded stellar fields. In general, these two selection methods are in general combined with other selection criteria (e.g. Cimatti et al. 1993; Brunzendorf & Meusinger 2002; Rengstorf et al. 2004).

Optical selection of type 2 AGN

Because of their possible confusion with star forming regions, type-2 AGN are more difficult to select than type 1 AGN in the optical wavelengths. However, Djorgovski et al. (2001) could select some type 2 quasars as color outliers in the Digital Palomar Observatory Sky Survey. Zakamska et al. (2003), used the spectrocopic data of the SDSS survey to select 291 type 2 AGNs at redshifts $0.3 < z < 0.83$, on the basis of their emission-line properties.

1.4.2 The puzzle of X-ray surveys

It was already observed 30 years ago (see for example Tananbaum et al. 1979) that quasars are strong X-ray emitters and that they contribute significantly to the cosmic X-ray background (CXRB) discovered by Giacconi et al. (1962).

In fact, X-ray emission might be the most common and distinctive feature of AGN. But owing to technical challenges, X-ray space missions did not have, until recently, the sensitivity and spatial resolution needed to conduct surveys of AGN.

Thanks to ROSAT, and more recently to the Chandra and XMM missions, the selection of AGN in the soft 0.5-2 keV band yield the highest surface densities of AGN in all wavelengths and techniques (Miyaji et al. 2000; Hasinger et al. 2005).

A major advantage forseen for X-ray selected samples is their ability to select at the same time type-1 AGN and type-2 AGN.

In the framework of the unified AGN scheme presented Section 1.3.2, constraining the ratio of type-2 to type-1 AGN is of great interest: to reproduce the observed CXRB, and in particular its observed hard X-ray peak at $\sim$ 30 KeV, from the population synthesis of obscured and non-obscured AGN, one needs to invoke a ratio of type-2 to type-1 AGN as large as 4:1. In particular, one expects to find a substantial population of luminous type-2 AGN, so-called "type-2 quasars" or "type-2 QSO" (e.g. Gilli et al. 2001). Another requirement of these models, to conciliate the slope of the observed CXRB with the one of individual AGN, is to consider a peak of the redshift distribution for AGN at a redshift of $\sim$2, as observed in optical samples.

The resolved fraction of the 2-10 keV hard X-ray background with the Chandra Deep Field-North (CDFN Giacconi et al. 2002) and Chandra Deep Field South (CDFS Alexander et al. 2003) is as large as 85-90%, and intense effort of optical identification of these faint sources lead to samples of reasonable statistics with good completeness Hasinger et al. (2005). Despite this situation, the picture of the AGN population and evolution is not as clear as forseen.

The bulk of the X-ray selected AGN is found to be low redshift, even if one takes into consideration X-ray sources with no optical counterpart, this translates into

evidence for a luminosity dependent density evolution of AGN (Miyaji et al. 2000; Hasinger et al. 2005), contrasting with the pure luminosity evolution model which can describe optically-selected AGN LF.

It was a surprise to observe, how in the soft X-ray band 0.5-2 KeV, type-1 AGN constitute the major population of bright sources. Though, at fainter luminosities type-2 AGN constitute the main population (Barger et al. 2005).

Only a few examples of type-2 QSOs where uncovered by deep X-ray observation (e.g. Norman et al. 2002) but the large absorption column densities inferred for these objects ($N_H > 10^{23-24}$) makes them extremely difficult to detect or identify in soft X-ray surveys. Conveniently, this leave some room for the population of hidden extreme objects required by the background models.

To detect these "Compton thick" objects, Fiore et al. (1999) undertook a hard X-ray AGN selected survey the High Energy Large Area Survey (HELLAS).

1.4.3 Radio surveys

If radio observations led to the discovery of the first quasars, radio-selected quasar are quite expensive in term of telescope time: one needs a wide sky coverage with excellent positions. The two largest radio survey are the NRAO VLA Sky Survey (NVSS) and the Faint Images of the Radio Sky at Twenty-cm (FIRST) survey (Becker et al. 1995; Condon et al. 1998). The FIRST Bright Quasar Survey is a relatively large (~ 1000) quasar sample selected from the FIRST radio observations combined to Automated Plate Measuring Facility (APM) optical catalog.

A major advantage of the radio selection technique is that radio wavelenth are not affected by dust extinction. For this reason, the chalenge of constructing a complete radio selected sample free of optical color pre-selection was undertaken: an intense spectroscopic observational programme for 878 flat-spectrum radio sources selected from the Parkes catalogues yield a near-complete identification of these sources and allowed to constitute the Parkes quarter-Jansky (PQS) flat-spectrum sample: it comprises 379 QSOs of which 355 have measured redshifts (Jackson et al. 2002).

This survey found no evidence for a subsequent population of "red-quasar". But since the radio-loud quasars selected in this sample correspond only to 10-20% of the QSO population, this leaves room for the hard X-ray and infrared searches for those objects.

1.4.4 Infrared and mid-infrared selection

AGN show infrared (IR) excess and, as in the case of radio, selection of AGN in the infrared facilitates the discovery of sources whose optical emission is extinguished by dust.

The Spitzer mission is providing the possibility to select AGN from their mid-infrared emission (e.g. Lacy et al. 2004; Sajina et al. 2005). The first results suggest that indeed a significant population of obscured AGN is present and is partially missed in X-rays (Martínez-Sansigre et al. 2005; Treister et al. 2006).

Survey	Selection technique	Number of AGN$^{(*)}$	Limiting flux	Redshift range	Reference
2Qz	u, b_j, r + morphology	23 338	$b_j < 20.85$	$z \lesssim 2.3$	Croom et al. (2004)
SDSS	u, g, r, i, z + radio + morphology	76 483	$i^* < 19.1$ for $z \lesssim 3$ $i^* < 20.2$ for $z \gtrsim 3$	$z \lesssim 5.8$	Richards et al. (2002)
COMBO-17	SED fitting, 17 filters: UV to near-IR	192	$R < 24$	$1.2 < z < 4.8$	Wolf et al. (2003)
LBQS	SS: continuum + EL + morphology	1055	$B_J \lesssim 18.5$	$0.2 \leq z \leq 3.4$	Hewett et al. (1995)
HES	SS: continuum + EL	415	$B_J \lesssim 17.5$	$z < 3.2$	Wisotzki et al. (2000)
CFRS	I-band flux limited	6	$I_{AB} < 22.5$	$z < 5$	Schade et al. (1996)
VVDS	I-band flux limited I-band flux limited	56 74	$I_{AB} < 22.5$ $I_{AB} < 24$	$z < 5$ $z < 5$	Gavignaud et al. (2006)
CDFS-N CDFS-S	Soft X-ray	~ 400	$F_{0.5-2keV} > 3.10^{-14}$ ergs cm^{-2} s^{-1}	–	Alexander et al. (2003); Barger et al. (2003); Giacconi et al. (2002); Szokoly et al. (2004)
HELLAS	Hard X-ray	38	$F_{5-10keV} > 3.10^{-14}$ ergs cm^{-2} s^{-1}	–	Fiore et al. (1999); La Franca et al. (2002)
FBQS	radio + blue color + optical morphology	957	$S_{1.4GHz} \geq 1$ mJy, $R < 17.8$ and $R < 18.9$	$z < 4$	White et al. (2000); Becker et al. (2001)
PQJ	radio flat spectra	379	$S_{2.7GHz} \geq 0.25$ Jy	$z < 4$	Jackson et al. (2002)

(*) Number of AGN with an optical spectral identification (except in the case of COMBO-17 sample).
- **SS:** Slitless spectroscopy;
- **EL:** Emission lines.

Table 1.1: Example of recent AGN surveys, the VVDS AGN sample presented in this work is shaded in grey.

1.5 Some open questions

Many interesting question concerning AGN are open: how did the initial black hole seeds form? How did these seeds grow into the super-massive black holes observed in local galaxies? Which event triggers the AGN phenomena?

But interest for AGN is as well triggered by the important role that they are playing for their environment and describing AGN evolutionary history can provide fundamental insight into the theories of structure formation in the universe.

In particular, the discovery of a tight relation between black-holes mass and velocity dispersion of their host galaxy (Ferrarese & Merritt 2000; Gebhardt et al. 2000) suggests that AGN feed-back possibly regulate coeval black-hole growth and host galaxy evolution (e.g. Granato et al. 2004).

To trace AGN evolution it is fundamental to collect large samples of AGN as free as possible of selection effects and covering a large cosmic look-back time. This ph D explore various properties of an optical spectroscopic sample of AGN which meets these requirements. An other important characteristic of this sample is to have a very faint limiting flux. Previous to the proper ph.D. thesis work we will present the survey from which our data are selected. The first task of the ph.D, was to determine the selection function of this sample. The direct application of this study was to derive the surface density of AGN observed on the sky as a function of magnitude. We then interested ourselves to the redshift distribution, and to the morphological, color, and spectral properties of this sample. The preliminary results concerning the luminosity function of this sample are then briefly described.

1.6 Conventions

In this work, observed magnitudes are including correction for galactic extinction using the dust map provided by Schlegel et al. (1998).

Absolute magnitudes are computed from the observed I-band. The K-correction is computed considering the SED of the SDSS composite spectrum, except in the case of the luminosity function, in which the LBQS composite spectrum is considered.

A Hubble constant $H_0 = 70$ km s^{-1} Mpc^{-1} and a flat cosmology with $\Omega_M = 0.3$ and $\Omega_\Lambda = 0.7$ have been used throughout.

Dominant emission lines such as C IVλ1549, C III]λ1909, Mg IIλ2798, [O II]λ3727 or [O III]$\lambda\lambda$4959,5007 are plainly referred as C IV, C III], Mg II, [O II] or [O III] doublet.

Contexte scientifique

Il est aujourd'hui établi de façon consensuelle que le phénomène d'AGN est la manifestation qui résulte de l'accrétion de matière sur un trou noir super-massif (d'un million à plusieurs milliards de masses solaires) situé au centre d'une galaxie (Zel'Dovich & Novikov 1964; Salpeter 1964; Lynden-Bell 1969; Rees 1984).

Depuis la découverte au début des années soixante par Maarten Schmidt des quasars, forme la plus extrême de noyaux actifs de galaxies, ces objets, longtemps considérés commes rares et exotiques, ont suscité beaucoup d'intérêt.

On pense aujourd'hui, au contraire, que la plupart des galaxies, du moins celles qui contiennent une composante sphéroïdale, traversent au cours de leur formation plusieurs phases où leur trou noir central est nourri en gaz, déclenchant le phénomène d'AGN. L'intéraction au cours de ces phases entre l'AGN et sa galaxie hôte permettrait d'expliquer ainsi une croissance co-régulée entre trous-noirs et bulbes de galaxie comme le suggère les observations [3].

Il reste aujourd'hui un certain nombre d'interrogations : Comment ces trous noirs super-massifs se sont-ils formés et quelle évolution ont-ils suivi ? Par quel mécanisme ces trous-noirs et leurs galaxies hôtes s'influencent-ils mutuellement ? Au delà de la quête propre à la connaissance du phénomène d'AGN leur étude est également importante pour résoudre certains problèmes cosmologiques. Par exemple : quand et comment l'Univers s'est-il ré-ionisé ?

La réponse à ces différentes questions passe par l'étude statistique de ces objets et pour cette raison, il est nécessaire de constituer de grands échantillons qui soient, au mieux, représentatifs de la population sous-jacente des AGN.

Mais d'une part les AGN sont des objets faibles et rares, et d'autre part la spectroscopie est une étape indispensable pour confirmer leur nature : dans le cas des AGN de type-1, ils ne constituent qu'environ un pour cent des objets du ciel profond détectés en imagerie optique. Pour cette raison, il a été nécéssaire de développer des techniques de pré-sélection qui permettent d'isoler des candidats QSOs avant leur observation spectroscopique. La méthode la plus efficace, la pré-sélection de candidats par des critères de couleurs, a permis ces dernières années une augmentation sans précédent du nombre de QSO connus. Notamment, le SDSS (Richards et al. 2002) et le 2Qz (Croom et al. 2004) rassemblent chacun plusieurs dizaines de milliers de QSO et ont permis une étude détaillée des AGN de type-1.

Cependant ces études portent sur des objets relativement brillants, de plus, la pré-sélection de candidats QSO sur la base de leurs couleurs cause potentiellement un biais vers certains types de QSO, plus facilement sélectionnés que d'autres. En effet la complétude de ces échantillons, c'est à dire le ratio entre d'une part le nombre de candidats pré-sélectionnés et d'autre part la population des QSOs prise dans son ensemble, varie de façon complexe suivant le redshift (décalage cosmologique vers le rouge) considéré et la distribution spectrale d'énergie des QSOs considérés.

[3] En particulier, la corrélation observée localement entre la masse des trous noirs super massifs et la dispertion effective de vitesse stellaire (Ferrarese & Merritt 2000; Gebhardt et al. 2000) ou bien encore la corrélation entre la masse des trous noirs super massif et la masse lumineuse du bulbe galactique (Magorrian et al. 1998; McLure & Dunlop 2001; Marconi & Hunt 2003).

Dans ce contexte, l'échantillon d'AGN de type 1 issu du VIMOS-VLT Deep Survey (VVDS, Le Fèvre et al. 2005b) présente un intérêt unique, de part la simplicité des critères de pré-sélection de ces QSOs (une simple limite en magnitude) ainsi que par la profondeur en magnitude atteinte : il fournit d'une part un aperçu des propriétés des AGN de type 1 à des magnitudes encore peu explorées spectroscopiquement (les AGN étudiés ici sont jusqu'à cent fois plus faibles que ceux du SDSS) et il permet d'autre part de quantifier les biais qui seraient introduits par des critères classiques de sélection.

Avant d'entrer dans la description du travail propre à cette thèse nous décrivons dans un premier chapitre l'échantillon du VVDS à partir duquel nos données ont étés sélectionnées. La première réalisation du travail de doctorat a été de déterminer la fonction de sélection de cet échantillon. L'application directe de cette étude a été la mesure de la densité d'AGN projetée sur le ciel. Nous nous sommes ensuite intéressés à la distribution en redshift et aux propriétés morphologiques, de couleurs ainsi que spectrales de cet échantillon. Finalement, nous présentons les résultats préliminaires obtenus sur la fonction de luminosité et sur la nature des trous noirs galactiques de cet échantillon.

Chapter 2

The VIMOS VLT Deep Survey

2.1 Survey goals and strategy

The VIMOS VLT Deep Survey[1] (VVDS) is a survey aiming at studying the evolution of galaxies, large scale structures and AGN with a coherent approach, over a large volume and a large cosmic-time base.

It aims to be the complementary deep and high redshift counterpart of the massive efforts undertaken with the 2dF and Sloan surveys (Colless et al. 2001; Abazajian et al. 2003) which are mapping the distribution and establish the properties of several hundreds of thousands of galaxies in the local universe.

To reach its scientific goals the VVDS adopted the strategy of constructing a purely I-band magnitude limited spectroscopic sample obtained in a wide and in a deep survey. The absence of morphological pre-selection criteria aims at keeping QSOs and compact galaxies in the sample. Setting a magnitude limit obviously leads to a Malmquist bias, with increasingly luminous objects being selected towards higher redshifts. However, it allows to perform in a given volume of the universe a complete census of the galaxy or AGN population. The choice of the I-band selection was made to allow selection upon the flux emitted by the "old" stellar content at wavelengths longer than 4000Å up to $z \sim 1$. Above redshift 1, galaxies are selected from the rest-frame continuum emission at wavelengths shorter than 4000Å. In the case of QSO, this I-band selection is sensitive to objects with redshifts ranging from $z = 0$ up to $z \sim 5.5$. At higher redshifts the rest frame UV flux is strongly extinguished by the intergalactic medium, with the so-called Lyman alpha forest entering the observed I-band filter. To reduce the impact of cosmic variance, the *wide* survey is carried over 3 independent fields, VVDS-1003+01,VVDS-1400+05 and VVDS-2217+00. The *deep* survey is mainly carried out in VVDS-0226-04 and supplemented by an additional field in the Chadra Deep Field South, called hereafter VVDS-CDFS.

To obtain the required spectroscopic data the VVDS consortium has built the VIsible Multi Object Spectrograph (VIMOS) for the ESO-VLT Melipal Unit Tele-

[1] http://www.oamp.fr/virmos/vvds.htm

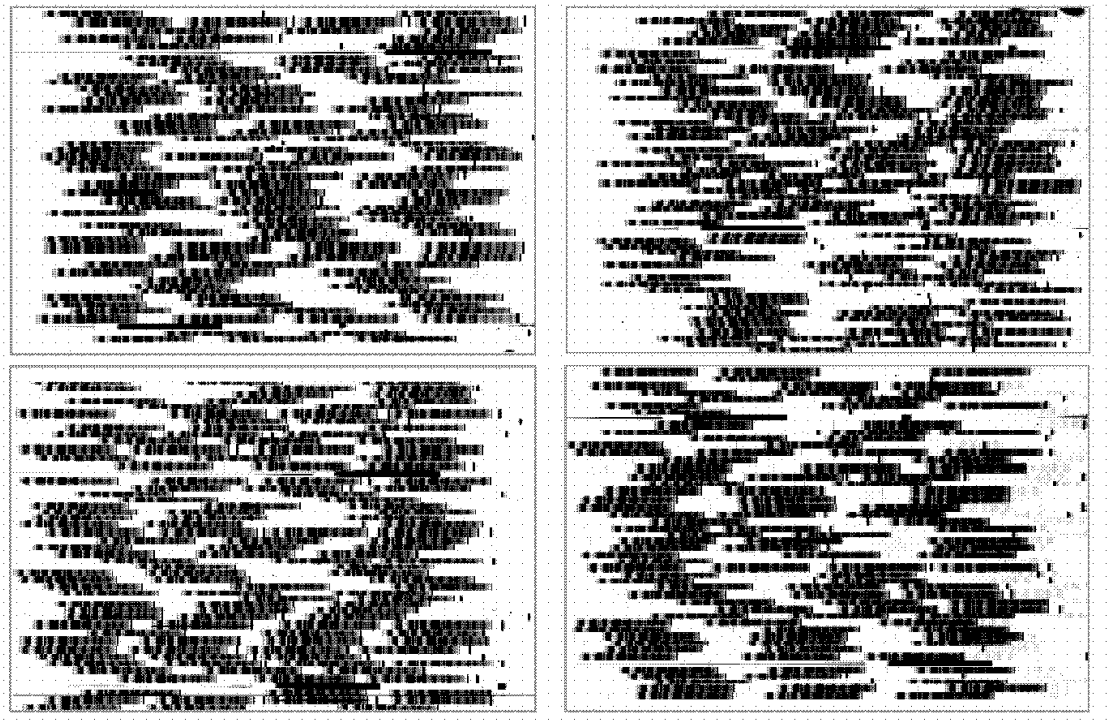

Figure 2.1: Typical layout of spectra in the 4 quadrants of a VVDS-Wide pointing; more than 550 are observed on average (Le Fèvre et al. 2005b)

scope (UT3). This instrument allows to observe with 600 slits simultaneously at a spectral resolution of $R \sim 230$ (see Figure 2.1). The data presented in this thesis were obtained during the Guaranteed Time Observations.

2.2 Observations and data reduction

The spectroscopic VVDS survey consists of the VVDS-deep, targeting objects in the range $I_{AB} = 17.5 - 24.0$, and the VVDS-wide, targeting objects in the range $I_{AB} = 17.5 - 22.5$.

The purely magnitude-limited selection of spectroscopic targets was carried out from a catalog based on deep photometry. This catalog is complete down to $I_{AB} = 25$ in all fields. In addition, deep multi-band photometry was obtained, providing comprehensive multi-wavelength information for the objects. The B, V, R, and I photometry was obtained on the full fields of view and U, K, and J in smaller areas. For a detailed description of the photometric catalog we refer the reader to Le Fèvre et al. (2004). A comprehensive description of the data reduction and final data quality of the deep imaging survey can be found in McCracken et al. (2003).

Spectroscopic observations were performed with the multi-object spectrograph VIMOS installed on Melipal (see Le Fèvre et al. 2003), the third 8-meter telescope at the Paranal Observatory. We present results based on the first spectroscopic runs only (Epoch One), obtained during October and November 2002. These observations

Table 2.1: Summary of the spectroscopic data available on VVDS first epoch fields.

Field	Mode	TSR*	N spectra	$\mathcal{A}^{**}$ [deg^2]
VVDS-0226-04	deep	25%	9622	0.48
VVDS-1003+01	wide	26%	2092	0.33
VVDS-2217+00	wide	22%	5651	0.81
VVDS-CDFS	deep	23%	1716	0.13

* Target sampling rate: fraction of objects in the photometric catalog inside our targeted area $\mathcal{A}$, which have been spectroscopically observed.

** Geometrical area in deg^2 of the spectroscopic first-epoch data that are used in this work (see Fig. 2.2).

and the reduction procedure are presented in detail in Le Fèvre et al. (2005b) for the deep survey and in Garilli et al. (2006) for the wide survey.

2.2.1 The VVDS multi-wavelength imaging survey

The wide and deep fields were imaged in four bands, B, V, R, and I. The wide photometric survey covers 12 deg^2 in three high-galactic latitude fields, each 2x2 deg^2: VVDS-1003+01, VVDS-1400+05, and VVDS-2217+00. The deep photometric survey covers a 1.3 x 1 deg area, VVDS-0226-04. Part of the deep field has been observed in additional bands: U (Radovich et al. 2004), J and K (Iovino et al. 2005), u^*,g',r',i',z' from the Canada-France-Hawaii Legacy Survey[2] (CFHTLS) , as well as in the infrared (3.6, 4.5, 5.8, 8 and 24 microns) with Spitzer-SWIRE IRAC (Lonsdale et al. 2003), in radio (1.4 GHz) on the VLA (Bondi et al. 2003), X-ray with XMM (Pierre et al. 2004), and UV (1500 and 2300Å) with GALEX (Morrissey et al. 2005; Arnouts et al. 2005; Schiminovich et al. 2005).

In order to minimize surface brightness selection biases down to the faintest required spectroscopic limit of $I_{AB} = 24$, the imaging survey was designed to be complete down to $I_{AB} = 25$ (see McCracken et al. 2003). The B, V, R, and I observations were performed from November 1999 to October 2000 at the 3.6 m Canada-France-Hawaii Telescope, with the CFH12K wide-field mosaic camera.

In addition to the VVDS fields, a deep spectroscopic survey was also performed in 0.13 deg^2 of the Chandra Deep Field South (CDFS) field and is included in this work. This field is based on the ESO Imaging Survey (EIS) I-band catalog described in Arnouts et al. (2001). The spectroscopic data available in the CDFS are public and are described in Le Fèvre et al. (2004).

[2]www.cfht.hawaii.edu/Science/CFHLS

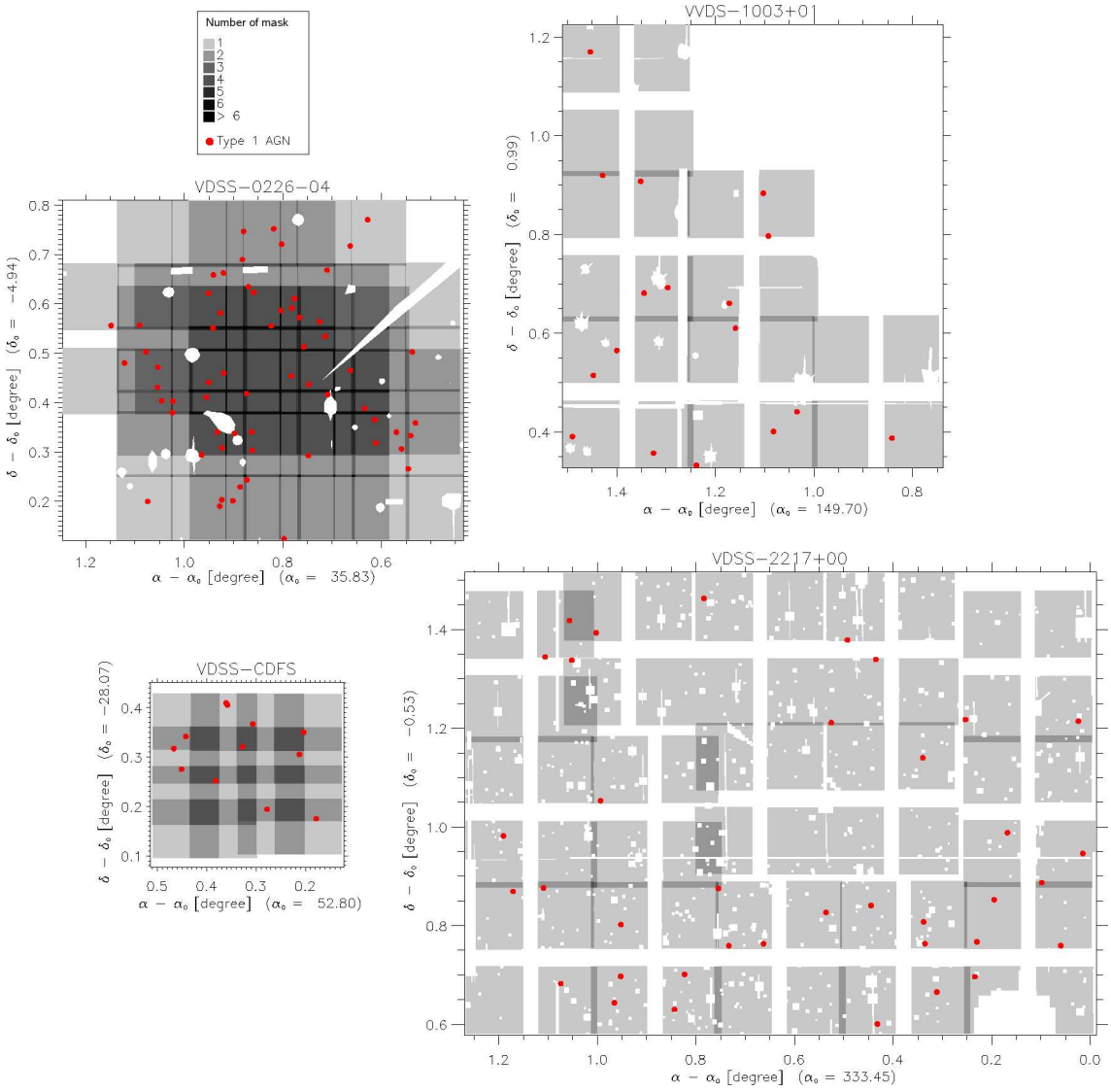

Figure 2.2: Spectroscopically observed area $\mathcal{A}$ in the VVDS first epoch fields: the grey scale indicates the number of VIMOS passes. The area masked in the photometric catalog has been subtracted to the different VIMOS field of views. Red dots indicates type 1 AGN identified in the spectroscopic catalog.

2.2.2 Target selection

To get a fully unbiased spectroscopic sample, one would pick objects at random from the input catalog. But such a procedure could then provide spectra at a less-than-optimal rate for a given observing time. For this reason a special target-selection algorithm SPOC was developed, with the aim of optimizing the use of spectroscopic follow-up time given the constraints of the VIMOS optical and mechanical layout (Bottini et al. 2005). In this optimization process, however, two biases are introduced.

First, objects with a small projected size along the slit are slightly favored for spectroscopic selection, resulting in a bias against more extended objects.

Second, the distribution of selected targets is not isotropic as the minimum distance between targets is about $11''$ perpendicular to the dispersion direction and must be at minimum $2'$ along the dispersion direction in order to avoid the superposition of spectra on the same columns. This introduces orientation dependent correlations in the spectroscopic catalog which must be taken into account if one aims to study properties related to the spatial distribution of the objects, e.g. close pair statistics, the correlation function or large-scale structure (see Pollo et al. 2005). The effect is smaller in the deep fields as they were covered with 2 to 4 passes (i.e. 2 to 4 sets of slits masks), and stronger in the wide fields covered with only a single pass.

2.2.3 Spectroscopy

The area covered by the Epoch One VVDS spectroscopy is $\sim$0.6 deg^2 in the deep fields and $\sim$1.1 deg^2 in the wide fields and the corresponding numbers of spectra are 11 338 and 7743 respectively. The target sampling rate, i.e. the ratio of selected objects for spectroscopy to the total number of objects down to the corresponding spectroscopic flux limit, is $\sim 25\%$ in both the wide and the deep surveys (see Table 2.1 and Figure 2.2 for an overview).

We used VIMOS' low-resolution red grism, which covers the wavelength range 5500 – 9500Å with a 7Å/pixel dispersion. The slit width was fixed to $1''$, providing a sampling of 5 pixels per slit and a spectral resolution of $R \sim 230$ corresponding to a spectral-resolution element of ~ 33 Å. The total integration time is 4.5 hours per mask in the deep fields and 50 minutes in the wide fields. Data reduction was performed homogeneously using the VIPGI software which was developed specifically for the VVDS survey (Scodeggio et al. 2005).

At our limiting magnitudes in both the deep and the wide fields, the median signal-to-noise ratio (S/N) per pixel is measured to be ~ 4 at a scale of 7 Å pixel.

2.2.4 Spectral classification

The process of classification and redshift determination of the reduced VVDS spectra is described in Le Fèvre et al. (2005b). As an integrated part of this process, all objects with broad emission lines are identified and flagged. When only narrow

emission lines are present, it is not straightforward to recognize AGN activity (type-2 AGN) from starburst activity, especially in spectra with relatively low S/N and limited wavelength range. For this reason we have chosen not to include narrow-line AGN in our present catalog.

2.3 Some results of the VVDS

Currently, the VVDS is the only large survey which is not using complex selection functions, and, as such it provides a view of the universe unaffected by theoretical or simulation predictions. It is probing large-scale structure, galaxy formation and evolution in a coherent way from $z \sim 5$ down to $z \sim 0.2$, going 1.5 to 2 magnitudes deeper than either DEEP2 (Davis et al. 2003) or GEMS (Rix et al. 2004). I recall here some of the measurements derived from the VVDS data which are not in the focus of this thesis.

2.3.1 Evolution of the galaxy luminosity function

Based on near-UV observations with GALEX of a sample of ~ 1000 VVDS galaxies, Arnouts et al. (2005) could measure the evolution of the rest-frame 1500Å Luminosity Function (LF). They confirm a higher star formation activity in the past, with a brightening of the parameter M_*[3] of ~ 2 magnitudes between $z = 0$ and $z = 1$.

At optical wavelengths, Ilbert et al. (2005) found as well a brightening of the M_* parameter in the U, B, V, R and I rest-frame bands. They observe that this brightening is stronger toward shorter wavelengths, corresponding to a factor of 2.6 increase in the comoving density of bright galaxies in the U-band, this factor decreasing toward redder rest-frame bands and being 1.5 in the I-band.

This evolution of the global LF is reflecting the evolution of the different galaxy types. In fact, Zucca et al. (2005) found a strong type-dependent evolution and identified the latest spectral types as responsible for most of the evolution in the UV-optical luminosity function out to z = 1.5.

2.3.2 Galaxy clustering

To measure the galaxy real space correlation length r_0 and correlation slope within the VVDS it is necessary to remove selection effects, especially the biases introduced by the instrumental slit pattern (see Sect. 2.2.2). For this reason, a scheme specific to the VVDS data has been developed and is described in Pollo et al. (2005).

Le Fèvre et al. (2005a) used this work and found the correlation length r_0 in the VVDS lowest redshift bin $z = [0.2, 0.5]$ to be smaller than for any other population at the same redshift, indicating the low clustering of very low luminosity galaxies ($r_0 = 2.2h^{-1}$ Mpc).

[3]LF are usually fitted with a Schechter function (Schechter 1976).M_* is a parameter of this function and represent a characteristic magnitude under which the density of more luminous galaxy is exponentially decreasing.

To follow the evolution of clutering of the mass in the universe from the observed galaxy correlation length would require to follow at each redshift galaxies descendent of a well-identified original population of matter halos. This is clearly not the case of the VVDS galaxies which contain a broad population mix evolving with redshift. The interpretation of the evolution of r_0 is therefore not direct. But on can remark that the slow increase of the overall galaxy population clustering up to redshift $z = 1.1$ measured in the VVDS ($r_0 \simeq 2.2 - 2.9h^{-1}$ Mpc) differs markedly from the evolution predicted by Cold Dark Matter simulations, in which the dark matter correlation length is expected to drop steeply with increasing redshift.

2.3.3 Evidence for a constant σ_8 with an evolution of the non-linear bias up to $z = 1.5$

Marinoni et al. (2005) reconstructed the galaxy density field in a cone spanning over the redshift interval [0.4,1.5] and an angular aperture of 0.4×0.4 deg within the VVDS-0226-04 deep field. This sub-field corresponds to an area with a homogeneous spatial spectroscopic sampling achieved with 4 VIMOS passes. They derived the associated Probability Distribution Function (PDF) of galaxy fluctuations. The second moment of the PDF, computed on a scale of 8 h^{-1}Mpc for galaxies brighter than $\mathcal{M} = -20 + 5log h$, is found to be well described by a constant value of $\sigma_8 = 0.94 \pm 0.07$ over the redshift interval [0.7,1.5]. The third moment of the PDF, the skewness, increase with cosmic time: the probability of having under-dense region is greater at $z \sim 0.7$ than it was at $z \sim 1.5$. By comparing the PDF derived from these observation to the theoretically predicted PDF, they find evidence for an increasing galaxy bias as a function of redshift.

2.3.4 Population of high redshift galaxies

An unexpected discovery from the First Epoch VVDS is the identification of a substantial population of bright galaxies in the redshift range $1.4 \leq z \leq 5$, based on the analysis of ∼1000 galaxies with measured spectroscopic redshifts. Le Fèvre et al. (2005b) find that there are 2 to 6 times more galaxies at $z \sim 3$ than previously thought (Steidel et al. 1999). Color-selected surveys of high redshift galaxies thus miss a large fraction of the population of bright galaxies at $z \sim 3 - 4$ compared to the VVDS purely magnitude selected survey. This could be partly due to galaxies not being a simple combination of stellar populations but rather harboring a complex mix of stars, dust, and AGN as evidenced by mid-IR and sub-mm surveys (Chapman et al. 2003). The Luminosity Function built from the VVDS shows a stronger bright end suggesting a star formation rate higher than previously thought at these redshifts. The luminosity density that results from the VVDS is comparable to that estimated in other studies. However, the relative contribution of the most luminous galaxies compared to the fainter ones is at least twice as large in the VVDS compared to former estimates (Paltani et al., in preparation).

Présentation du VIMOS-VLT Deep Survey

Le VVDS est un programme exhaustif d'observation en imagerie et en spectrocopie de l'Univers profond dont l'objectif est d'étudier l'évolution des galaxies, des AGN et des structures à grandes échelles sur de larges volumes couvrant une importante échelle de temps cosmique.

Il complémente l'effort impressionnant conduit par les deux surveys majeurs, le SDSS (Abazajian et al. 2003) et le 2dF (Colless et al. 2001), qui, dans l'univers local, établissent les propriétés de plusieurs centaines de milliers de galaxies et caractérisent leur répartition spatiale.

La stratégie adoptée pour réaliser ce programme est de construire un catalogue spectroscopique purement limité en flux dans la bande I. Ce catalogue s'appuie sur un survey large, le *wide survey* avec une magnitude limite $I_{AB} = 22.5$ et un survey profond, le *deep survey*, limité à $I_{AB} = 24$. Dans le cas des AGN de type 1, ce choix de la bande I permet la sélection d'objets avec un redshift de 0 à 5. Pour réduire les effets de variance cosmique produits par la présence de grandes structures, le *wide survey* est mené dans trois champs indépendants situés à haute latitude galactique, le VVDS-1003+01, le VVDS-1400+05 et le VVDS-2217+00. Le *deep survey* est principalement mené sur le champ VVDS-0226-04, complémenté par un champs additionel, le VVDS-CDFS.

Afin de collecter les données spectroscopiques nécessaires à ces objectifs, le consortium du VVDS a construit l'instrument VIMOS (Visible Imaging Multi-Objet Spectrograph), capable de produire plus de 600 spectres simultanément. Couplé à la puissance d'un des Very Large Telescopes (VLT) de huit mètres de l'ESO, VIMOS procure une efficacité unique de machine à remonter le temps.

L'aire sur le ciel couverte par les premières données du VVDS, utilisée dans ce travail de thèse, correspond dans le *wide* et *deep survey* respectivement à $\sim$0.6 deg^2 et $\sim$1.1^2. Sur cette surface, approximativement un quart des sources de notre catalogue photométrique ont été observée spectroscopiquement, ce qui correspond á $\sim$8 000 spectres dans le *wide* survey et $\sim$11 000 spectres dans le *deep* survey. Au cours du processus de classification spectroscopique, tous les objets possédant une raie d'émission large ont été repérés. C'est sur l'échantillon de 130 AGN ainsi collectés que s'appuie l'étude de cette thèse.

Chapter 3

The VVDS AGN sample

3.1 The VVDS AGN sample

The AGN catalog considered in this thesis consists of the sub-sample of objects in the VVDS spectroscopic catalog identified purely on the basis of the presence of one or more broad emission lines. Given our effective spectral resolution, we consider that it contains all objects with detected broad lines full width half maximum (FWHM) larger than 1000 $\mathrm{km\,s^{-1}}$. We introduce here after the acronym *BLAGN* for Broad line AGN, to refer to these objects. This makes it clear then, that only type-1 AGN with an *observed* broad line are selected. For example, peculiar type-1 AGN with narrow Balmer lines will not enter our catalog when observed at low redshift.

We make **no** distinction between Seyfert galaxies and QSOs based on the absolute magnitude or morphology of the objects.

The final sample of BLAGN selected from the VVDS survey consists of 56 objects from the wide fields (the "wide BLAGN sample") and 74 objects from the deep fields (the "deep BLAGN sample"). The total number of 130 BLAGN corresponds to about 0.7% of the objects with a measured redshift in the total VVDS database. Not all of the 130 BLAGN have a secure redshift. In some cases, we have two or more possible redshifts for a given object ('redshift degeneracy').

Redshift degeneracy

The exact list of emission lines we expect to detect in any given spectrum is a function of its S/N. In addition, because of the limited wavelength coverage of the observations, there are some redshift intervals where only a single broad emission line may be detected in our spectra (see Figure 3.1). In these cases, where no other features (e.g. narrow emission lines, absorption systems, Lyman forest) are present, several identifications of the broad line may be possible, leading thereby to a degeneracy of solutions for the redshift (see an example in Figure 3.3).

In order to treat redshift degeneracy in a consistent way, we have taken the SDSS composite spectrum of BLAGN (Vanden Berk et al. 2001), convolved it to our resolution, and added noise. For each line we then determined the S/N which

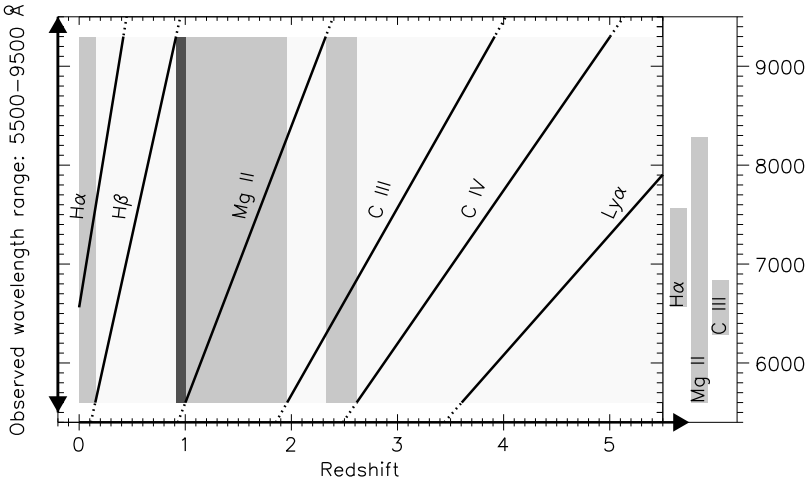

Figure 3.1: Visibility in the wavelength range of our data of AGN broad emission lines versus redshift: The thick lines trace the observed wavelength as a function of redshift of the main AGN broad emission lines that we expect to detect in our spectra. The objects in which we detect only a single broad emission line are expected to be in the redshift ranges shown in light gray. We expect to miss BLAGN lying in the narrow redshift range filled in dark gray since no strong broad emission line is visible at these redshifts within our observed wavelength window. On the right side we note the wavelength ranges in which each broad emission line can be observed as isolated. Hβ and Lyα are not reported here as such since they are not affected by the redshift degeneracy (we expect to observe them, respectively, with the [O III] doublet and the Lyman forest).

would provide a 3.5 σ detection of the line. Following this procedure we have found that down to a S/N of 4 per resolution element, we are able to detect and recognize as broad the following lines: H$\alpha\lambda$6563, H$\beta\lambda$4861, Mg IIλ2798, C III]λ1909, C IVλ1549 and Ly$\alpha\lambda$1216.

The visibility windows of these lines within the VVDS observed spectral range are shown in Figure 3.1 as a function of redshift. The redshift ranges where we expect to observe a single broad emission line (in gray) are: [0 - 0.13], [1.0 - 1.9] and [2.4 - 2.6].

Since we always expect to detect the narrow-emission-line doublet [O III]$\lambda\lambda$4959,5007 close to Hβ, we consider the detection of Hβ to securely identify the redshift. The same applies to Lyα which can be identified from the Lyman forest.

Consequently, for an object with a single broad line, we have one to three potential redshifts. In addition, a small gap is present at redshift $\sim$0.95 (dark gray in Figure 3.1) where no broad emission line is visible within our observed wavelength window.

A small fraction of spectra ($\sim$ 15%) fall outside this general scheme, due to a lower S/N or to technical limitations such as strong fringing. For this reason some objects have up to four possible redshifts.

Because of these limitations, a total of 42 BLAGN in our original sample were flagged as having a degenerate redshift (Flag 19, as defined here after). To solve this redshift degeneracy we have first looked for the objects already observed in other spectroscopic surveys in the same areas. From the CDFS optical spectroscopic

data we found the redshifts for 3 of the objects (Szokoly et al. 2004). Furthermore, additional observations have been carried out with FORS1 on the VLT in March 2004 and November 2005 to extend the spectral coverage down to 3800 Å . From these observations we have been able to solve the redshift degeneracy and find a secure redshift for another 25 objects.

The fraction of BLAGN remaining with a degenerate redshift correspond to ~ 10 % of the total BLAGN sample.

Identification and redshift quality flags

Based on the above analysis, each entry of our BLAGN catalog has been assigned a quality flag according to the following criteria (these flags have been adapted from the VVDS galaxy flag definition):

Flag 14: BLAGN with secure redshift measurement (i.e. two lines or more);

Flag 13: BLAGN with only one line detection but with the redshift secured from other informations such as:

- no other possible identification for the given wavelength range;
- an "intervening absorption line" system is detected and leaves only one redshift solution for the BLAGN;
- strong iron features, so called 'bumps', are detected;
- a second line is marginally detected;

Flag 19: BLAGN with only one detected line and more than one possible redshifts;

Flag 12: Object with secure redshift but for which the broad line nature is uncertain due to the low spectral resolution, often coupled with low S/N or technical limitations (i.e. it could be a narrow line object);

Flag 11: Both the redshift and the broad line nature of the target are uncertain.

The statistics of the data quality according to these flags is summarized in Figure 3.2. Objects with uncertain broad emission lines (flags 11 and 12), corresponding to $\sim$(10-15)% of our survey objects, are excluded from further analysis, since we want to avoid contamination by normal galaxies and we do not know which fraction of these objects are really broad-line AGN. The final sample of BLAGN with secure classification (flag 14, 13 and 19) contains 130 objects. They are presented in Appendix A: Table A.1 gives the list of BLAGN in our wide and deep samples for which we have a secure redshift, while Table A.2 lists the BLAGN for which we still have a redshift degeneracy (flag 19).

Figure 3.3 presents some examples of spectra across our magnitude and redshift range. In particular object 220567224 (upper left panel) is the highest redshift BLAGN of our sample. This extremely bright object –previously found by the SDSS high-redshift quasar survey– was re-discovered in our wide survey. Object

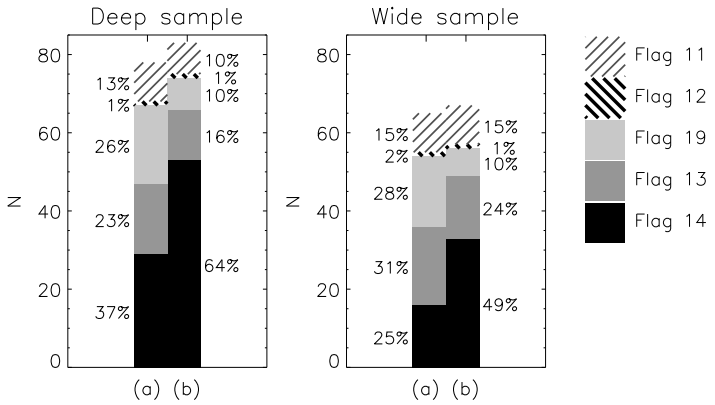

Figure 3.2: AGN quality flags statistics. Columns (a) corresponds to our original quality flags, before looking for objects already existing in other spectroscopic samples and performing re-observations with FORS. Columns (b) correspond to our current quality flag statistics.

020180665 (upper right panel) is an example of extreme broad-absorption-line (BAL) spectrum. Out of 41 objects for which we observe the C IV line either in the VVDS original spectra, either in our FORS additional spectra, 9 are found QSO to have broad absorption lines, and two other example of such extreme BAL QSO are found (objects 220556037 and 100343840). Object 020302785 (right panel) is a BLAGN at z=2.24 in which there are evident absorption features that can be well fitted by metal absorptions of a system at z$\sim$ 1.727. Object 020463196 is an example of AGN in which strong [Ne III], [Ne IV] and [Ne V] lines are visible. This suggests a hard ionizing continuum. Object 220098629 is an illustration of flag 19 AGN for which the redshift was resolved with additional observations obtained with F0RS1.

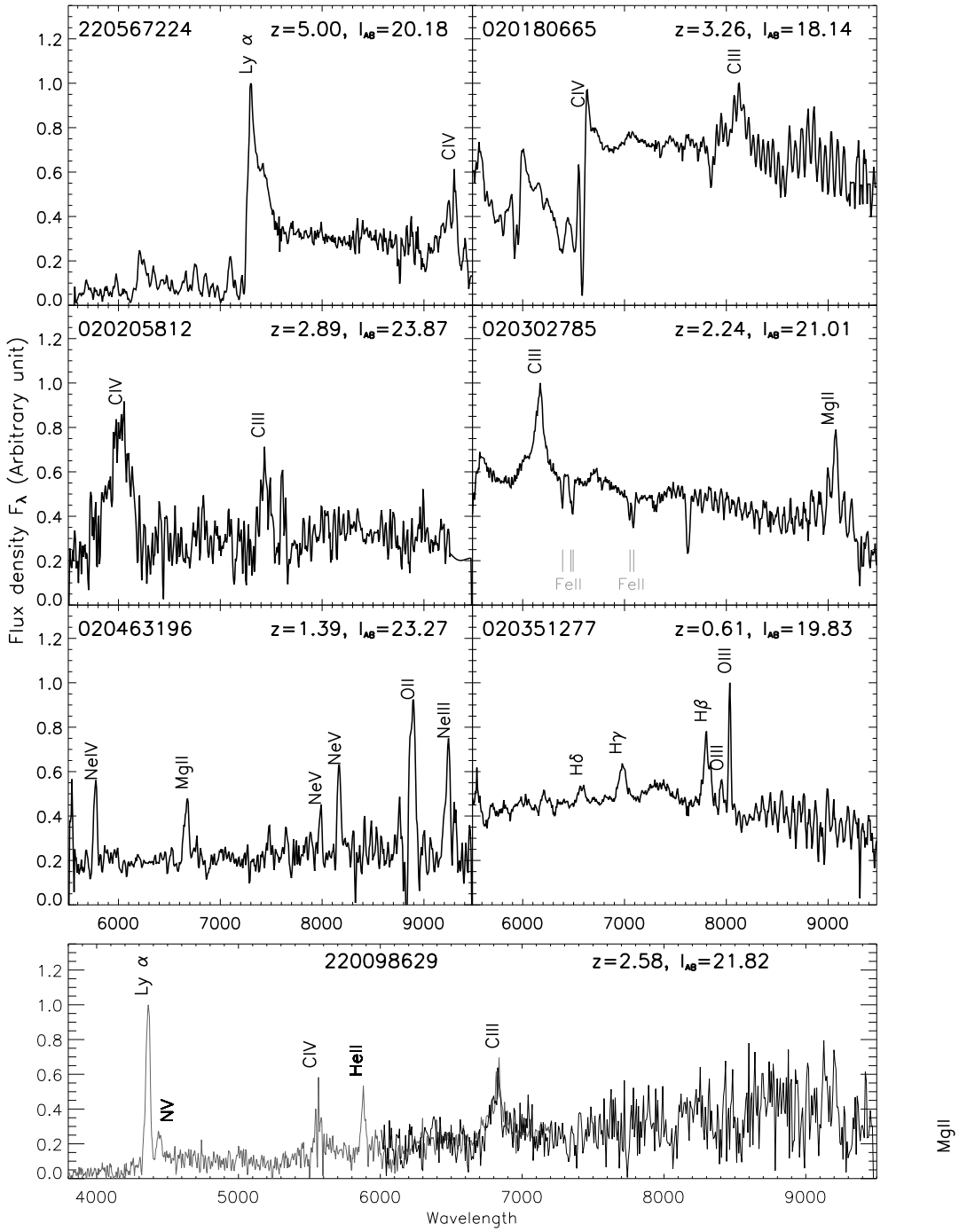

Figure 3.3: Examples of BLAGN spectra across our magnitude and redshift ranges. Spectra of AGN with $I_{AB} > 23$ have been rebinned to 5 pixels. The integral catalog of spectra is presented in Appendix B.

3.2 Selection function

To study the statistical properties of any sample it is fundamental to understand qualitatively, and estimate quantitatively its selection function. The selection function is the function providing the probability for an object meeting with our initial criteria to be effectively selected in our BLAGN catalog. If it is possible to estimate this probability, we can, a posteriori, correct our statistical analysis for objects which will not be selected in our sample. In our sample we need to correct for (1) the BLAGN which have not been spectroscopically observed althought they were part of our flux limited photometric catalog; (2) the spectrocopically observed BLAGN which were not correctly identified from their spectrum. This correction is performed by applying to our BLAGN two statistical weights, w^{TSR} and w^{SSR} defined following Ilbert et al. (2005) as follows:

3.2.1 Treatment of non-targeted BLAGN: w^{TSR}

The *Target Sampling Rate* (hereafter TSR) is the fraction of objects in the photometric catalog inside our targeted area which have been spectroscopically observed. As already mentioned in Section 2.2.2, the TSR is a function of the projected size, $x - radius$, of the objects along the slits. Objects with a small x-radius are slightly favored by the selection process. Figure 3.4 illustrates the effects of this parameter: the distribution of x-radii in the spectroscopic catalog is slightly biased towards smaller values of the x-radius than in the photometric catalog. To balance for non-targeted BLAGN we apply to our BLAGN the weight $w^{TSR} = \frac{1}{TSR}$.

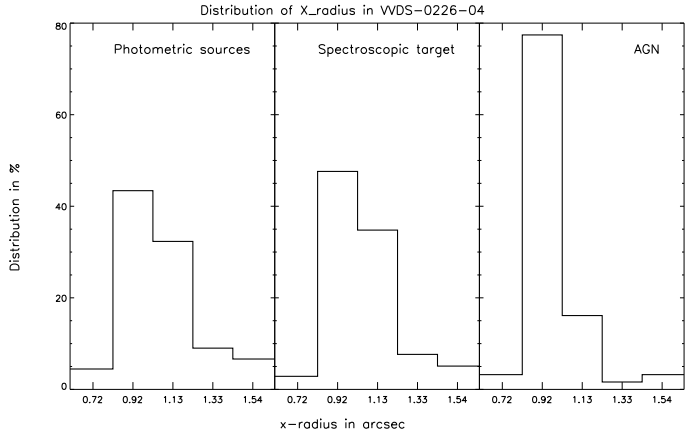

Figure 3.4: Distribution of x-radius in three catalogs: the photometric catalog, the spectroscopic catalog and the BLAGN catalog. The x-radius corresponds to the size of the object projected along the slit and converted into discrete values, with steps corresponding to the pixel size.

3.2.2 Treatment of misclassified AGN: w^{SSR}

The *Spectroscopic Success Rate* (SSR) is the probability of a spectroscopically targeted object to be securely identified. It is a complex function of the BLAGN red-

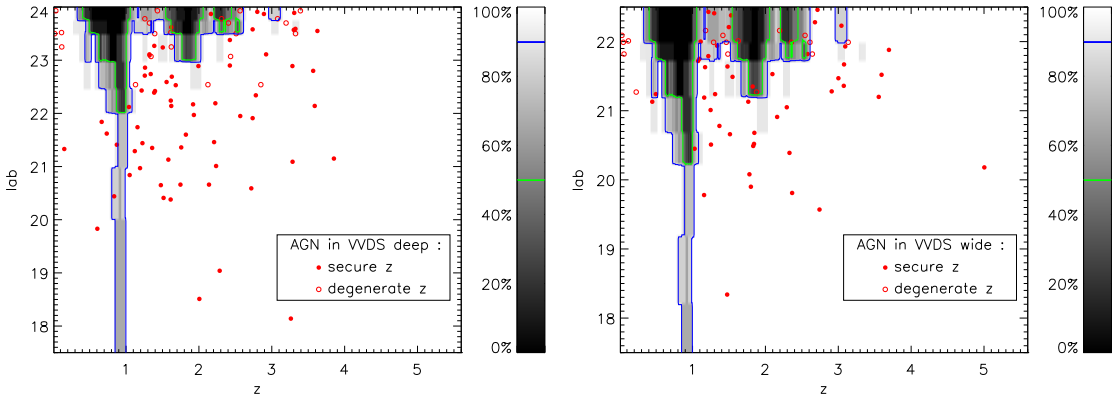

Figure 3.5: *Spectroscopic Success Rate* for BLAGN in the VVDS deep (left) and wide (right) sample as a function of redshift and apparent magnitude. Contour lines are drawn for 90% and 50% of the identification success rate. The location of BLAGN with a secure redshift is reported with filled dots. BLAGN with a degenerate redshift are plotted at their different redshift solutions with open circles.

shift, apparent magnitude and intrinsic spectral energy distribution. We evaluated the SSR with two different methods:

Simulations

Twenty deep VIMOS pointings or a total of 2745 spectra have been simulated in order to evaluate the SSR. Theses simulations incorporated the major instrumental effects of VIMOS observations, including sensitivity curve, fringing in the red-most part of the spectra, sky background and contamination by zeroth-orders. Each spectrum has been simulated using the SDSS composite spectrum as a template. Redshifts and magnitude were drawn at random in the ranges $0 < z \leq 5$ and $17.5 \leq I \leq 24$ respectively. The spectra were then analyzed and classified in the same way as the real spectra, except that we did not try to resolve cases where a single line was present; we merely checked whether the BLAGN nature of the object could be detected in the spectrum or not. For the wide field, we used the same SSR derived for the deep field, but shifted by 1.8 magnitudes to take into account the difference in exposure times between the deep and wide parts of the survey.

Because it includes all instrumental effects and reproduces the conditions of the VVDS real spectral classification, we expect this method to give a robust estimate of our SSR. The main limitation of this method is its large time-consuming nature, making it impossible for example, to repeat this process for a different QSO template. For this reason we estimated the SSR with a complementary, entirely automatic approach.

Figure 3.5 presents the resulting SSR as a function of redshift and apparent I_{AB} magnitude in the deep and wide fields.

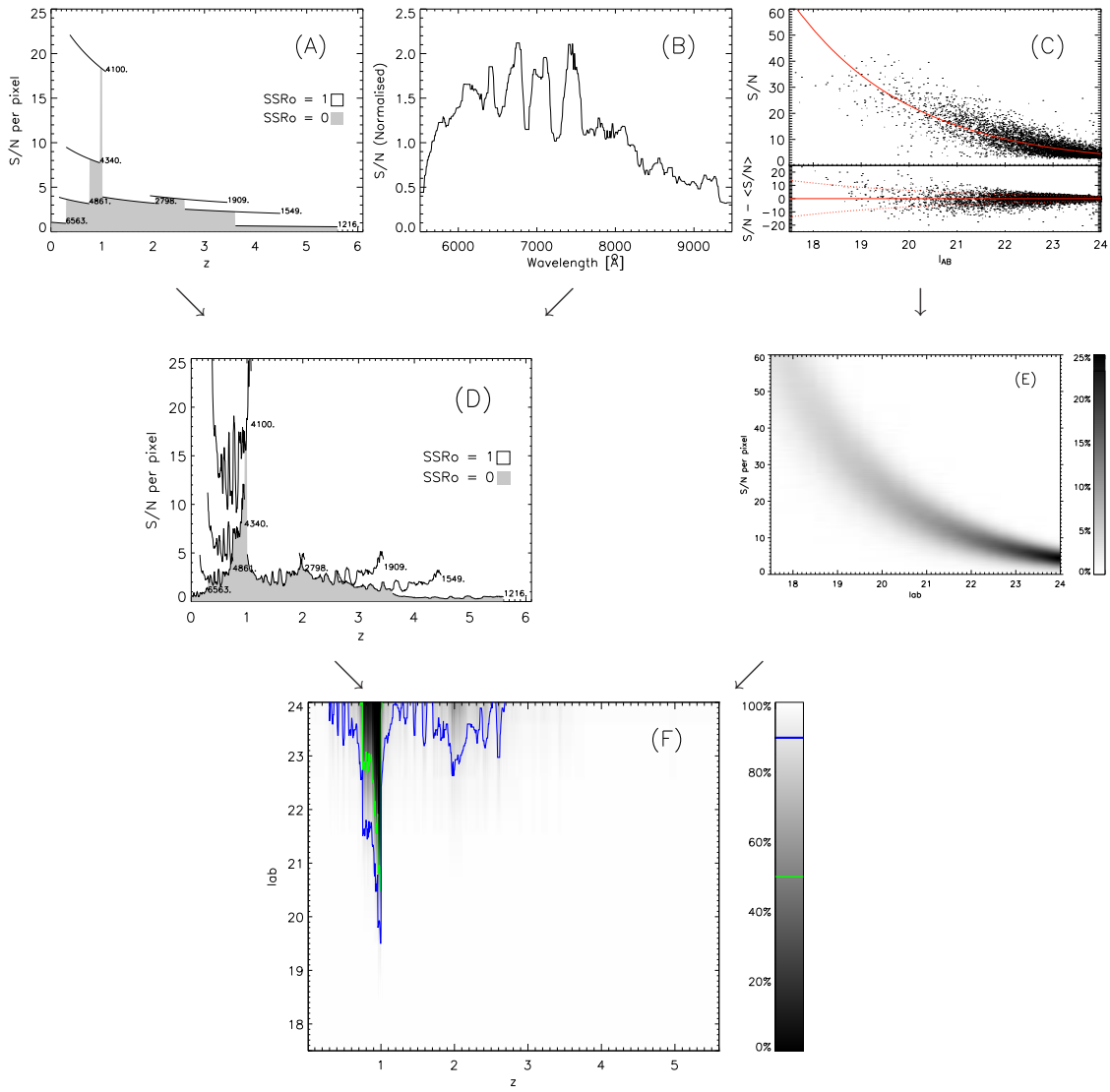

Figure 3.6: Automatic estimation of the *spectroscopic success rate*. The assumed EWs and FWHM of the broad emission lines in this example are the ones measured in the SDSS composite spectrum Vanden Berk et al. (2001).
(A): Theoretical S/N threshold for detecting a broad emission line as a function of redshift in the VVDS (see Appendix C). The shaded area correspond to the area where we are not able to classify a broad line AGN. Individual broad emission line detection thresholds are plotted over the redshift range where they cross our spectral coverage.
(B): Median normalized S/N spectrum of 6000 galaxies in the VVDS deep sample. The humpy pattern is produced by the succession of series of sky emission lines. For wavelengths larger than 7800 Å, the noise is dominated by the non-linear fringing.
(C): Exponential fitting of the first and second moments of the S/N distribution in the VVDS measured as a function of magnitude I_{AB}.
(D): Spectrum mean S/N threshold for detecting a broad emission line as a function of redshift in the VVDS.
(E): Assumed S/N distribution in the VVDS sample.
(F): Predicted SSR in the VVDS deep sample.

Alternative approach

In order to estimate our ability to select AGN with different emission line properties, we developed an automatic method to evaluate our SSR. A schematic overview of the procedure is given Figure 3.6. We detail hereafter the different steps of the procedure. All signal-to-noise ratios are expressed in unit of 7 Å pixels.

(A) S/N threshold for detecting a broad emission line as a function of redshift: We assume that a broad emission line is detected when the core enclosed by its FWHM is above the 3.5σ noise level. As detailed in Appendix C, if we assume a Gaussian profile, this correspond to the following relation:

$$S/N_{limit} \sim 7.5 \frac{\sqrt{\frac{FWHM}{d}}}{EW} \tag{3.1}$$

where d corresponds to the number of pixels per Ångström. EW and FWHM are respectively the observed equivalent width and full width half maximum. They evolve with redshift as follows:

$$EW = EW_o(1+z) \tag{3.2}$$
$$FWHM = FWHM_o(1+z) \tag{3.3}$$

From these relations, we compute the theoretical S/N threshold for detecting an AGN broad emission line as a function of redshift. Figure 3.6.A presents our calculation for the SDSS composite spectrum emission lines (Vanden Berk et al. 2001, Table 2).

(B) Median S/N spectrum in the VVDS: For the purpose of spectrophotometric studies, 6000 galaxies of the VVDS deep sample were fitted with an adapted version of the platefit software. This software was originally developed for the SDSS survey (Tremonti et al. 2004) and was then adapted to the VVDS survey as described in Lamareille et al. (2006). It provides a fit of the galaxy stellar continuum and emission lines. We assume that the residual spectra of these 6000 fitted galaxies corresponds to our noise spectrum. We normalize the obtained S/N spectra and combine them using a median. The resulting S/N spectrum is presented Figure 3.6.B.

(C) S/N as a function of magnitude in the VVDS: We consider the median value of the 6000 S/N spectra obtained previously. As shown Figure 3.6.C, our best exponential fit of the first and second moment of our S/N distribution are found to be $< S/N >= 83655 exp(-0.41 I_{AB})$ and $\sigma_{S/N} = 3754 exp(-0.32 I_{AB})$. We measure a mean S/N of ~ 4 at our limiting magnitude $I_{AB} = 24$.

(D) Figure 3.6.D corresponds to the mean S/N required in a spectrum in order to detect a broad emission line. It is the equivalent of Figure 3.6.A taking into account the variation of S/N as a function of observed wavelength.

(E) S/N distribution in the VVDS sample, as derived from the exponential fits described in (A).

(F) Map of our expected SSR, obtained by convolving our theoretical S/N threshold (D) with our S/N distribution (E).

Discussion

The SSR obtained with this automatic algorithm for the SDSS composite spectrum and our *deep* survey (Figure 3.6, panel F) is compared to the one derived from our simulations (Figure 3.5, left panel). The 90% completeness level outlined by both method is in very good agreement, however simulations predict a much sharper transition between areas with SSR$\sim$ 1, and areas where no objects are selected. In term of counts (Section 3.3), the automatic algorithm predict 30 AGN per square degree less than the simulations.

If the automated approach predict a smoother selection function it is due to the dispersion of S/N observed for a given magnitude in our sample (Figure 3.6, panel C). This dispersion of S/N of galaxy with the same magnitude can be attributed to various parameters: observing conditions, apparent size of the galaxy or discrepancy between the fitted spectra and real spectra. Since QSO are more compact than galaxies we investigated the correlation between the S/N and the half light radius of the galaxies but found no significant effect of this parameter. No systematic galaxy fit residual is found. We conclude that our distribution, Figure 3.6, panel C, is dominated by variation of the observing conditions (e.g. seeing, accuracy of the slit centering, sky brightness).

On one side, the SSR derived from simulations do not account for the dispersion of the S/N-magnitude relation. On the other side, the SSR derived from our automatic approach do not properly account for the contamination by 0ths order spectra and for the non-linear fringing noise. Simulations show that a number of AGN are probably missed because of these two instrumental effects. For this reasons, we finally decided to adopt as reference for our statistical analysis the SSR values derived from simulations.

The automated approach is used, in turn, as a tool to investigate the influence of AGN emission lines properties on our selection function.

In particular, we observe that AGN selected in our sample have in general larger equivalent width than the SDSS composite spectrum. This is observed in our composite spectrum (Section 3.6 and Table 3.2) and in our analysis of individual objects emission lines properties (Section 3.7). We argue (see discussion, Section 3.7) that this property is not only induced by the bias toward larger emission lines expected for our sample.

We therefore compare the differences of our SSR for the VVDS composite spectra and the SDSS composite spectra. This is illustrated Figure 3.7.

We observe that the difference between the two estimated of our SSR becomes significant only in areas where it is already difficult for our sample to select objects. For this reason we conserve the SSR derived from simulations using the SDSS

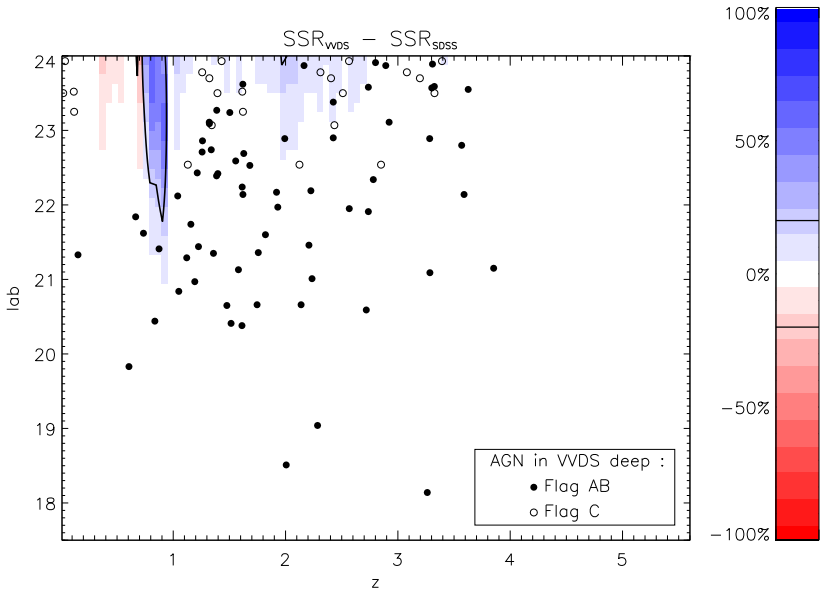

Figure 3.7: Comparison of the Spectroscopic Success Rate of BLAGN with different emission lines properties: the color scale indicates the difference of probability for selecting a VVDS-composite-like BLAGN and a SDSS-composite-like BLAGN. Black lines contour area with a difference exceeding 20%. Area in blue correspond to magnitude-redshift domains where the selection of a VVDS-composite-like BLAGN is favored in comparison to a SDSS-composite-like BLAGN. The opposite is figured in red.

composite-spectrum as a template.

To correct for missed BLAGN we apply to our objects the weight $w^{SSR} = \frac{1}{SSR}$. Objects for which the broad-line is stronger than that in the SDSS composite spectrum will be over-estimated by our method and, on the contrary, objects with weaker broad emission lines will be under-estimated.

3.2.3 Total correction

Correction for our global selection function is obtained by applying to each of our objects the product of the two weights, i.e. $w^{TSR} \times w^{SSR}$.

This method becomes however not accurate to account for BLAGN with very low probability to be selected (for example faint BLAGN with $z \sim 1$).

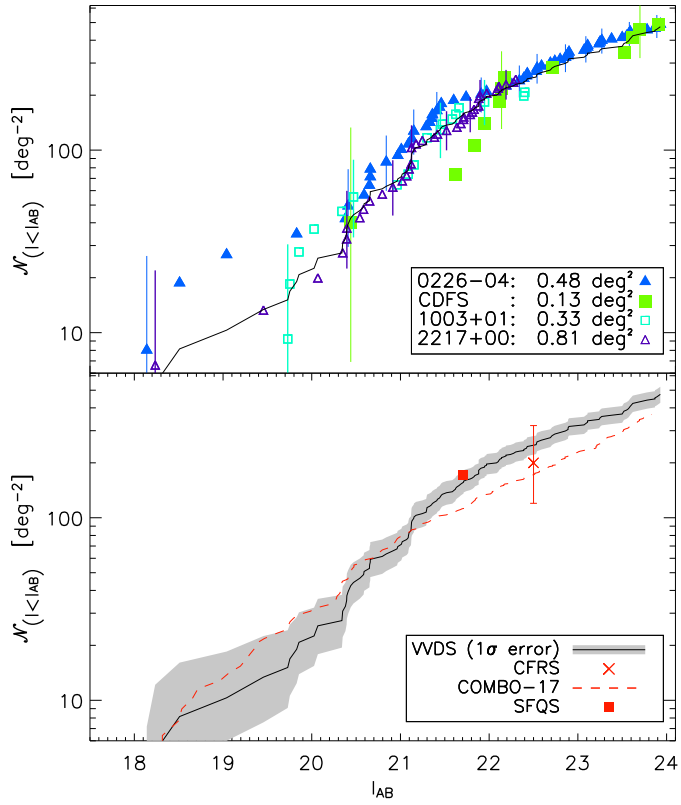

Figure 3.8: BLAGN cumulative surface density in the VVDS sample. Error bars represent the one sigma Poissonian errors. Top panel: Observed surface density in the individual fields and in the total sample (solid line). For clarity error bars are reported for every 5 data points. Bottom panel: Comparison with the CFRS and COMBO-17 surveys.

3.3 Counts

Since the objects to be observed spectroscopically in the VVDS are selected on the basis of their I_{AB} band magnitude, we have computed the BLAGN cumulative surface density in this band with the following algorithm:

$$\mathcal{N}\left(\leq I_{AB}\right) = \frac{1}{\mathcal{A}} \sum_{i, I_{AB,i} \leq I_{AB}} w_i^{TSR} w_i^{SSR}$$

where $\mathcal{A}$ is the geometrical area targeted by the spectroscopic survey, i.e. the area covered by the different VIMOS fields of view corrected for the area masked in our photometric catalogs (see Figure 2.2); the sum is running over all BLAGN i with magnitude $I_{AB,i}$ less or equal to I_{AB}.

The upper panel of Figure 3.8 presents the cumulative surface density derived in the VVDS individual fields with the corresponding Poissonian error bars (Gehrels 1986). Although some differences are visible in the counts of different fields , the surface densities measured in all our fields at $I_{AB} = 22.5$, corresponding to the magnitude limit of the wide fields, are all consistent, within the errors, with each other. We conclude that the error induced by cosmic variance is smaller than our

Table 3.1: BLAGN number counts as function of I_{AB} magnitude. N is the actual number of BLAGN in the VVDS survey while $\mathcal{N}(\leq I_{AB})$ is the cumulative surface density of BLAGN (objects / square degree) corrected from incompleteness.

I_{AB}	N	$\mathcal{N}(\leq I_{AB})$
19	3	10
20	9	22
21	29	71
22	76	196
23	108	327
24	130	472

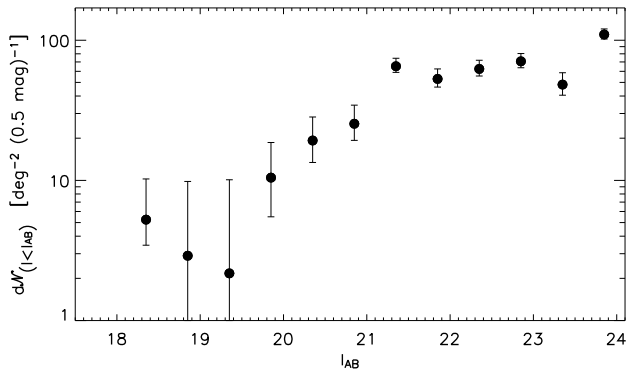

Figure 3.9: BLAGN differential surface density in the VVDS sample. Error bars represent the one sigma Poissonian errors.

Poissonian noise. We compute a single $log\mathcal{N} - I_{AB}$ curve by merging the data from the four fields into a single coherent sample (Avni & Bahcall 1980) using the following algorithm:

$$\text{if } I_{AB} \leq 22.5: \quad \mathcal{N}(\leq I_{AB}) = \frac{1}{\mathcal{A}_{wide} + \mathcal{A}_{deep}} \sum_{i, I_{AB,i} \leq I_{AB}} w_i^{TSR} w_i^{SSR} \; ;$$

$$\text{if } I_{AB} > 22.5: \quad \mathcal{N}(\leq I_{AB}) = \mathcal{N}(\leq 22.5) + \frac{1}{\mathcal{A}_{deep}} \sum_{i, 22.5 < I_{AB,i} \leq I_{AB}} w_i^{TSR} w_i^{SSR}.$$

At the limit of our deep fields ($I_{AB} < 24.0$) our measured surface density of BLAGN is $\sim 472 \pm 48$ per square degree and the correction applied for misclassified BLAGN corresponds to $\sim 10\%$ of this value. The differential surface density computed for the total sample is shown in Figure 3.9. In this plot the different points and associated errors are independent from each other. This figure suggests

a significant turn-over in the slope of the counts at $I_{AB} \sim 21.5$. At $I_{AB} \gtrsim 21.5$ the differential number counts are still increasing with magnitude, but at a much lower rate than at brighter magnitudes. This effect is seen, although less clearly, in the continuous flattening with magnitude of the integral number counts in Figure 3.8.

Comparison with other spectroscopic surveys is not straightforward since most of the optical QSO surveys are based on much shallower B band flux limited samples and most of them are not complete over the entire redshift range due to their different selection criteria. The CFRS is an exception with essentially the same selection function as the VVDS (i.e. a flux limited sample in the I band with no color or morphological selection). Although it contains only 6 BLAGN at a magnitude limit of $I_{AB} < 22.5$ (see Schade et al. 1996), the surface density resulting from these objects is in excellent agreement with our current measurement (see Figure 3.8, lower panel).

The surface density derived from the recent SDSS Faint Quasar Survey (SFQS Jiang et al. 2006) is also reported in the lower panel of Figure 3.8. This survey selects AGN over the redshift range 0-5 and up to $g = 22.5$. The surface density, corrected for completeness, is computed in the g band (Jiang, private communication) and approximately translated to the I_{AB} band assuming the mean color term observed in our sample: $< I_{AB} - g >= -0.7$. The VVDS and SFQS number counts at $I_{AB} \sim 21.8$ are in good agreement.

With a limiting magnitude similar to ours, the only other comparable sample is the COMBO-17 sample (see Wolf et al. 2003), which is however based on photometric selection of AGN, with a small fraction of spectroscopic confirmation. For comparison with our sample, we have obtained the cumulative counts of the complete COMBO-17 sample, without redshift restriction (Wisotzki, private communication). Since this sample is selected in R-band, we apply a global color term of -0.16 magnitude to translate its surface density to our I_{AB} reference system. This color term corresponds to the mean $I_{AB} - R_{vega}$ color observed for our objects. In addition, a dozen of BLAGN are observed in both the VVDS and COMBO-17 samples. The mean color term of these objects is measured to be -0.12. The result is presented in the lower panel of Figure 3.8. Our number counts are statistically consistent with those of COMBO-17 for magnitudes brighter than 21.5. At fainter magnitudes our counts are systematically higher by $\sim 30 - 40\%$. This can be explained by incompleteness in the COMBO-17 at low redshift in the regime where the host galaxy contamination becomes non-negligible. This is the reason why the published version of the COMBO-17 AGN sample was restricted to $z > 1.2$.

Figure 3.10, compares the cumulated surface density for our sample restricted to $z > 1.2$ with the COMBO-17 sample in R band. Our total number counts –with $\mathcal{N}(R \leq 24) = 340 \pm 47$– compares well to this sample for which $\mathcal{N}(R \leq 24) = 337$. However if we consider these number counts in different redshift ranges, we do not observe a flattening of the number counts for $z < 2.2$ towards faint magnitudes. This effect might result from incompleteness of the COMBO-17 sample above $z > 1.2$ at the faintest magnitude (we detect in our sample contribution of host galaxy up to $z \sim 1.6$: see Figure 3.14). This difference is observed in the lower redshift bin of our

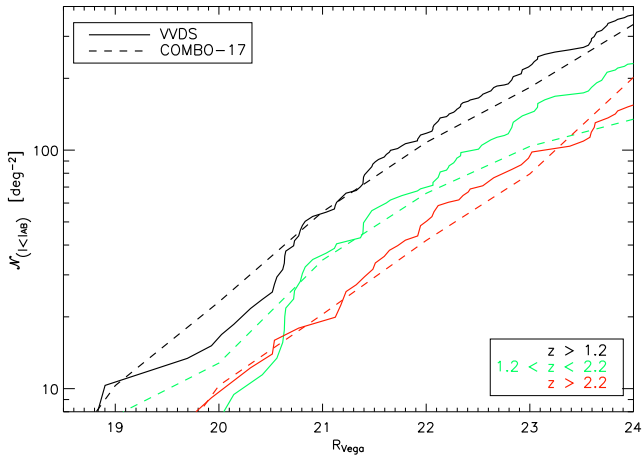

Figure 3.10: Comparison of the BLAGN cumulative density of the VVDS and the COMBO-17 sample in different redshift bins.

luminosity function (Section 3.8).

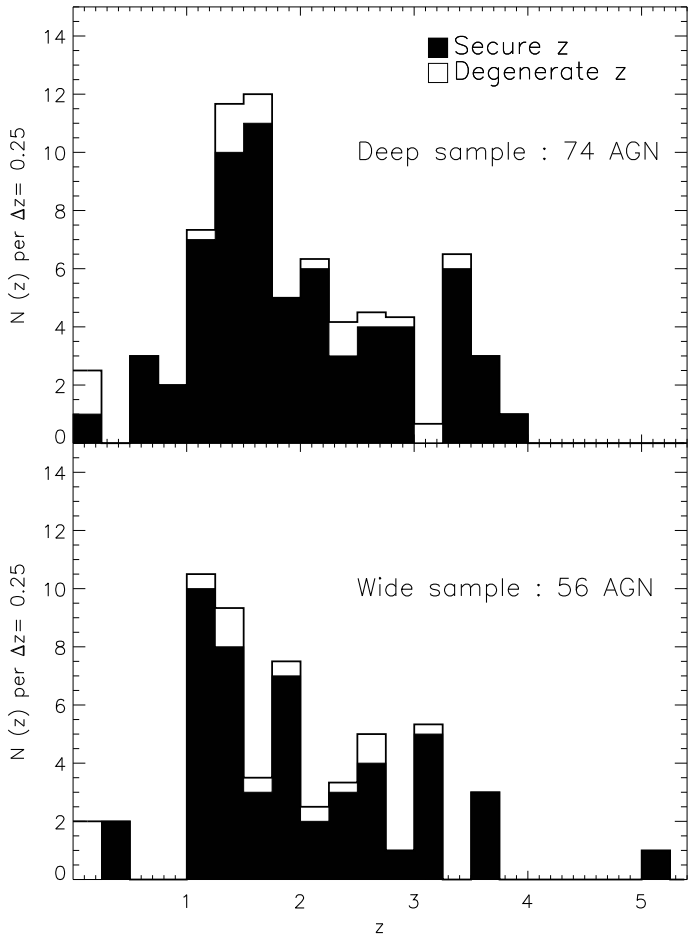

Figure 3.11: Redshift distribution of the VVDS BLAGN sample. The shaded histogram corresponds to BLAGN with a secure redshift (flags 13 and 14), while the unshaded histogram includes also flag 19 BLAGN, distributed with an equal weight over the different redshift alternatives.

3.4 Redshift distribution

The redshift distributions of our wide and deep samples are presented in Figure 3.11. BLAGN a with degenerate redshift solution (flag 19) have been distributed with equal weights in the different possible redshifts. The absence of objects between redshift 0.5 and 1 in the wide fields can be attributed to our low efficiency for selecting objects at this redshift (see Figure 3.5). The main uncertainty resulting from BLAGN with a degenerate redshift concerns the fraction of BLAGN at low redshift.

The fraction of $z > 3$ objects is $\sim 17\%$ in the wide sample and $\sim 15\%$ in the deep sample. The mean redshift is ~ 1.8 in both the wide and deep samples. Considering all flag 19 BLAGN successively at their lowest and highest redshift solution, we find that the mean redshift of both deep and wide sample lies between 1.5 and 2.1. This shows that, by pushing our magnitude limit from that of the wide to that of the deep survey, we are not increasing our mean redshift but rather exploring the fainter

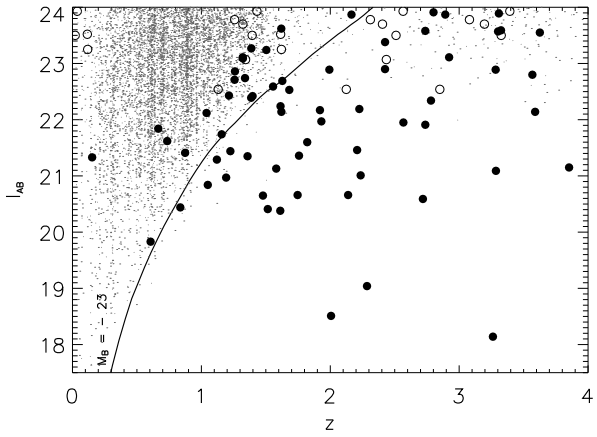

Figure 3.12: Apparent I_{AB} magnitude as a function of redshift in the VVDS deep sample. Galaxies are plotted with points, BLAGN with secure redshift are plotted with filled dots and BLAGN with degenerate redshift are presented at all their redshift solutions with empty circles. The thick line gives the apparent magnitude of a BLAGN template of absolute magnitude $M_B = -23$ and therefore corresponds to the transition between QSOs and Seyfert galaxies.

part of the luminosity function at all redshifts.

Figure 3.12 shows the apparent magnitude versus redshift distribution of BLAGN and galaxies in the deep sample. We see that some of our BLAGN are sampling the faint magnitudes, well inside the galaxy luminosity function. We find that $\sim 35\%$ of the objects in the deep sample are Seyfert galaxies, rather than QSOs, having absolute magnitudes fainter than $M_B = -23$.

3.5 Morphology and color properties

The fundamental property of our survey is that it does not suffer neither from morphological nor from color selection biases which are present in most optical surveys. Therefore, using the VVDS deep photometric data, we are able, a posteriori, to estimate quantitatively the fraction of AGN missed by these standard selection criteria.

3.5.1 Morphological analysis

The use of a morphological selection of point-like objects causes the loss of BLAGN candidates for two main reasons. The first is due to the fact that a reliable separation between point-like and extended sources from ground-based images is possible only for relatively bright objects. The second reason is associated with an intrinsic property of BLAGN: at relatively low z and low intrinsic luminosity, BLAGN may appear extended or at least slightly resolved because of significant contribution from the host galaxy. This effect can introduce a redshift-dependent bias in morphologically selected AGN samples, especially at faint magnitudes.

We have conducted a morphological analysis of our BLAGN sample through the study of various shape parameters, which define a characteristic radius weighted by the light distribution function (Kron 1980). In particular, for this analysis we used the `SExtractor` flux-radius parameter, denoted as r_2, which measures approximately the radius which encloses half of the object's total light. This parameter is used to identify point-like sources, because, for unresolved objects, it is directly related to the width of the point spread function and it is independent of luminosity (for non-saturated objects). In the plane $r_2 - I$ magnitude, we can distinguish two different classes of objects: unresolved sources that occupy a well defined strip of the plane at small and approximately constant values of r_2 and resolved objects for which r_2 varies with magnitude.

This analysis is restricted to the VVDS-0226-04, VVDS-1003+01 and VVDS-2217+00. We exclude the CDFS for which this parameter is not measured. Since our data, covering large areas in different sky regions, have been taken with different seeing conditions, the stellar locus resulting from the use of the measured r_2 values is significantly broadened, thus making a clear separation between point-like and extended objects difficult. To account for this, we used an "adaptive" classification technique following McCracken et al. (2003): after dividing the field into many sub-areas, mainly following the pattern corresponding to the different pointings, we have normalized the flux radius of each object to the local r_2 mode, computed for all the objects within each sub-area. Figure 3.13 shows this normalized r_2(I) parameter versus I-magnitude.

The use of the normalized r_2(I) allows us to improve our ability to distinguish point-like from extended objects. As shown in Figure 3.13, this separation appears to be feasible up to $I_{AB} \sim 22.5$ (without normalization, the corresponding limiting magnitude was $I_{AB} \sim 21.5$). Beyond this magnitude ($I_{AB} \sim 22.5$), the number of

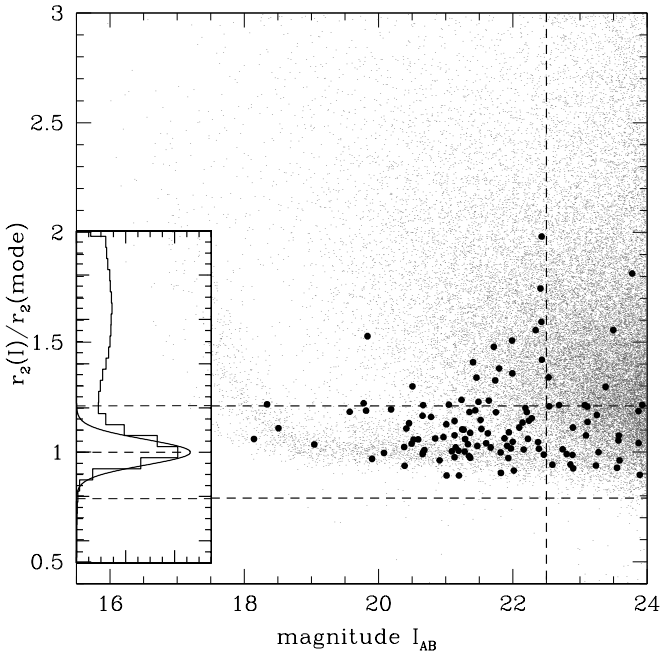

Figure 3.13: Normalized $r_2(I)$ parameter versus I_{AB} magnitude. The two horizontal lines correspond to the range in $r_2(I)$ that we have adopted for our morphological classification of point-like sources. Large circles are the spectroscopically confirmed BLAGN. The inset shows the r_2 distribution of objects with $21.0 < I_{AB} < 22.0$, fitted with a Gaussian of $\sigma = 0.06$.

galaxies with small $r_2(I)$ parameter increases and no reliable selection of point-like sources is possible.

The two horizontal lines correspond to the range in $r_2(I)$ that we have adopted for our morphological classification of point-like sources. The upper limit in this range corresponds to about 3.5σ of the Gaussian fit of the r_2 normalized distribution of point-like sources. As shown by the inset on the left of Figure 3.13, this somewhat conservative choice makes sure that the vast majority of point-like sources are really classified as point-like, allowing some contamination from extended objects, especially at faint magnitudes. Efficiency in classifying point-like sources has been tested on the spectroscopically confirmed stars in the magnitude range $18.5 \leq I_{AB} \leq 22.5$ (the bright limit has been set in order to exclude saturated objects – see Figure 3.13). We find that 95% of the stars with secure spectroscopic identification (flag $\geq$ 3, see Le Fèvre et al. 2005b) are correctly classified as point-like sources.

Figure 3.13 also shows the location in this plane of the spectroscopically confirmed BLAGN. In this analysis we consider only BLAGN brighter than $I_{AB} = 22.5$ (90 objects); within this limit, 77% of the BLAGN are classified as point-like, while 21 of them (23%) are classified as extended. This percentage is significantly higher than that of morphologically misclassified stars (see above).

Nineteen of these 21 extended BLAGN, have a secure redshift measurement, while the other 2 are BLAGN with two or more possible values for z. Figure 3.14

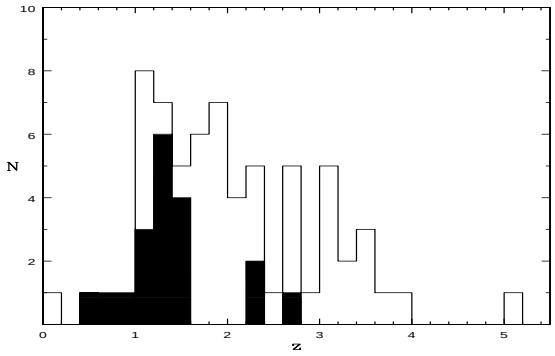

Figure 3.14: Redshift distribution of BLAGN with secure redshift and $I_{AB} < 22.5$. The unshaded histogram show the objects classified as point-like while the filled histogram shows the objects classified as extended.

shows the redshift distribution of BLAGN with secure redshift and $I_{AB} \leq 22.5$, morphologically classified as extended compared to those classified as point-like. The two redshift distributions are significantly different (the probability that they are drawn from the same distribution, as estimated from a Kolmogorov-Smirnov (KS) test, is smaller than $\sim 4 \times 10^{-4}$), with the extended BLAGN having on average a lower redshift. Figure 3.14 shows that sixteen out of nineteen of these BLAGN have $z < 1.6$ and in this redshift range they constitute $\sim 42\%$ of the sample.

3.5.2 Color analysis

The classical way to create an optical BLAGN sample is to preselect candidates from a photometric catalog requiring that the objects are point-like and have blue colors. This selection criterion allows to select BLAGN candidates with an efficiency above 50% (see Croom et al. 2004), at least for objects brighter than B$\sim$21. This jump in efficiency –from less than 1% in a flux-limited sample without preselection to more than 50% with preselection – makes it possible to construct very large catalogs of several tens of thousands of BLAGN, such as the 2QZ.

The drawbacks of this selection criterion are:

(a) Its high redshift limit arises at about the same redshift where the cutoff of the BLAGN space density is observed, i.e $z \sim 2.3$;

(b) It excludes objects at low redshift, for which the contribution of the host galaxy is detected and resolved, thus introducing a bias especially toward the faint end of the BLAGN luminosity function.

To overcome this problem, various surveys adopted more complex selection algorithms based on multicolor analysis, estimating for each of them different levels of incompleteness. The SDSS QSO survey is the largest example of this kind of survey. Its completeness function is investigated in detail in Vanden Berk et al. (2005).

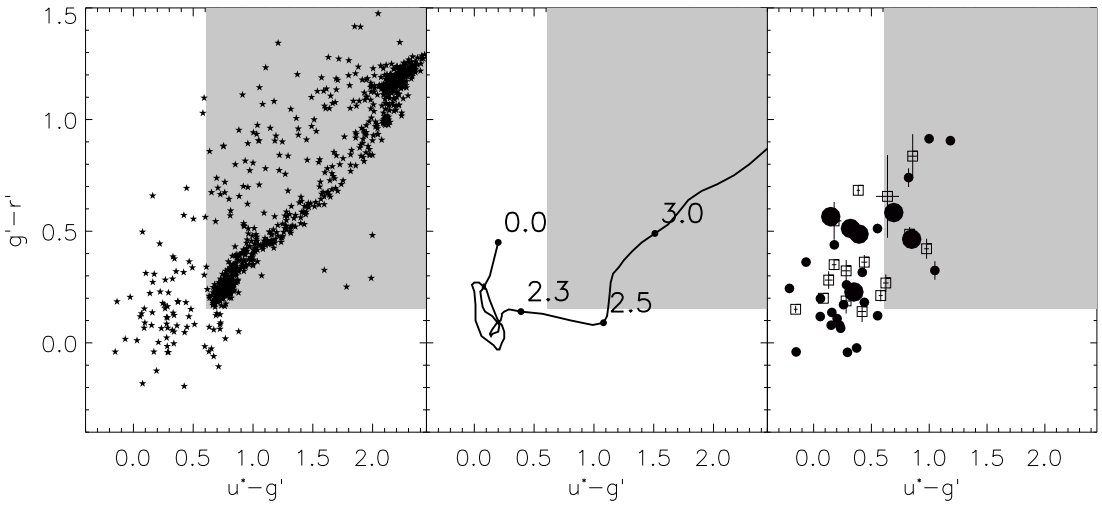

Figure 3.15: $u^* - g'$, $g' - r'$ color diagram. Left panel: location of the point-like objects in our photometric catalog. An exclusion area, reported in gray, is set to exclude most of main sequence stars. Middle panel: color evolutionary track with redshift of a BLAGN. The template considered here is the SDSS composite spectrum. Right panel: location of AGN with $z < 2.3$. AGN which could not be morphologically classified ($I_{AB} > 22.5$) are plotted with open boxes. AGN classified as extended are big dots while AGN classified as point-like are small dots.

We investigate here how a simple ultraviolet excess preselection technique based on three color bands would have applied to our sample. For this purpose we used the deep photometry obtained in the frame of the CFHTLS and we plotted our point-like objects in the color plane $u^* - g'$,$g' - r'$, as shown in the left panel of Figure 3.15. We could then set a color selection criterion meant to exclude most of the main sequence stars: (a) $u^* - g' < 0.62$; (b) $g' - r' < 0.16$. The exclusion area is reported in gray Figure 3.15.

Following the evolutionary track of a QSO template (here SDSS composite spectrum, Vanden Berk et al. 2001) in this color plane, we can expect our selection criterion to be efficient up to $z \sim 2.3 - 2.5$.

We observe now which fraction of the optical AGN population with $z < 2.3$ would have been missed by this selection criterion. Our AGN sample with $z < 2.3$ and photometric information in the u^*,g' and r' band is reported in this plane, Figure 3.15, right panel. We find that $\sim 25\%$ of the population of our optical BLAGN would have been excluded by this color selection. If we restrict now our analysis to a limiting magnitude of $I_{AB} < 22.5$, we find that $\sim 35\%$ of our AGN do not fulfill this color selection criterion combined with a morphological selection of point like objects.

We would like to emphasize that these completeness rates are found for our sample which is two to three magnitudes deeper than current major samples and do not necessarily apply to existing brighter samples.

Figure 3.16 presents the $B_{AB} - I_{AB}$ colors of our BLAGN sample as a function of redshift, for $z < 1.8$. The dispersion in color is large and most of our objects have a significantly redder color than that expected from the SDSS composite spectrum.

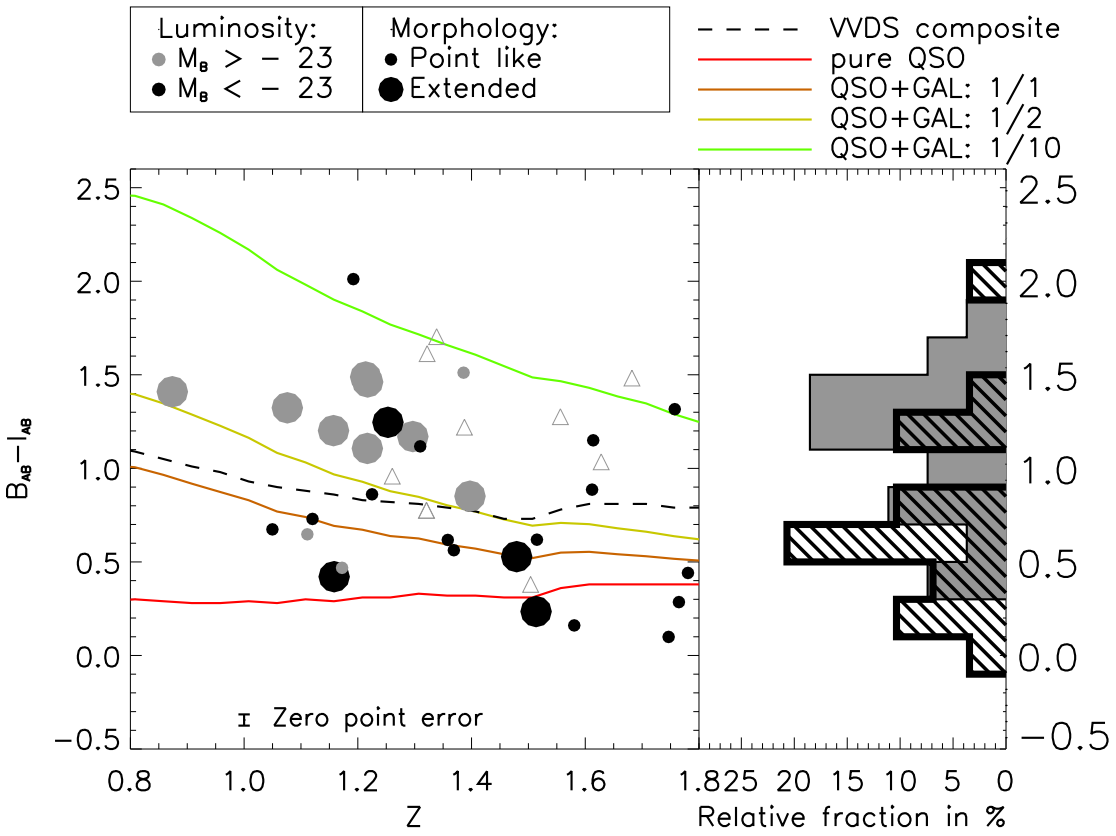

Figure 3.16: Observed $B_{AB} - I_{AB}$ color for VVDS BLAGN as a function of redshift. Black dots correspond to QSOs, while the gray dots correspond to Seyfert galaxies. The $B_{AB} - I_{AB}$ color histograms of these two populations are shown on the right. For comparison we report the evolutionary track for QSO mixed with various relative host galaxy contributions. The relative QSO/host galaxy flux ratio is fixed in the rest frame I-band to be 1/0 (red); 1/1 (dark brown); 1/2 (light brown) and 1/10 (green). The QSO template adopted is the SDSS composite spectrum (Vanden Berk et al. 2001)) while the galaxy template is a synthetic stellar population model with 1Gyr age (Bruzual & Charlot 2003). The dashed line correspond to the VVDS composite spectrum evolutionary track.

Moreover, the less luminous objects appear to have on average redder colors than the more luminous ones. A KS test applied on the color of the Seyfert galaxies ($M_B > -23$) and of the QSOs ($M_B < -23$) indicates a probability of only $\sim 1 \times 10^{-3}$ that these objects have the same color distribution.

This could be explained in different ways: (a) the contamination of the host galaxy is significantly reddening the measured colors of faint AGN; (b) BLAGN are intrinsically redder when they are faint; (c) the reddest colors are due to the presence of dust. With the present analysis we can not exclude or confirm hypotheses (b) and (c). However, we observe that for $\sim$ 60 % of our reddest AGN (objects with $(B_{AB} - I_{AB}) > 1$) we detect the extended component of the BLAGN host galaxy in I band. In this redshift range the contribution from the host galaxies is in fact expected to be more significant in the I band (corresponding to near UV-B rest-frame bands) than in the B band (corresponding to the far UV rest-frame band). We therefore believe that host galaxy contamination is contributing to give a redder color to our BLAGN, in particular at $z \lesssim 1.5$. Following this hypothesis we report Figure 3.16 the color evolution of our composite spectrum (see 3.6) as well as the one expected for various templates of mixed QSO/host galaxy light. For our mixed QSO/host galaxy light templates we consider a synthetic stellar population model of an early type galaxy with 1Gyr age Bruzual & Charlot (2003). The relative QSO/host galaxy flux ratio is fixed in the rest frame I-band, and the VVDS composite spectrum lie in between the mixed template for which the host galaxy contribution is once and twice larger than the one of the QSO. However, the evolutionary track of our composite spectrum is rather flat, as it would be exected from a pure power low spectrum (and in this case α_ν would be -1.2 which is significantly redder than the value observed for the SDSS QSO composite spectrum with $\alpha_\nu = -0.44$). In order to put stronger conclusion concerning the origin of this redder colors we will use the multiwavelength data available for some of our object in order to try to deconvolve the contribution to the light from the AGN, its dust obscuration and its host galaxy.

From this morphological and color analysis we conclude that *classical optical preselection techniques are significantly under-sampling the overall BLAGN population in deep samples*. This effect should be fully taken into account when deriving BLAGN volume densities or related quantities.

3.6 Composite Spectrum

Composite spectra are useful tools to characterize the mean spectral properties of a class of objects. They as well provide a reference to study the deviation from those properties in individual objects or bring in evidence differences between different samples characterized by different selection functions. For this different reasons we generated a composite spectrum of the VVDS AGN sample and present it in the following section.

3.6.1 Spectrophotometric calibration

One of the main concern when generating a composite spectrum is the accuracy of the flux calibration of the individual spectra used. Although the absolute flux calibration is not important, a systematic errors in the relative flux calibration could introduce a "color" bias in our composite.

As explained in Le Fèvre et al. (2005b) (see Figure 5), the quality of the spectrophotometric calibration of the VVDS spectra was measured by comparison of the magnitudes derived from the integrated flux spectra with the broad band photometric measurements coming from the deep imaging survey. The accuracy of the relative flux calibration over the complete spectral wavelength range is conserved at the 10% level and no systematic color trends are observed.

3.6.2 Generating the composite spectrum

The algorithm used to generate the composite, basically follow the method described in Francis et al. (1991).

The spectra were first transformed into rest-frame wavelengths and re-binned to 1 Å. The lowest redshift spectrum was taken as a starting point to build the long wavelength part of the composite. The spectra were then taken in order of increasing redshift and for each of them the spectral range in common with the composite was determined. The spectrum was rescaled to have the same average as the composite in this common spectral range. It was then added to the composite. Each contribution is weighted by the corresponding individual average S/N ratio. The co-addition is a geometric mean to preserve the continuum logarithmic slope (see Francis et al. 1991). Once all spectra are co-added a sliding Gaussian filter ($\sigma = 2$ Å) is applied to the composite to improve the S/N ratio.

Individual redshifts are slightly varied so as to maximize the peaks of each main emission line, then they are corrected to fix the line peaks close to their laboratory wavelengths. The entire procedure is iterated, the convergence being quite fast after 2 or 3 iterations.

All 115 BLAGN spectra with secure redshifts but one have been used to generate the composite. In particular, BAL spectra are included. The spectrum of object 000029274 at redshift 0.7352, is strongly affected by the residual noise of the fringing pattern and contributes to a wavelength range covered by only 5 other objects. For this reason, it was excluded to generate the composite.

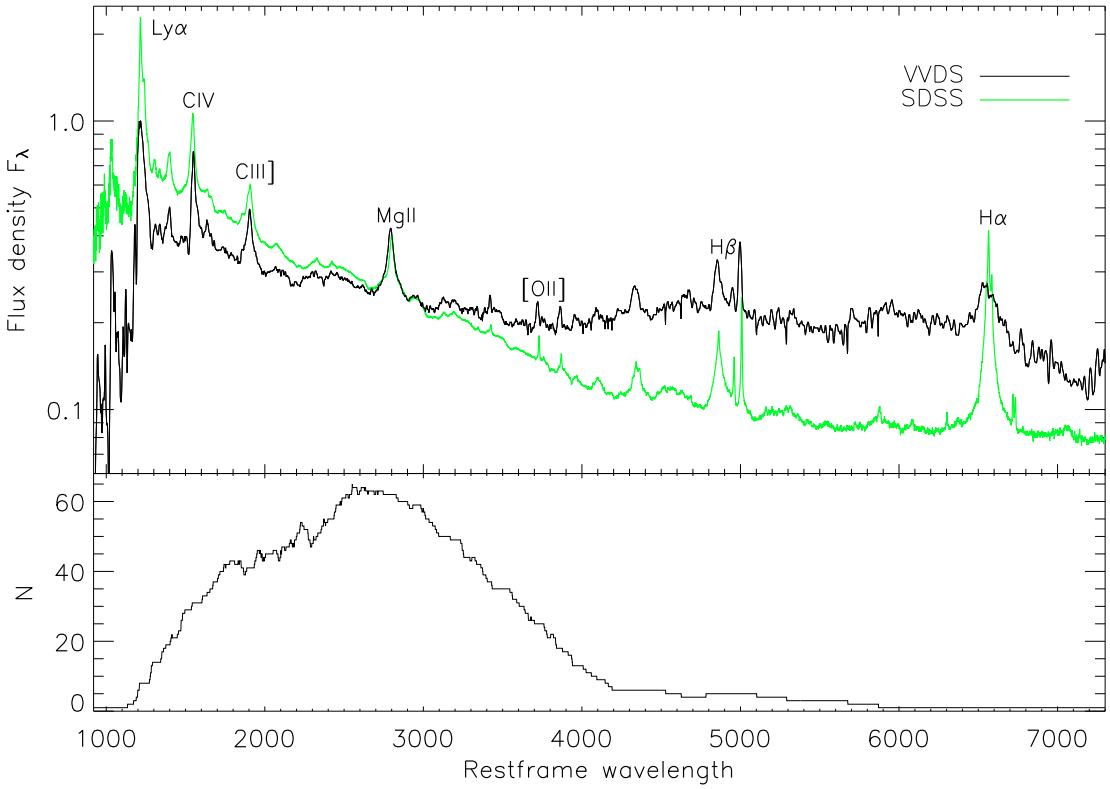

Figure 3.17: Composite spectrum . Top panel: Composite spectrum of the VVDS BLAGN with secure redshift (black) compared with the SDSS composite spectrum (gray or green in electronic version). Bottom panel: Number of contributing spectra as a function of wavelength.

3.6.3 Result and discussion

The final composite obtained is shown in Figure 3.17 along with the number of contributing spectra per wavelength bin. For comparison, the SDSS composite spectrum obtained with the same method over 2200 spectra is plotted over our composite (Vanden Berk et al. 2001).

The maximum number of individual spectra contributing to the composite is 64 near 2570 Å. At both wavelength ends, only a few objects contribute to the composite spectrum. The signal to noise is ~ 60 in the $2000 - 4000$ Å range and goes down to ~ 30 at larger wavelengths. We measured the EW of the main emission lines in the composite using the IRAF package[1]. Broad emission lines have been fitted by a Lorentzian profile while narrow emission lines were analyzed using a Gaussian. C IV and Lyα lines have been de-blended from their absorption components. The resulting EW values are given Table 3.2 and are compared to those of the SDSS composite spectrum.

Significant differences are seen in the EW of Lyα and Hα. The reason for such discrepancies is probably due to the large variety of EWs for the same line observed in QSO spectra, since very few objects are contributing at both ends of the VVDS

[1]http://iraf.noao.edu/

composite spectrum, 5 or less below 1200 Å and above 5050 Å. As demonstrated Section 3.2, at redshift $z \sim 1$ our sample can only select AGN from their Hγ emission line. This is possible either in very bright objects, either in objects with enhanced balmer lines. For this reason we interpret the large EW of the Hγ emission line to be caused by this bias.

We interpret the larger EW we obtain for the C IV,C III] and MgII lines as a consequence of the Baldwin effect (Baldwin 1977), our objects being a factor up to 100 times fainter than the ones of the SDSS sample (see Section 3.7).

The overall continuum shape of our composite spectrum is redder than that of the SDSS composite and this is particularly true at $\lambda > 3000$ Å. This can again be an indication that the host galaxy contamination is reddening our composite spectrum at long wavelengths. This result is consistent with the discussion made in Section 3.5.2 about the red colors we observe for our fainter objects.

To further check this interpretation, a new composite was computed excluding the extended objects found in our morphological analysis above, for which we expect the contamination of the host galaxy to be stronger. This composite of point-like BLAGN is indeed found to have a bluer continuum than our composite with the complete sample.

Finally, we subtracted the continuum of the SDSS composite spectrum from that of the VVDS composite; emission lines have been previously fitted and subtracted from both composite spectra.

The resulting difference is shown in Figure 3.18 together with the spectrum of the template of early type galaxies as derived from the VVDS data (Contini et al. 2006). The good agreement of the overall shape of the two spectra further strengthens our conclusion about the probable significant contamination of the red part of our composite spectrum by emission from the host galaxies.

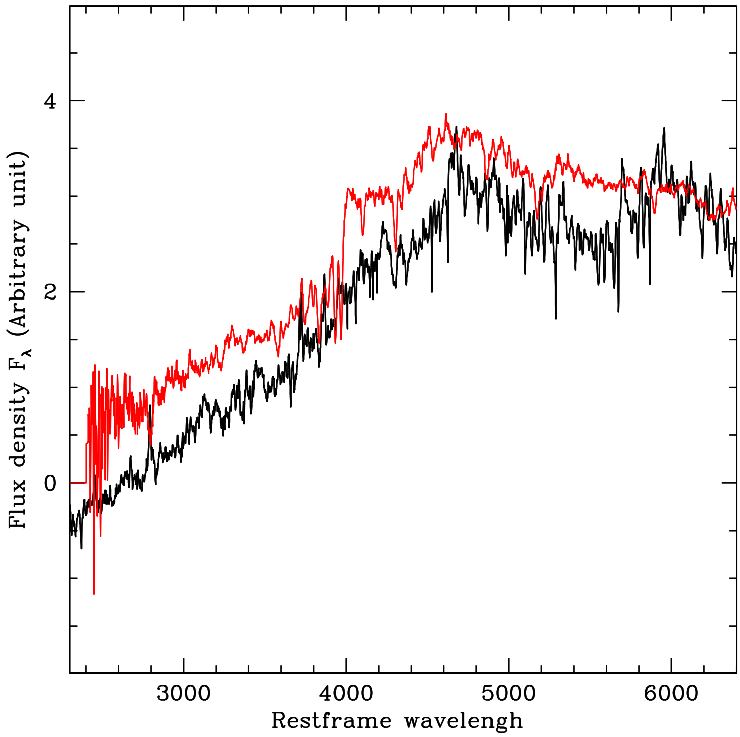

Figure 3.18: Difference between VVDS-AGN composite spectrum and the SDSS one. For comparison, the red line shows the template of early type galaxies as derived from the VVDS data.

Table 3.2: Rest-frame EWs and FWHM of the emission lines in the VVDS composite spectrum and their comparison to the corresponding lines of the SDSS composite spectrum.

Line	λ_0	EW (VVDS)	EW (SDSS)
Lyα+N v	1216+1240	137.4	92.91
Si iv+O iv]	1396+1402	7.9	8.13
C iv	1549	46.0	23.78
C iii]	1909	25.5	21.19
Mg ii	2798	40.3	32.28
[O ii]	3727	3.4	1.56
[Ne iii]	3869	2.7	1.38
Hδ	4103	5.0	5.05
Hγ	4342	21.8	12.62
Hβ	4861	33.8	46.21
[O iii]	4959	4.9	3.50
[O iii]	5007	16.8	13.23
Hα	6562	137.5	194.52

3.7 Baldwin effect

The recent discovery of scaling relations between the width of some broad-emission lines and the AGN powering black-hole mass opened a promising window for the study of black hole demography (Wandel et al. 1999, see Vestergaard & Peterson 2006 for a recent update). Taking this apart, the connections between AGN spectral properties and other physical parameters appear to be relatively complex and are still poorly understood. In fact, it is currently not possible to discriminate the various BLR models from the observed QSO line properties. However, instead of comparing directly models with average line profile it is possible to study the correlation of various observed spectral quantities. For this purpose, Boroson & Green (1992) applied the technique of *Principal Component Analysis* to a sample of 87 QSO of the PG survey and found that most of the variety of spectroscopic properties was related to two set of correlations. The first one, "Eigenvector 1", was originally found as an anti-correlation between the prominence of the [O III] line doublet and the Fe II emission. It consists in fact of a larger set of correlation that will not be considered here. The second one, "Eigenvector 2" concerns the anti-correlation of high ionization line strength with continuum luminosity. This anti-correlation was already known as "Baldwin effect", and was first pointed out in the case of the C IV emission line (Baldwin 1977).

We derived for individual AGN various parameters characterizing the dominantly observed EL in the VVDS spectra; the C IV, C III], Mg II broad emission lines as well as of the Fe II line complex and we present here our first results concerning the Baldwin effect (hereafter BEff).

3.7.1 Measurements

Table 3.3: For each emission line we indicate the continuum windows considered to normalize the spectra, the integration limits used to measure equivalent width as well as a limiting continuum S/N under which emission lines measurements are flagged as "low quality".

Line	Continuum windows [Å]		Integration limits [Å]	S/N
C IV	1425–1470	1680–1705	1500–1590	7
C III]	1770–1820	1950–2050	1850–1945	10
Fe II	2230–2260	2650–2670	2300–2600	20
Mg II	2640–2670	3010–3060	2680–2900	7

Spectra normalization and quality flags

The local continuum was estimated by fitting a simple slope in the windows listed table 3.3. In the cases where the continuum could be estimated only from one side of the emission line, a constant continuum level was considered. In a very limited

number of spectra, this normalization had to be manually adjusted to avoid spurious features.

Additionally, we measure the continuum S/N close to the emission lines for each spectrum. In the following analysis, we flag as "low quality" objects with the lowest S/N: For the strongest emission lines: C IV and Mg II we give this "low quality" flag to objects with S/N<7, whereas for the fainter C III] emission line we apply this flag for objects with a S/N lower then 10. The equivalent width measurement of the Fe II line complex is more sensitive to noise and normalization accuracy, for this reason we consider spectra with a continuum S/N lower then 20 as "low quality" spectra. Those limits are reported Table 3.3.

Equivalent width measurement

Rest-frame EW are measured by integrating the flux density of the normalized spectrum under the wavelength range given table 3.3.

Out of the 29 C IV profile analyzed hereafter, 8 present absorption in their blue wing[2]. Ideally one would estimate the EW of these line either from a de-blended fit of the emission and absorption component, either from the red wing of the line. However, in all our objects these multi-component absorption were too strong to constrain our fit and it is not clear whether the absorption component extend over the red wing of the lines. For these reason we choose the conservative approach to derive only a lower limits constrain on the EW.

3.7.2 The magnitude-EW relation

The individual emission lines profiles and our measurements are presented in Appendix D.

Figure 3.19, presents the distribution of EW for each emission line.

We compute the mean EW of all the profiles, excluding "low quality" spectra. The dispersion around this mean EW is taken as the mean deviation of the distribution divided by the square root of the number of measurements of that line. This is reported Figure 3.19 and Table 3.4.

Rather then considering spectroscopic magnitude for this work, we use photometric magnitudes.

To study the distribution of emission lines EW with absolute magnitude we need to consider all our objects, in particular the ones flagged as "low quality", since they are sampling the fainter luminosities. However the EW measurement in the lowest signal to noise spectra is associated with large uncertainties (in a few cases S/N< 3, in the continuum). To overcome this problem we decided to stack emission line profiles. In this way we can obtain a profile with a reasonable signal to noise which contains as well the information of the faintest objects. For each line we divide our objects in a "bright" and a "faint" [3] sample and combine all the profile. We obtain

[2]In fact, this is not true in the case of the BLAGN 020351846; this singular object presents an absorption feature mostly on the red wing of its C IV line.

[3]Obviously, we refer in this section to *intrinsic* brightness.

Figure 3.19: Histograms of rest-frame equivalent width from the VVDS individual spectra. The shaded histogram corresponds to good quality spectra whereas the distribution of all measurement, including "low quality" spectra is unshaded. Over-plotted are the mean EW of the distribution (dashed line) and its dispersion (dotted line). For comparison, we report the EW measured in the VVDS composite spectrum (thick arrow) and in the SDSS composite spectrum (thin arrow).

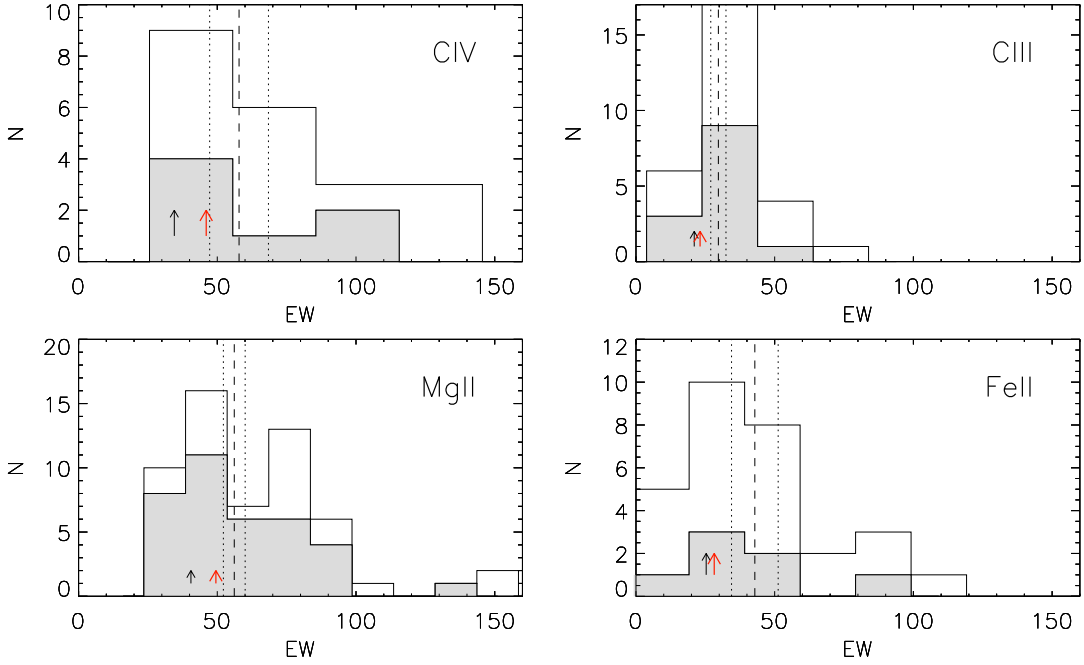

Table 3.4: Rest-frame EW derived from our data and from the SDSS composite spectrum. Column (a) gives the mean equivalent width measured in our spectra excluding objects flagged as "low quality". The mean error bars are derived from the distribution of EW (see text). n corresponds to the number of objects considered. Column (b) gives the EW measured in the weighted-mean "faint"-objects stacked profile, while column (c) corresponds to the "bright"-objects stacked profile. Column (d) and (e) give respectively the EW measured in the VVDS and SDSS composite spectra.

Line	(a) Mean EW [Å]	n	(b) Faint comp. [Å]	n	(c) Bright comp. [Å]	n	(d) VVDS comp. [Å]	(e) SDSS comp. [Å]
C IV	57.9±10.6	7	73.4±10.9	10	47.2±8.3	11	~ 46.0[1]	34.5
C III]	29.7±2.7	13	31.0±4.9	12	26.2±3.3	17	23.1	21.0
Fe II	42.8±8.4	7	46.4±11.2	18	39.1±6.3	12	28.2	25.3
Mg II	56.1±3.9	36	58.2±6.4	30	57.0±5.9	27	49.5	40.5

[1]BAL QSO are not excluded from the VVDS composite spectra and an absorption component is present in the C IV emission line. We cannot therefore measure the EW of this line with a simple integration. A de-blended fit of this line suggest an equivalent width of ~ 46 Å.

Table 3.5: Slope β of the Baldwin Effect for the individual emission lines: log EW $\propto \beta(\pm d\beta)$ Mb. Comparison with other observational studies are given for Kinney et al. 1990 (K90), Zamorani et al. 1992 (Z92), Dietrich et al. 2002 (D02), and Croom et al. 2002 (C02).

Line	VVDS	K90	Z92	D02	C02
C IV	0.097 (± 0.052)	0.068	0.051	0.056	0.051
C III]	0.039 (± 0.047)	...	...	0.036	0.028
Fe II	0.034 (± 0.057)	...	...	0.008	...
Mg II	0.042 (± 0.037)	...	0.030	0.036	0.023

the same qualitative results when combining our flux profile with a median, mean or S/N-weighted-mean algorithm. Each one of this method having its advantage and drawback, we finally choose to present here the S/N-weighted-mean profile. This method provides the best resulting S/N but is biased in each sub-samples towards the higher S/N spectra. The obtained EW are reported Tables 3.4. The error term which dominates the EW obtained from this method, is not the uncertainty in the EW measurement of the stacked profile but the uncertainty induced by the large scatter in EW observed in individual objects. For this reason, the error bars are derived from the dispersion of EW width measured in individual spectra divided by the square root of the number of objects.

Figure 3.20 present our results. The absolute magnitude cut between our "faint" and our "bright" sample is set in order to have a comparable number of contributing spectra in both magnitude bins. From this figure we can see that no significant difference between "bright" and "faint" profiles is seen in the case of C III], Mg II and Fe II lines. In the case of the C IV emission line we observe however a larger equivalent width for the "faint" emission line profile.

The linear relation passing through the two points obtained following this method is described as following:

$$\log \mathrm{EW}_{\mathrm{C\,IV}} = 4.053(\pm 0.243) + 0.097\mathrm{Mb}$$
$$\log \mathrm{EW}_{\mathrm{C\,III]}} = 2.371(\pm 0.151) + 0.039\mathrm{Mb}$$
$$\log \mathrm{EW}_{\mathrm{Fe\,II}} = 2.412(\pm 0.232) + 0.034\mathrm{Mb}$$
$$\log \mathrm{EW}_{\mathrm{Mg\,II}} = 2.711(\pm 0.182) + 0.042\mathrm{Mb}$$

The dispersion indicated here do not correspond to our error bar but to the 1σ scattering of the BEff: it is the dispersion of our individual EW measurements (excluding "low quality" flag) with respect to the magnitude-EW relation. This dispersion intrinsic scattering is reported in Figure 3.21 with a shaded area.

Uncertainties on our slope, computed from the standard error propagation equation are indicated Table 3.5.

From this analysis we observe marginal evidence of evolution with magnitude of $\mathrm{EW}_{\mathrm{C\,IV}}$ and $\mathrm{EW}_{\mathrm{Mg\,II}}$ respectively at the 1.9σ and 1.1σ level. There is no evidence for evolution of $\mathrm{EW}_{\mathrm{Fe\,II}}$ and $\mathrm{EW}_{\mathrm{C\,III]}}$ as function of luminosity.

Figure 3.20: Left: EW of the C IV,C III],Mg II emission line, and of the Fe II line complex as a function of absolute magnitude. Open circles correspond to all measurements, filled circle correspond to spectra with a S/N above our threshold. The EW lower limits derived from absorbed emission lines are figured with arrows. Objects plotted in red are staked into our "bright" composite profile, object plotted in black are stacked in our "faint" profile. The equivalent width measured in those profile is reported with a solid line while the dotted line show the $\pm 1\sigma$ dispersion of the different EW in each sample divided by the square root of the number of objects. Right: Composite mean-weighted profile of our spectra separated in a "faint" and a "bright" sample.

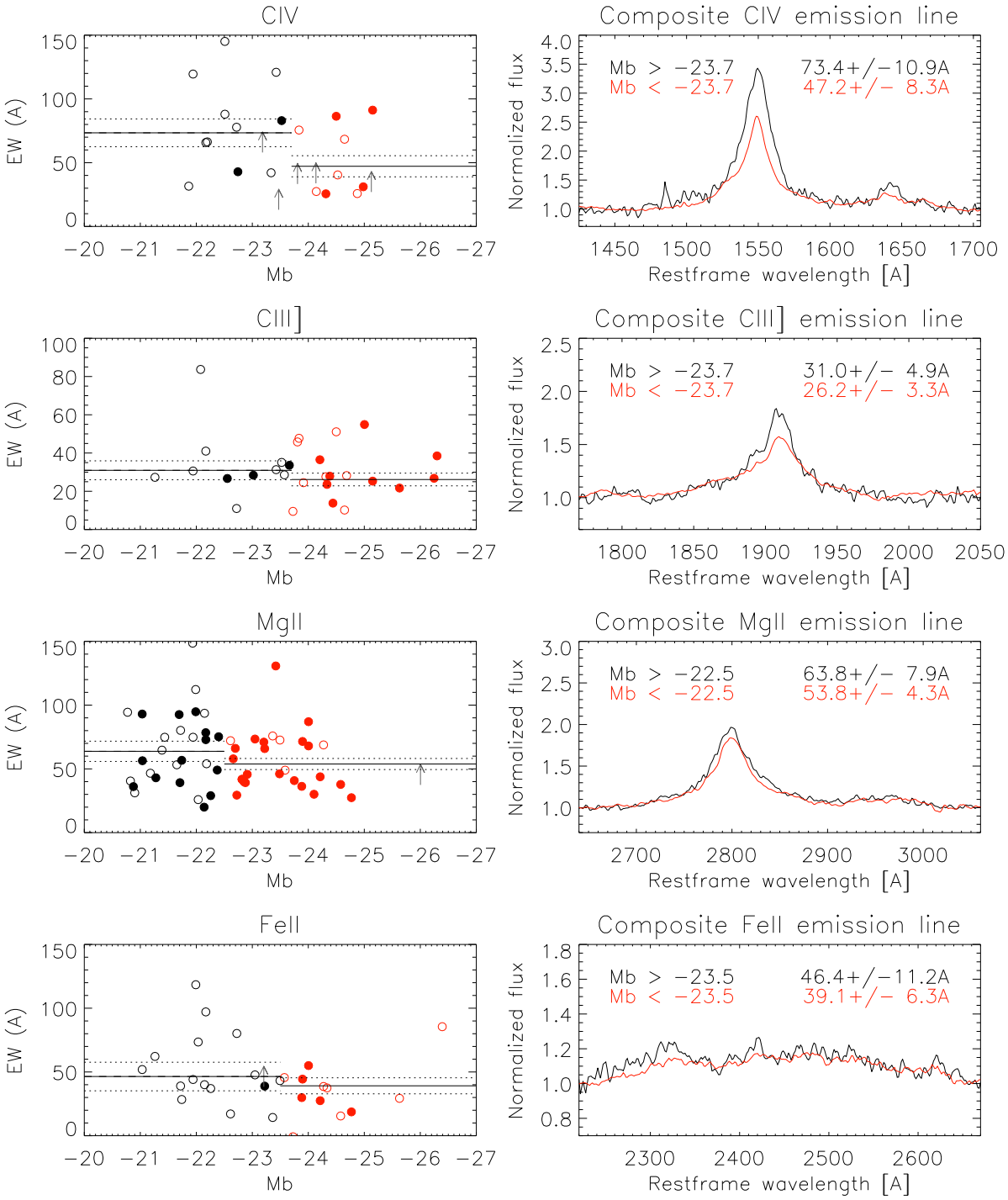

3.7.3 Comparison with previous studies

We report Table 3.5 and Figure 3.21 the work of Kinney et al. (1990), Zamorani et al. (1992), Dietrich et al. (2002), and Croom et al. (2002).

Croom et al. (2002) studied the BEff using over 22 000 individual QSO spectra obtained from the 2Qz and 6Qz surveys. This work consider by far the largest number of objects and is selected from a coherent set of data.

We compare as well our result to three other work, based on smaller numbers of objects but which encompass AGN selected from various techniques and cover a larger range of redshift and luminosities.

Kinney et al. (1990) studied the BEff for C IV (and Lyα) from a sample of quasar spectra gathered from the International Ultraviolet Explorer (IUE) satellite archives complemented, for higher redshift by ground-based studies. Their objects span a redshift range lower that the one of the VVDS ($z \leq 2.2$) but covers similar intrinsic magnitudes. Taking advantage of multiple observations of some AGN they can reduce the scatter of the relation induced by variability and measure the intrinsic BEff for some of their objects. Dietrich et al. (2002) measured the BEff for various high ionization line from a sample of over $\sim$ 800 type-1 AGN. Their spectra are provided by a compilation of ground-based and space-based observation. In contrast with these two studies, Zamorani et al. (1992) base their study of the BEff (for C IV and Mg II) on a set of *complete* optically selected of quasars with ground-based spectra.

To bring the absolute magnitudes of these last three works to our cosmology, we adopt a global correction for the luminosity distance modulus and consider that the slope of the Baldwin relation is not strongly affected by cosmology assumption. This approximation is found to be accurate for all the AGN considered by Zamorani et al. (1992), and most of the objects studied by Dietrich et al. (2002). However the magnitude correction adopted to bring the work of Kinney et al. (1990) in our cosmology is not correct over the large redshift range of their objects (see intervals of redshift indicated Figure 3.21). We set the correction in order to provide a compromise between low redshift and hight redshift objects. Qualitatively we expect that the slope of their relation slightly flattens in our cosmology. Color term corrections are obtained, assuming a power-law SED of index $\alpha_\nu = 0.5$.

The values derived for the slope β of the BEff in our sample is in good agreement with values quoted in these works. Nevertheless β is found to be systematically larger in our sample, this marginal effect been at the $\lesssim 0.9\sigma$ level in the case of C IV.

In the case of C IV Zamorani et al. (1992) found at a given magnitude values of $\mathrm{EW_{C\,IV}}$ significantly smaller than the one of Kinney et al. (1990) and later Dietrich et al. (2002) (factor $\sim$ 2). In this work we obtain intermediate values of $\mathrm{EW_{C\,IV}}$ consistent with the reference set by Croom et al. (2002).

We remark that the data point set by our "bright" composite is always found to be consistent with the relation obtained in Croom et al. (2002). This point samples the faint end of the magnitude range considered by this work. The data point set by our "faint" composite however correspond to a luminosity range not covered by this work and is marginally found to deviate from their relation, towards higher EW

Figure 3.21: Comparison of the BEff observed in the VVDS sample with previous studies. The two dots corresponds to the EWs derived from our "bright" and "faint" emission line composite profile. Error bars correspond the standard deviation of EW and magnitude of the N individual objects divided by $\sqrt{N}$. The shaded area correspond to the 1σ dispersion observed in our sample with respect to the magnitude-EW relation. Relation derived from previous work are as well presented. Blue dashed line: Kinney et al. (1990); green solid line: Zamorani et al. (1992); red dotted line Dietrich et al. (2002); violet dotted-dashed line Croom et al. (2002). **Important remark:** we do not consider exactly the same set of Fe II lines as Dietrich et al. (2002) and their relation zero point is set arbitrarily.

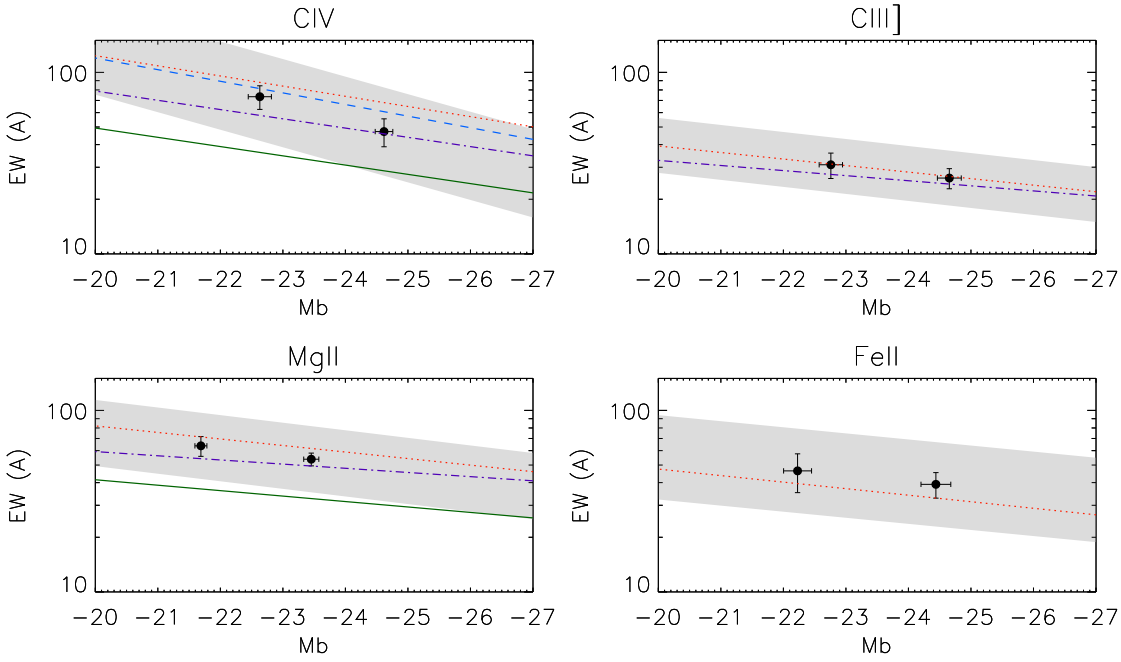

Magnitude correction applied due to cosmology: $M_{new} = M_{old} - \Delta M$.
We indicate in parenthesis the redshift range in which the deviation to this correction is lower then 0.2 magnitude.

- Kinney et al. 1990: $\Delta M = -0.3$ for C IV $(0.8 < z < 1.7)$;
- Zamorani et al. 1992: $\Delta M = -0.7$ for C IV $(1.8 < z < 4.1)$; $\Delta M = -0.45$ for Mg II $(1.05 < z < 2.5)$;
- Dietrich et al. 2002: $\Delta M = 0$ for all lines $(0 < z < 4.1)$;
- Croom et al. 2002: We consider the same cosmology.

values.

The EW we observe in the case of Mg II are as well higher than the one quoted by Zamorani et al. (1992). Since we observe more object in the case of this emission line, this difference is significant, at the 4 σ level. The transfer of cosmology can not account for all the discrepancy found. One source of systematic effect might be the method employed to measure equivalent width: for example fitting emission lines with a given profile leads to different results than a plain integration of the flux under the line. This can however not explain the large factor observed.

Dietrich et al. (2002) measure the EW of Fe II in a larger wavelength range then the one considered here and for this reason we can not compare our absolute EW values but find consistent slope. Our relation is consistent with their in the case of C III] and Mg II.

3.7.4 Discussion

In his original paper Baldwin (1977) pointed out a strong anti-correlation between luminosity and $EW_{C\,IV}$. This was suggesting that QSO could have been used as cosmological standard candles. However it was soon realized that the dispersion in this relation had been under-estimated and the slope itself of the relation was not as steep as previously thought (Kinney et al. 1990; Zamorani et al. 1992). The statistical weakness of this correlation lead, in fact, to several counter claim of the Baldwin effect (e.g. Jones & Jones 1980). As pointed out by Baldwin himself, it is quite conceivable that the apparent fainter QSO, sampling as well the intrinsically fainter population, will be preferentially identified when they have a strong $EW_{C\,IV}$. This selection effect clearly apply to our sample. However the fact that we detect and identify objects on the basis of their C III] emission line which have much smaller observed $EW_{C\,III]}$ then the cut observed in our observed $EW_{C\,IV}$ distribution (e.g: object 020212038), gives evidence that type-1 AGN with fainter $EW_{C\,IV}$ could have been detected in our sample. Simulation suggest that for a S/N of 8, a C IV emission line of Ew larger than 9 can be detected (Appendix C, Figure C.1). Nevertheless this does not apply to the faintest spectra in which only large EW can be detected. Such a bias might partially account for the fact that we derive systematically steeper Baldwin relation than previously quoted. On the other hand, the VVDS is probing the BEff in a luminosity range only previously studied for lower redshift objects and a steepening of the BEff with redshift is not excluded (see Dietrich et al. 2002). Our analysis of the selection function, in particular the automated tool developed to estimate our *spectroscopic success rate* (Section 3.2.2) can we used to derive some constrains on our bias towards high EW AGN. Moreover, including the ~ 100 new AGN recently selected in the VVDS survey will allow us to sub-divide our spectra in more than 2 samples and give a clearer idea of the significance of this result.

Currently, several models have been suggested to understand the origin of the BEff and its observed dispersion (e.g. luminosity dependant SED, luminosity dependent covering factor). The mechanism is still unclear but observational constrains will help to discern in between the different process. Understanding the BEff is

therefore not a quest limited in itself but will bring some general insight of accretion disk's physics.

3.8 Luminosity Function

This section gives a short insight of the first results obtained on the evolution of the VVDS BLAGN luminosity function. This project is leaded by A. Bongiorno and G. Zamorani. My main contribution for this work was to determine the selection function of our sample (Section 3.2.2).

3.8.1 Definition of the Luminosity Function

A major aim of cosmology is to study how our universe is evolving with time. This is done by observing how its content is evolving with time. For this the Luminosity Function (LF) is a major tool. This function correspond to the density of objects of a given magnitude, at a certain redshift:

$$\Phi(M, z) = \frac{dN(M, z)}{dMdV} \ ,$$

where dN is the number of object of magnitude $M \in [M, M + dM]$ and redshift $z \in [z, z + dz]$, this redshift interval enclosing the elementary volume dV.

3.8.2 Scientific background

Schmidt (1968) could already establish with a sample of 40 objects that the distribution of QSO is strongly evolving with redshift. For this purpose, he adapted the V/V_{max} test to a cosmological context. The basic idea of this test is the following: for an object i of absolute magnitude M_i selected in a flux limited survey, one can compute the maximal luminosity distance $d_{max,i}$ for which this object could have been detected in this sample. We define V_i as the volume enclosed by the actual distance d_i of this object and $V_{max,i}$ as the volume enclosed by $d_{max,i}$. For a sample of object homogeneously distributed, the mean value $< V/V_{max} >$ should be found to be 0.5. In his sample Schmidt measured $< V/V_{max} > \sim 0.7$ and interpreted this result has an evolution of the density of QSO with redshift. This model is referred as *pure density evolution*. Mathez (1976) showed that this result could as well be interpreted in terms of luminosity evolution. In this model, referred as *pure luminosity evolution*, highly luminosity quasars observed at redshift 2 are seen as a parent population, fading with time, of today's quasar characterized with a low luminosity.

Currently, up to a redshift of 2.5 the LF of optical AGN can be described to a very good precision by the pure luminosity evolution model (Croom et al. 2004) but this simple model fails to work beyond the quasar density peak, for $z \gtrsim 3$ (Richards et al. 2006b). However, most optical survey are more or less complete for $z \lesssim 2.2$ or for $z \gtrsim 3.6$. Within this redshift, instead, confusion arises among stars and compact galaxies in broad-band colors. It is precisely in the redshift range 2–3 that QSO activity show a maximum. The COMBO-17 is the only optically selected sample bracketing this peak of activity. Wolf et al. (2003) could observe this peak and describe the luminosity function of optical faint AGN either with a pure luminosity evolution, or with a pure density evolution.

On the other side, X-ray catalogs request a luminosity dependant density evolution model: in this interpretation more luminous AGN density peak at higher redshift than the less luminous ones. This effect, in apparent contradiction with the general hierarchical frame-work, is referred to as "down-sizing" (Page et al. 1997; Miyaji et al. 2000; Hasinger et al. 2005).

In this context, the VVDS AGN sample gives the opportunity to study the type-1 AGN activity peak and to observe whether at low luminosity, optically selected AGN follow the trend seen in X-ray surveys.

3.8.3 Computing the binned luminosity function

The computation of the binned luminosity function is done with a dedicate code, based on the classical non-parametric $1/V_{max}$ estimator (Schmidt 1968).

Absolute magnitudes are derived from the I_{AB} observed magnitude. To compute the K-correction term, we assume that the SED of our objects is well describe by the LBQS composite spectrum (Francis et al. 1991).

Because of our incompleteness at redshift $0.5 < z < 1$ (see Section 3.2), and of the low number of objects with $z < 0.5$, we restrict our redshift range to $z < 1$, this correspond to 119 AGN.

Currently, AGN with a degenerate redshift are distributed with equi-probability at their different redshift solutions, thought a weight w^D. Objects are corrected for incompleteness through the weights described Section 3.2, w^{TSR} and w^{SSR}.

The different fields of the VVDS are considered to be part of a coherent sample, following Avni & Bahcall (1980) and the luminosity function is computed in different redshift bins as follows:

$$\Phi(M) = \frac{1}{\Delta M} \sum_{M-\Delta M}^{M+\Delta M} \frac{w_i^{TSR} w_i^{SSR} w^D}{V_{i\,max}} \qquad \text{(Schmidt 1968)}$$

Where $V_{i\,max}$ is the volume in which the object i could have been detected. The error bars are :

$$\sigma_\Phi(M) = \frac{1}{\Delta M} \sqrt{\sum_{M-\Delta M}^{M+\Delta M} \left(\frac{w_i^{TSR} w_i^{SSR} w^D}{V_{max}} \right)^2} \qquad \text{(Marshall 1985)}$$

The assumption made by this method is that the LF is uniform in the magnitude and redshift bins considered and some biases are introduced in the case of a steep luminosity function.

3.8.4 First results and discussion

Figure 3.22 presents the binned LF of the VVDS sample compared to other surveys for different redshift bins. In the lowest redshift range (top left panel, $1.0 < z < 1.55$) for $M_B \leq 20.5$ we find a good agreement with the 2SLAQ survey (Richards et al. 2005) suggesting a larger number of low luminosity AGN than predicted by others

optical QSO surveys, like the COMBO-17 or 2Qz surveys. At the magnitude $M_B = -22$, this correspond to a factor of ~ 3. However, at higher redshift our LF flattens and we observe less low-luminosities AGN than the 2SLAQ sample. We are, in turn, in excellent agreement with the COMBO-17 survey in our intermediate and high redshift range (middle, $1.55 < z < 2.1$ and right, $2 < z < 3.6$).

Figure 3.23 presents, in turn, a comparison of the binned luminosity function with the X-ray selected QSO sample of Barger et al. (2005). This figure show that we probe luminosities sufficiently faint to observe the down-turning of the luminosity function, as observed in the hard X-ray luminosity function.

We expect the luminosities computed from our sample to be biased for $z \lesssim 1.6$. Although we still need to quantify this effect, we can qualitatively expect that AGN entering the galaxy luminosity function, with $M_B \gtrsim -22$, will have lower luminosities than the one we use. If all AGN host galaxy had the same luminosity this should steepen the luminosity function for brighter magnitudes than this luminosity and cause a break with a turning down of the LF for fainter magnitudes. This possible bias might cause the turning down observed in our lower redshift range, though this turning down seems to be seen as well in the X-ray selected sample.

This work will be presented in Bongiorno, Zamorani, Gavignaud et al. (2006) together with further results of parametric models fitting.

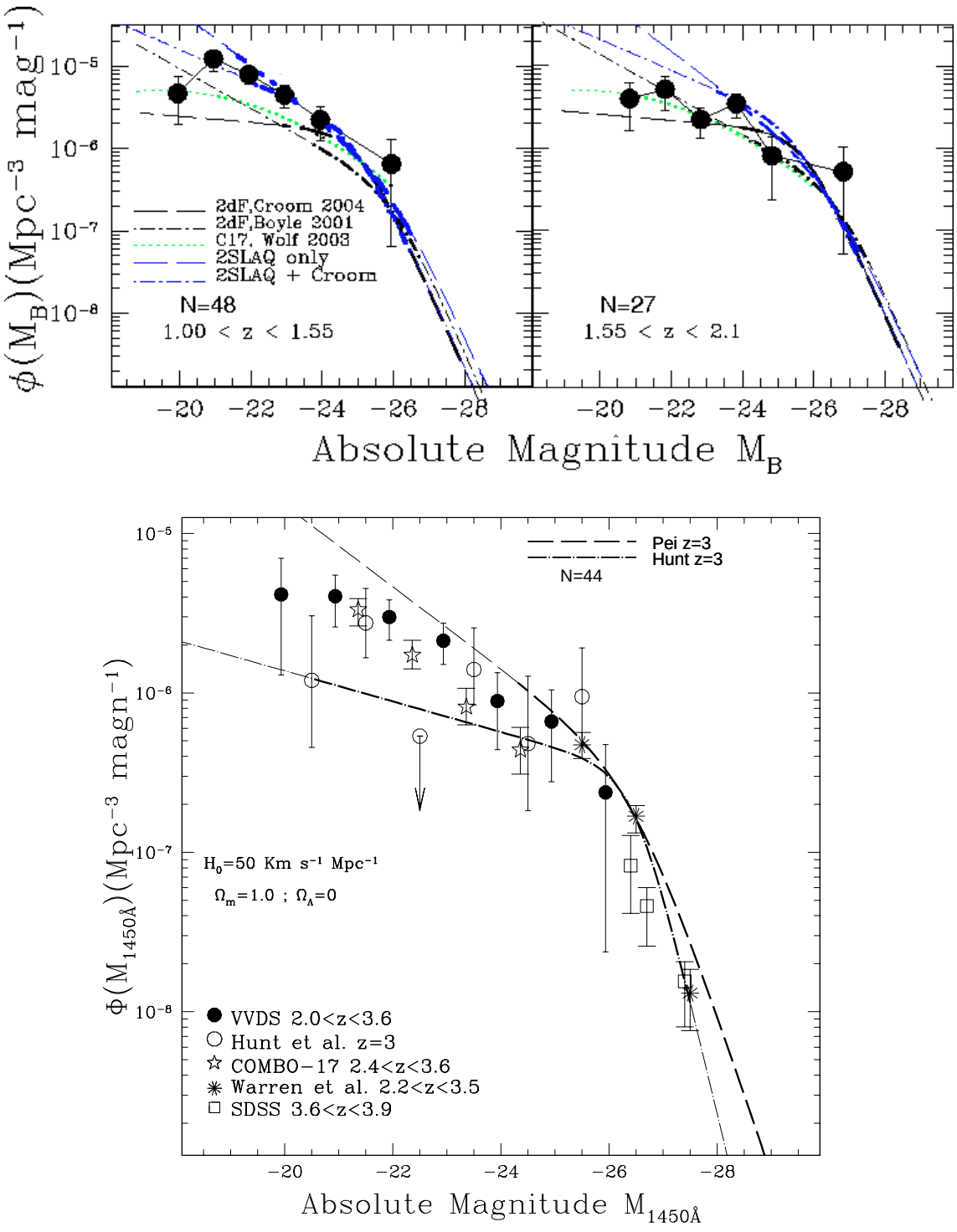

Figure 3.22: Comparison of the VVDS LF with other QSO surveys in the redshift bin $1 < z < 1.55$(Top left),$1.55 < z < 2.1$(top right), $2 < z < 3.6$ (bottom). The VVDS binned LF is plotted with black filled circles. Thick lines correspond to the magnitude ranges covered by the respective sample and thin line correspond to extrapolated values. Top: comparison with the following samples: 2Qz Croom et al. 2004 (black long-dashed lines), Boyle et al. 2000 (black long-and-short-dashed lines), COMBO-17 Wolf et al. 2003 (green dotted line), 2SLAQ (blue long-dashed line), and 2SLAQ and 2Qz (blue long-and-short-dashed lines) Richards et al. (2005). Bottom: references can be read in the caption.

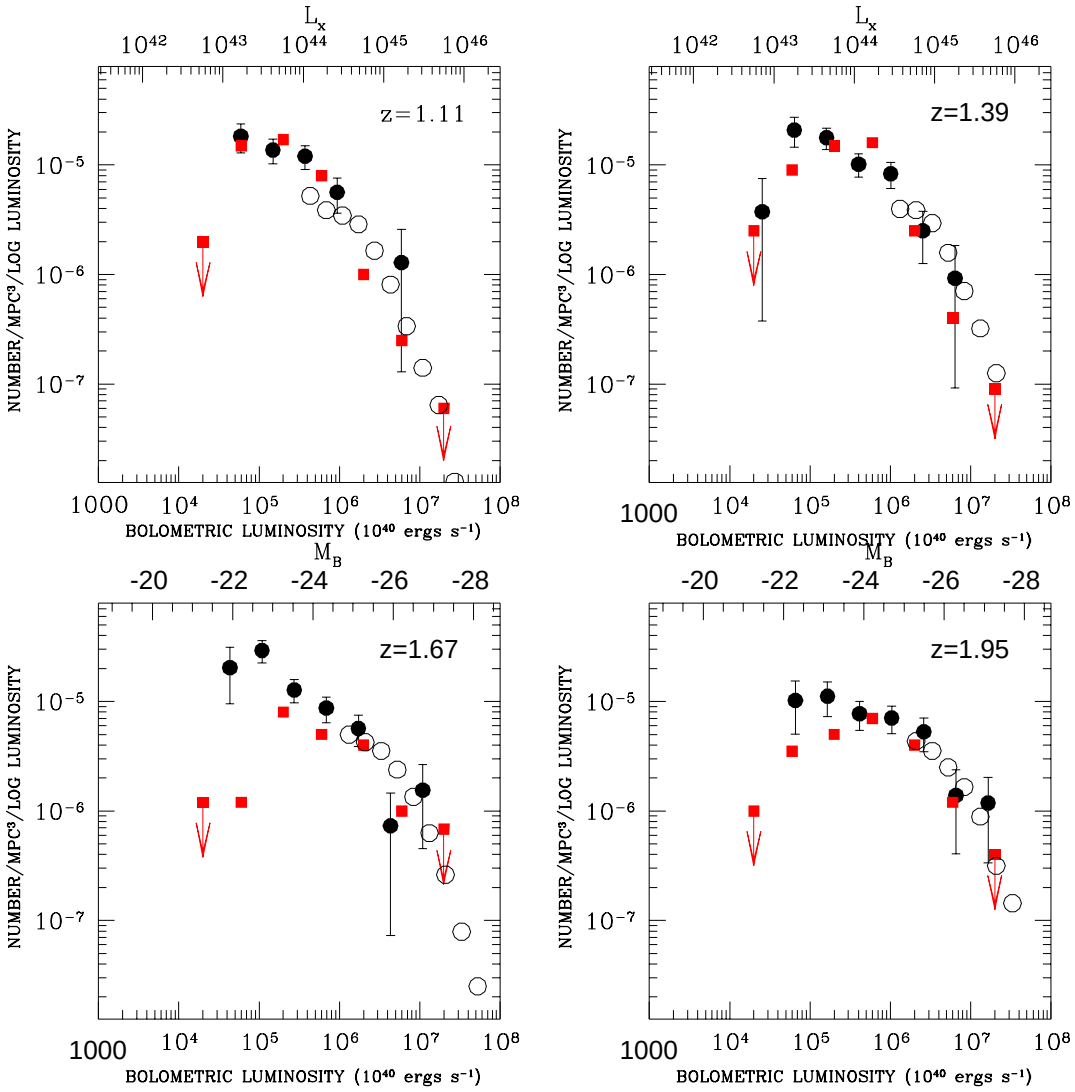

Figure 3.23: Comparison of the binned LF of the VVDS sample (black filled circles) and 2Qz LF from Croom et al. (2004) (open circles) with the Barger et al. (2005) hard X-ray LF (red filled squared). The rest-frame 2-8 keV luminosity function is given in unit of logarithmic luminosity. Optical M_B magnitudes and hard X-ray luminosities are converted to bolometric luminosities. A constant ratio between optical and X-luminosities is considered. The redshift intervals for the 2Qz and hard X-ray LF are: [3.97–1.25];[1.25–1.53];[1.53–1.81];[1.81–2.10]. For the VVDS we considered broader redshift intervals ($\Delta z = 1$) centered in the same medium redshift. In this case, we have [0.61–1.61];[0.89–1.89];[1.17–2.17];[1.45–2.45].

3.9 Black hole masses and accretion rates

At a given redshift most of the SMBH are non-active. Unfortunately for observers, the signature left by dormant black holes is only visible in the stellar and gas kinematics of their host galaxy's core, on scales of $\lesssim 100$ parsecs. For this reason the SMBH mass function can only be studied in the local universe.

It is however possible, with reasonable assumption, to estimate the black hole mass of active galactic nuclei. This potentially gives us the opportunity to shed light on the nature of black holes which are causing the steepening of the luminosity function at low redshift. Are these AGN caused rather by very small black holes accreting at their Eddington limit or, at the contrary, by very massive black holes accreting at low Eddington ratios? We will describe in this section the method employed to derived BH masses and will try to address this last question. The results presented here are still preliminary.

3.9.1 Black hole masses estimates

The Virial assumption

The black hole mass estimate of AGN rely on the assumption that the gas motion in the BLR is dominated by the central object gravitational potential. The black hole mass given by the virial equation is then:

$$M_{BH} = \frac{fR\Delta V^2}{\mathcal{G}} \tag{3.4}$$

where R is the size of the BLR, ΔV is the velocity dispersion, $\mathcal{G}$ is the gravitational constant and f is a unit-less factor close to unity which depends of the unknown geometry and kinematics of the BLR.

In equation 3.4, ΔV, correspond to the velocity of the clouds, and is, in general, estimated from the emission-line width: in the case of orbits randomly distributed in a spherically symmetric distribution $\Delta V = \frac{\sqrt{3}}{2} \times FWHM^2$ (Netzer 1990). ΔV can therefore be estimated from a simple spectrum of the AGN. However it is not straightforward to deduce the size R of the non-resolved BLR. This can be estimated by the mean of "reverberation mapping" proposed by Blandford & McKee (1982).

Reverberation mapping

This method takes advantage of AGN emission variability to map the emission line region. The size of the BLR can be estimated by measuring the mean time delay τ of broad-emission line variation relative to continuum variations. Within the assumption that the galactic nuclei continuum source is emitted from a central region of negligible size compared to the one of the surrounding broad-emission line region, then $R = c\tau$.

Black hole masses deduced from this method are supported by two observations: (1) In AGN for which time delays where measured for different emission lines, one

Figure 3.24: Example of a single peak (left) and a double peak (right) C IV emission-line profile.

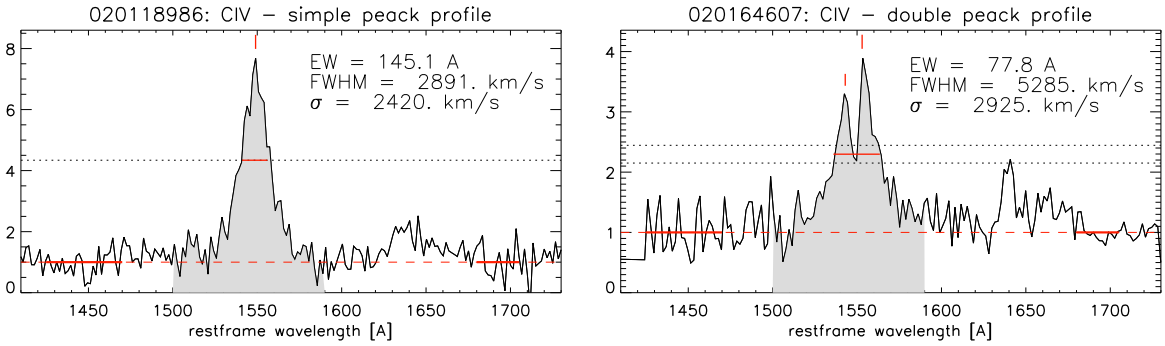

observes that $\tau \propto \Delta V^{-2}$ as expected from the virial equation; (2) The $M_{BH} - \sigma_*$ relation seen in quiescent galaxies (Ferrarese & Merritt 2000; Gebhardt et al. 2000) is consistent with the one obtained for AGN with available bulge velocity dispersion σ_* measurements.

A strong restriction of this method is its observational load, limiting thereby the number of AGN for which this study is performed. However, reverberation mapping put in evidence a simple relationship between the continuum luminosity L of the AGN and the size of the BLR. For a given emission line $R \propto L^{\gamma}$, giving thereby the possibility to estimate an AGN black hole (BH) mass from any flux calibrated spectrum. The exponent factor, γ, is ~ 0.5 and depends on the band where the luminosity is measured and, possibly, the emission line considered.

The relations obtained thence between M_{BH}, L and ΔV, i.e. $M_{BH} \propto L^{\gamma}\Delta V^2$, are called mass scaling relation and are the one we are using in this work.

Mass scaling relations

In this work we use the relationships calibrated in McLure & Dunlop (2004) for Mg II and Vestergaard & Peterson (2006) for C IV.

$$\text{Mg II:}\ \log\frac{M_{BH}}{M\odot} = \log\left(\text{FWHM}_{1000}^2(\lambda \text{L}_{\lambda\,44})^{0.62}\right) + 6.51, \text{ with } \lambda\text{=3000 Å} \quad (3.5)$$

$$\text{C IV:}\ \log\frac{M_{BH}}{M\odot} = \log\left(\sigma_{1000}^2(\lambda \text{L}_{\lambda\,44})^{0.53}\right) + 6.73, \text{ with } \lambda\text{=1350 Å} \quad (3.6)$$

where FWHM_{1000} and σ_{1000} are FWHM and velocity dispersion expressed in units of 1000 km s^{-1}while $\text{L}_{\lambda\,44}$ is the luminosity per Å in units for 10^{44} erg.s^{-1} at 1350 Å.

Line width measurements

Full-width-half-maximum and line dispersion σ_l were measured following Peterson et al. (2004). In the following we designate the emission line profile $P(\lambda)$ as been the flux

per unit wavelength above the continuum level (the normalisation of emission-line profiles is described Section 3.7.1).

FWHM: In the case of single-peaked line we identify the line peak flux P_{max}, and search for the wavelength limits, at short and long wavelength, where the line profile $P(\lambda)$ cross the half of P_{max} value. In the case of double-peaked profile we apply this method to both peaks of the profile and the FWHM is taken to be the separation between the mean value of the two short wavelength limits and the mean value of the two long wavelength limits, this procedure is illustrated Figure 3.24.

Line dispersion: It is the second moment of the line profile,

$$\sigma_l^2 = < \lambda^2 > - < \lambda >^2$$

or:

$$\sigma_l^2 = \frac{\int \lambda^2 P(\lambda) d\lambda}{\int P(\lambda) d\lambda} - \left(\frac{\int \lambda P(\lambda) d\lambda}{\int P(\lambda) d\lambda} \right)^2$$

Resolution correction:
Correction for the finite resolution of our spectrograph is done assuming that:

$$\Delta\lambda_{obs}^2 = \Delta\lambda_{true}^2 + \Delta\lambda_{res}^2$$

The instrumental resolution can vary from one spectra to the other due to the variable observational conditions (in particular, the seeing). However, this resolution correction is already small for most of our emission lines and we can adopt a mean resolution for all our spectra. We therefore take the value adopted by the VVDS spectrophotometric working group, based on intense narrow emission lines [4] (mostly [O III]λ5007). They find $\Delta\sigma_{res} = 350 \mathrm{km\,s^{-1}}$.

The 8 C IV emission-lines profile affected by absorption are excluded for line width measurements.

UV continuum luminosities

To compute monochromatic continuum luminosities we flux-calibrate our spectra with VVDS I-band photometry. This is done by applying a normalisation factor N which ensure that the light integrated in our spectra convolved with our I-band response filter equals the measured I band photometric flux. Monochromatic luminosities are directly measured from the re-calibrated spectra.

Error on black hole mass estimate

Analysis suggest that the intrinsic error on black hole mass estimate obtained from reverberation mapping is typically a factor close to three Onken et al. (2004). This lead, for black hole mass estimate derived from scaling relations to an accuracy

[4] Remark: The [O II] emission line is an unresolved doublet (with $\lambda\lambda$3726,3729) and therefore is not used for this purpose.

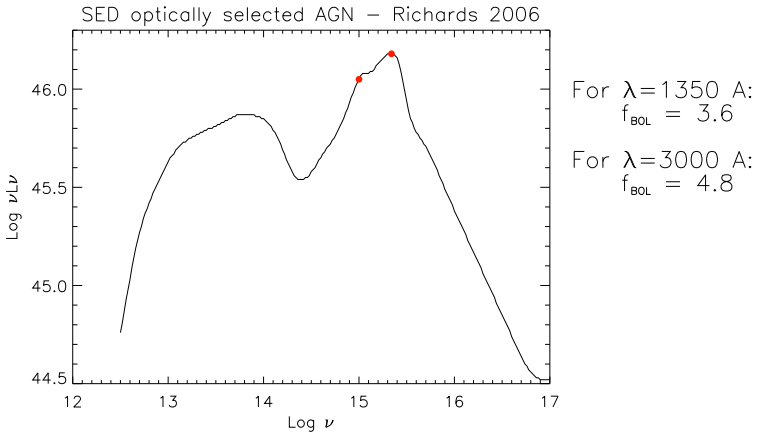

Figure 3.25: mean SED of "Type 1 quasars" (Richards et al. 2006a) considered here to compute our bolometric correction factor .

limited to a factor of order 4 Vestergaard & Peterson (2006). In this preliminary analysis, we will neglect the errors induced by our linewidth and luminosity measurements in front of this intrinsic error factor.

3.9.2 Accretion rates and Eddington ratios

Bolometric correction

We derive the bolometric luminosity of our objects from the monochromatic luminosities previously derived, multiplied by a factor, the bolometric correction factor f_{bol} based on the mean SED of optical AGN given by Richards et al. (2006a) for "Type 1 quasars". Type 1 AGN radiate most of their light at UV-wavelengths, leading thus to small correction factors: we find $f_{bol}(3000\text{Å}) = 4.8$ and $f_{bol}(1350\text{Å}) = 3.6$ (the correction factors obtained considering the Elvis et al. (1994) radio-quiet quasar template, previously used in the litterature, are slightly larger with $f_{bol}(3000\text{Å}) = 5.3$, $f_{bol}(1350\text{Å}) = 4.3$). There is observational evidence for an increase of $f_{bol}(UV)$ towards fainter luminosities (e.g. Wilkes et al. 1994; Green et al. 1995; Vignali et al. 2003; Strateva et al. 2005; Steffen et al. 2006). Moreover, for a given class of AGN and at a given luminosity, their is a significant dispersion of observed SED (Richards et al. 2006a). Marconi et al. (2004) argue as well that the *observed* bolometric luminosity estimated this way contains, in addition to the *intrinsic* bolometric luminosity, light radiated in the UV along other lines of sight and re-emitted isotropically in the infra-red (causing the "IR-bump"). To encompass all these effects we adopt a relative incertitude of $\Delta f_{bol}/f_{bol} = 30$ %.

Accretion rates

The accretion rate $\dot{m}$ is derived from the bolometric luminosity, L_{bol} assuming the efficiency ϵ of conversion of the gravitational energy to radiation:

$$L_{bol} = \epsilon \dot{m} c^2 \tag{3.7}$$

Theoretical expectations for ϵ vary from $\sim$ 5 percents for non-rotating BH to $\sim$ 40% in the case of spinning BH (Shapiro & Teukolsky 1983). We consider here the standard value adopted in the literature of $\epsilon = 0.1$.

Eddington ratios

The BH mass is univocally tied to its Eddington luminosity. Under the assumption of a spherical symmetry:

$$L_{EDD} = \frac{4\pi c \mathcal{G} m_p}{\sigma_e} M_{BH} \tag{3.8}$$

$$\log L_{EDD,44} \sim \log \frac{M_{BH}}{M\odot} - 5.90 \tag{3.9}$$

Where $L_{EDD,44}$ is the luminosity in units of 10^{44} erg.s^{-1}. Previous studies suggest that, indeed, the Eddington luminosity is a meaningful physical limit for broad line AGN (e.g: McLure & Dunlop (2004)). It is therefore interesting to study our AGN in terms of their Eddington ratio defined as $f_{EDD} = L_{bol}/L_{EDD}$.

3.9.3 First results and futur work

The BH mass estimated from equations 3.5 and 3.6 for the VVDS AGN sample are indicated Tables D.1 and D.4. In the following, we restricted our analysis to objects with a S/N larger than 7.

For this sample of AGN , BH masses are ranging from 2×10^7 to 6×10^8 M$\odot$ with a mean value close to 10^8 M$\odot$.

Figure 3.26 shows the distribution of BH masses and Eddington rates as a function of bolometric luminosities. As expected, BH masses and Eddington rates are correlated to the AGN bolometric luminosity: the most luminous quasars tend to be powered by the largest BH accreting at relatively high Eddington rates. However we observe that no black hole with mass estimate lower than 2×10^7 M$\odot$ is present in our sample although they could have been detected given the luminosity range we are exploring. To check whether this effect could be introduced by our limited spectral resolution, we add Figure 3.26 the lines drawn by emission-lines of constant widths : FWHM = 1000; 1500; and 2000 km s^{-1}. It is possible in the VVDS to resolve emission lines for which FWHM $\gtrsim$ 800km.s^{-1} and we expect that our AGN sample contain the objects with emission-lines for which FWHM $\gtrsim$ 1000km.s^{-1}. We should therefore be able to select AGN with BH masses lower than 10^7 M$\odot$. If we compare our result those of Kollmeier et al. (2006) (see Figure 3.28, presenting a copy their Figure 6), we can see that our results are qualitatively very different: in this sample

the M_{BH}–L_{BOL} distribution follow a diagonal ridge fairly well enclosed and parallel to the two lines materialising Eddington rates of 0.1 and 1. One conclusion of this work is a lack of AGN for which $f_{EDD} \lesssim 0.1$, which contradicts our observations. The main difference with our sample is that we are sampling a fainter population of AGN. Our result suggest therefore that this observed "ridge distribution" deviate for $L_{BOL} \lesssim 45$ erg.s^{-1}.

Figure 3.29 shows our derived distribution of black hole masses and Eddinton ratio versus redshift, compared to the brighter SDSS AGN sample. The question motivating this work was : what sort of BH is standing behind the low luminosity AGN seen in excess at lower redshift ? This first analysis suggest that the bulk of low luminosity AGN seen in our sample is caused by intermediate mass galactic black holes ($\sim 10^8$) radiating at moderate Eddington rates ($f_{EDD} \lesssim 10\%$).

However, we still need to perform sereval test to confort our results:

- Our current estimate of Mg II emission-line width is most likely biased by the surrounding iron emission. We still need to implement a procedure to substract the iron emission by a simultaneous fitting of our continuum and a iron emission-line template (Vestergaard & Wilkes 2001);
- Making use of our FORS spectra, it is possible for ~ 20 AGN to estimate black hole masses from both Mg II and C IV emission lines;
- We still need to quantify the observed dispertion and possible systematic effects introduced by the estimate of the bolometric luminosities from the UV-continuum in this work (at 3000Å and 1300 Å), and from the optical continuum at 5100 Åused in Kollmeier et al. (2006).

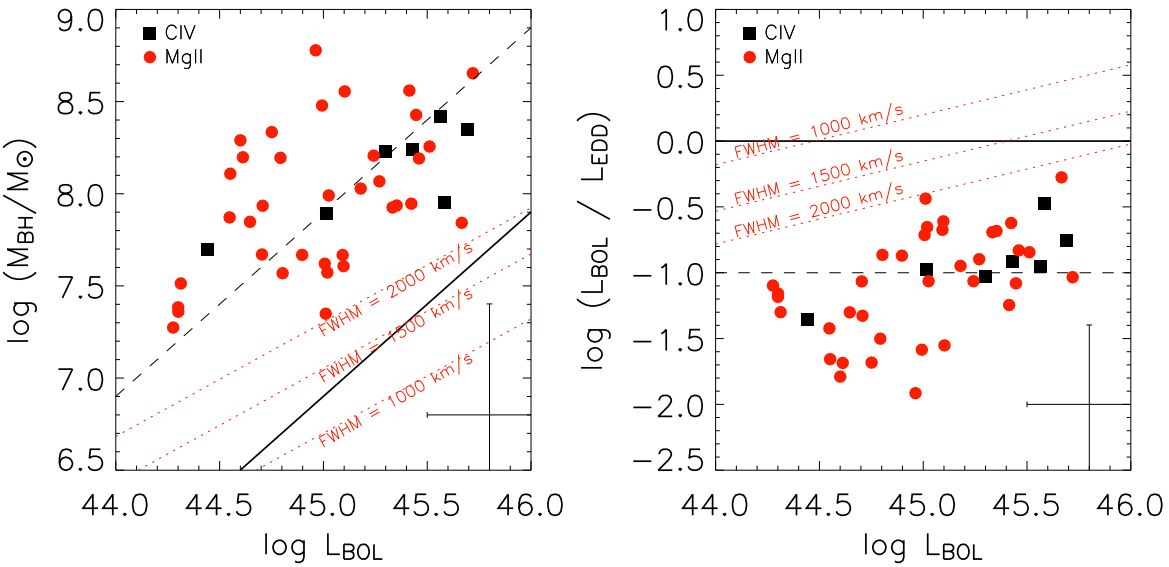

Figure 3.26: BH mass (left) and Eddington ratio (right) as a function of AGN bolometric luminosity. The solid line and the dashed line correspond respectively to $f_{EDD} = 1$ and $f_{EDD} = 0.1$. Point symbols indicate the emission line used for the mass measurement: red dots corresponds to Mg II while black squares correspond to C IV. The red dotted lines correspond to the track followed for different emission line width values in the case of the MgII emission line. The error bar reported in the lower left corner correspond to the *intrinsic* error of the method employed to estimate the black hole mass and the bolometric luminosity of an individual AGN.

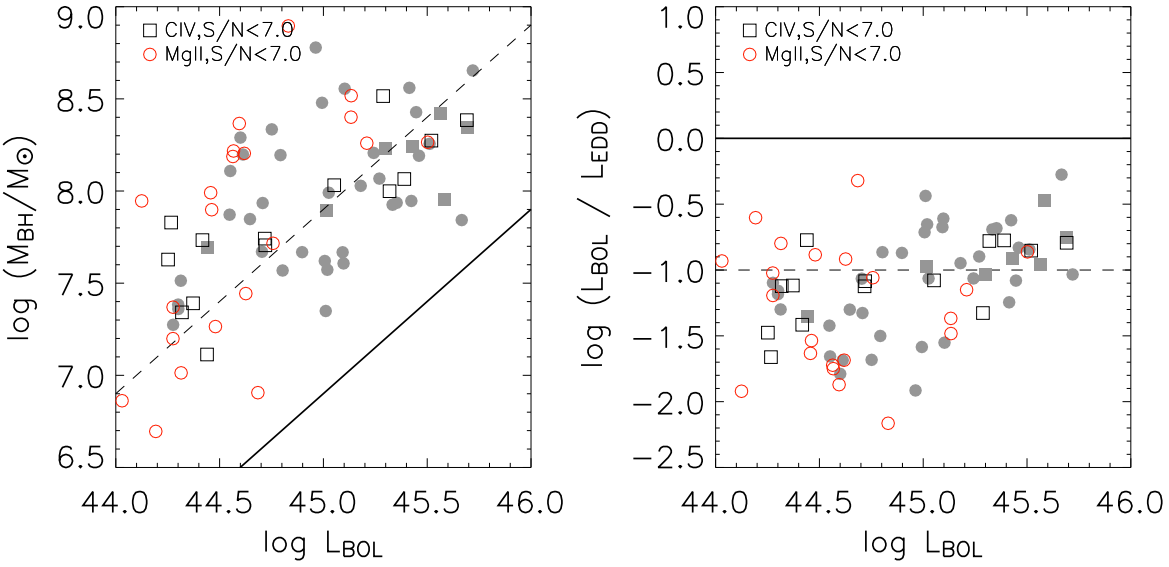

Figure 3.27: The same as figure 3.26 showing this time objects with a S/N inferior to 7 which we excluded from our analysis. Non-excluded values are reported in grey. Symbols have not changed but are now open.

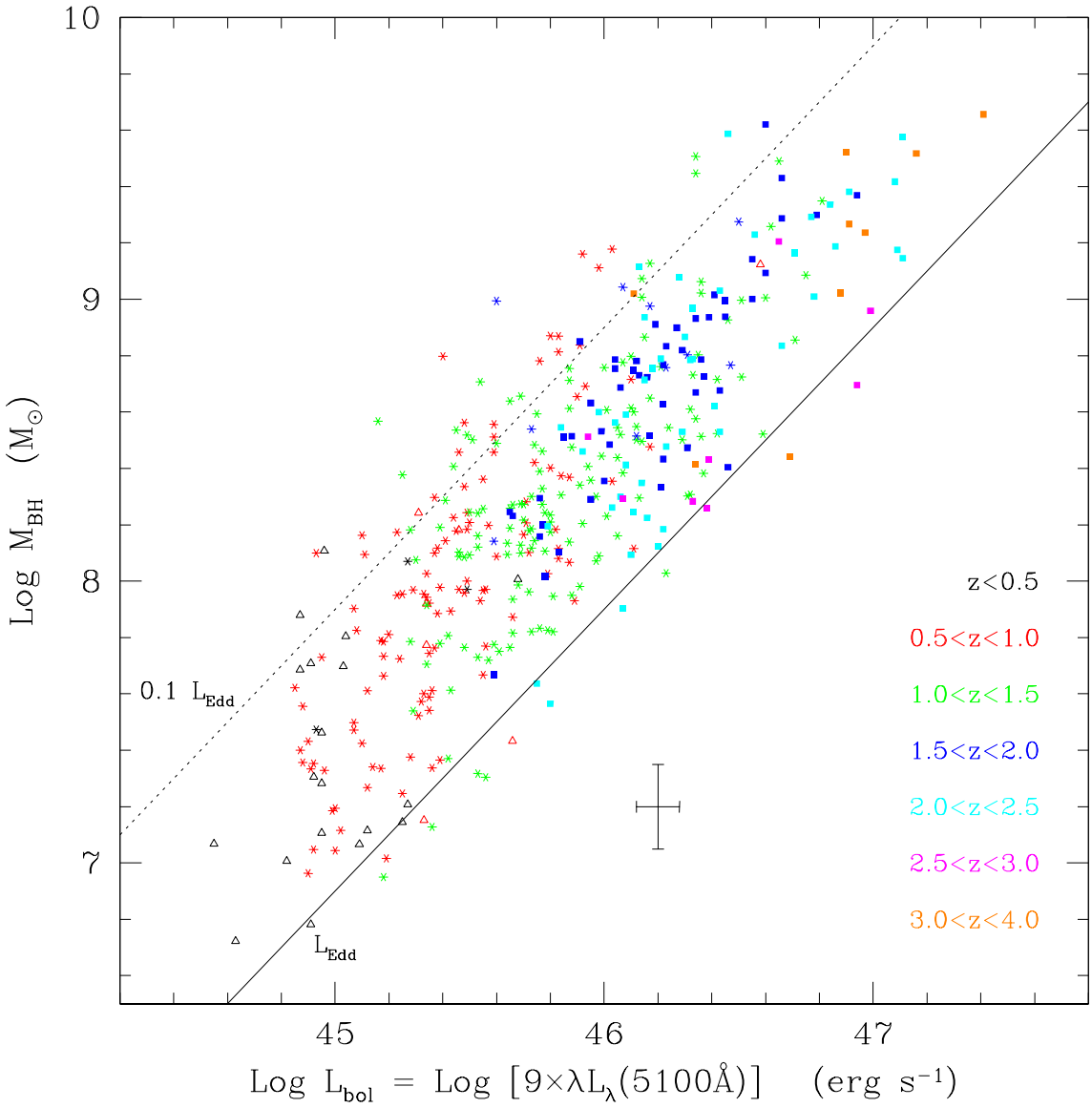

Figure 3.28: Estimated BH masses as a function of AGN bolometric luminosity in the AGES survey (Kollmeier et al. 2006,Figure 6)

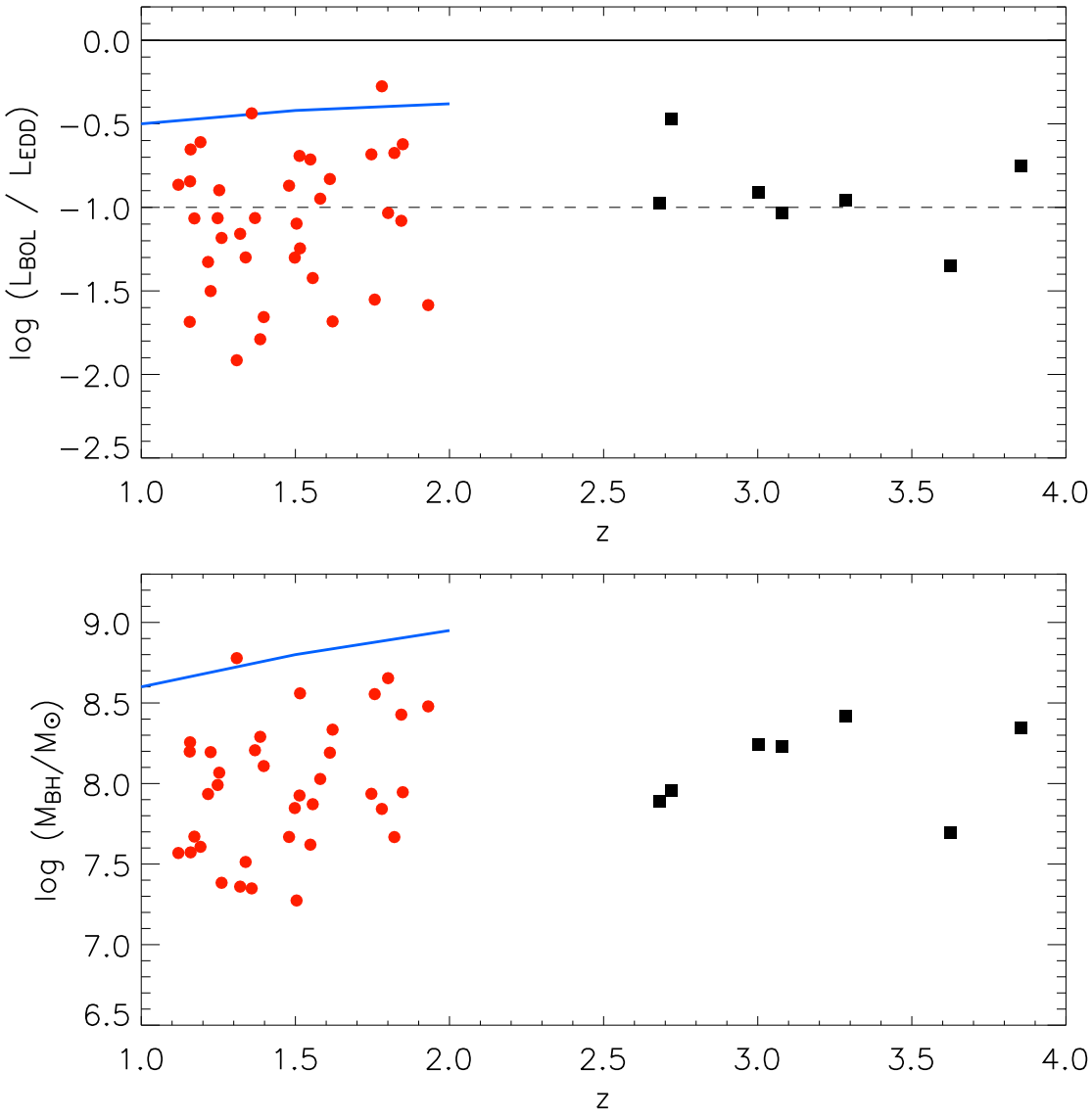

Figure 3.29: Eddington rate and black hole mass as a function of redshift. The blue lines indicates the mean Eddington rate and black hole mass evolution observed in the SDSS sample (McLure & Dunlop 2004,Figure 1 and 2). The solid line and the dashed line correspond respectively to $f_{EDD} = 1$ and $f_{EDD} = 0.1$. Point symbols indicate the emission line used for the mass measurement: red dots corresponds to Mg II while black squares correspond to C IV.

L'échantillon d'AGN

Ces AGN ont été purement sélectionnés dans le catalogue général du VVDS sur la base de la présence dans leur spectre de raies d'émission larges. Le *wide survey* contient 56 AGN alors que le *deep survey* en contient 74. Certains des AGN sélectionnés n'ont qu'une raie présente dans leur spectre et pour une fraction de ces objets (environ 30% du catalogue complet) il n'est pas possible d'identifier de manière univoque cette raie d'émission et donc le redshift de ces objets. Pour remédier à ce problème nous avons commencé une campagne de ré-observation avec le spectrographe FORS1 au VLT, étendant ainsi la couverture spectrale de ces objets vers le bleu jusqu'à 3800 Å et permettant la détection d'une seconde raie d'émission. Suite aux observations effectuées en Mars 2004 puis en Novembre 2005, la fraction de ces AGN avec un redshift ambigü est maintenant réduite à 10%.

D'autre part nous avons déterminé nôtre fonction de sélection et montrons que le VVDS permet de détecter effectivement des AGN sur toute notre couverture en magnitude et en redshift à l'exception cependant du domaine où z$\sim$1.

La densité d'AGN que nous mesurons sur le ciel à notre magnitude limite $I_{AB} = 24$ est d'environ 470 AGN par degré carré. Nous observons un fléchissement de la relation comptage-magnitude ($log\mathcal{N} - I_{AB}$). Ceci est clairement traduit dans la relation différentielle comptage-magnitude par une inflexion à la magnitude $I_{AB} \sim 21.5$. Le seul échantillon sélectionné en optique d'AGN de type 1 avec une magnitude limite similaire à la notre est celui obtenu à partir du COMBO-17 (Wolf et al. 2003). Il contient 192 objets avec $z > 1.2$ identifiés photométriquement. En considérant uniquement nos objets avec $z > 1.2$, on obtient une densité de surface en bon accord avec celle du COMBO-17.

Nos AGN sont distribués entre le redshift 0.15 et 5. La fraction d'objets avec $z > 3$ est de $\sim$ 16 %. De façon relativement surprenante, nous observons le même redshift moyen ($z \sim 1.8$) dans le *wide survey* et dans le *deep survey*. Ceci démontre qu'en allant vers de plus faibles magnitudes au lieu d'observer des AGN plus éloignés, nous dévoilons une population d'AGN intrinséquement moins lumineuse. Effectivement $\sim$35% de nos objets ont une magnitude absolue $M_B > -23$ correspondant à la catégorie des galaxie Seyfert-1.

En comparant la distribution de nos AGN dans le plan de couleurs $u - g$, $g - r$ avec le catalogue photométrique complet des objets de profil stellaire du VVDS, nous montrons que 35% des AGN de notre échantillon avec $z < 2.3$ et $I_{AB} < 22.5$ n'auraient pas pu être sélectionnés à partir des critères morphologiques et d'excès ultra-violet usuellement utilisés. D'autre part nous observons que 42% de nos objets ayant un redshift $z < 1.6$ pour une limite $I_{AB} < 22.5$ sont spatialement résolus en imagerie I, ce qui suggère une contamination lumineuse de leurs galaxies hôtes.

Un spectre composite est généré en co-additionnant les spectres individuels de nos objets ramenés dans leur repère propre. Le continuum du spectre composite du VVDS s'avère être plus rouge que celui du spectre composite du SDSS (Vanden Berk et al. 2001), et cela est encore plus marqué pour les longueurs d'ondes supérieures à $\sim$3500 Å . Nous pensons que ce résultat traduit (au moins partiellement) la contamination

de nos AGN par leurs galaxies hôtes.

Nous nous interéssons aux propriétés des raies d'émission de nos objets et observons que les AGN de plus faible luminosité ont, en moyenne, des raies de C IV plus intenses. Cette corrélation, associée à une forte dispersion, est connue sous le nom d'effet Baldwin (Baldwin 1977) et est également visible dans le cas de Mg II si l'on compare notre spectre composite à celui du SDSS.

Finalement, nous présentons les résultats préliminaires concernant la fonction de luminosité (LF) des AGN pour $z > 1$. Nous observons qu'à bas redshift ($z < 1.5$) la pente exponentielle de la LF vers les faibles luminosités est relativement forte, comparées aux précèdentes études portant sur des échantillons optiques d'AGN. Cette pente s'applatit pour ($z > 1.5$), ce qui suggère qu'à bas redshift, il y ait plus d'AGN de faible luminosité qu'à plus grand redshift. Cette observation corrobore le scénario de croissance anti-hièrarchique de trous-noirs galactiques suggéré par les échantillons d'AGN sélectionnés en rayons-X.

Conclusion

In research, every day brings a new set elements that one is eagerly comparing to the frame already acquired, trying to set some milestones. The perspective of an achieved work is somehow illusory and interrupting ones analysis to conclude is not something easy to do!

In this work we have explored various properties of a spectroscopic sample of 130 broad line AGN which presents two major interests: (1)a selection function free of pre-selection biases, which enables us to census the population of optical broad line AGN from redshift 0 to 5 in a coherent way; (2) a very faint limiting magnitude (respectively $I_{AB} = 22.5$ and $I_{AB} = 24$ for the *wide* and *deep* sample) that was previously reached for a catalog of this size only by photometric studies.

The different results found in this thesis can be listed as following:

- After a comprehensive analysis of our selection function, we could measure the surface density of BLAGN in the sky: there is 472 ± 48 BLAGN per deg^2 with a magnitude $I_{AB} \leq 24$. A turn-over is observed in the differential number counts at $I_{AB} \sim 21.5$;

- We observed that by pushing the magnitude limit from $I_{AB} = 22.5$ to $I_{AB} = 24$, from the *wide* to the *deep* field, the result is not to increase the mean redshift of the sample, observed to be 1.8. The deep sample is therefore unveiling the faint end of the AGN luminosity function, at all redshifts.

- 35% of the VVDS BLAGN have magnitudes fainter than $M_B = -23$, offering the opportunity to study a population of AGN entering the galaxy luminosity function. In fact, we can establish that the host galaxy light of a significant number of AGN is directly detected since over 20% of our AGN with $I_{AB} < 22.5$ are morphologically classified as extended. Most of these extended BLAGN are below the redshift $z = 1.6$, and in this redshift range 42% of VVDS BLAGN are extended. This opportunity is clearly favored by the absence of pre-selection criteria present in our sample: By comparing the $u^* - g'$, $g' - r'$ color distribution of our AGN population with $z < 2.3$ and $I_{AB} < 22.5$

to the complete VVDS photometric catalog of stellar-like objects, we find that $\sim 35\%$ of the AGN present in our sample would be missed by the usual UV excess and morphological criteria used for the pre-selection of optical QSO candidates in this redshift range.

- This last point naturally brought us to interpret two further results as being a consequence of the contamination of our AGN observations by their host galaxy stellar light continua: we observed first, that the VVDS BLAGN have redder colors at the faint end of the luminosity function and second, a comparison of the VVDS and SDSS composite QSO spectra shows that the VVDS continuum is significantly redder than the SDSS one, especially at long wavelengths. Of course, some other effect could be coming into play, for example, we cannot exclude the possibility that the intrinsic spectrum of BLAGN is getting redder towards fainter luminosity, or that we are observing some dust reddened objects, but there is no need to invoke these effects to explain our observations.

- We observe an extension of the anti-correlation between luminosity and equivalent-width of high-ionization emission-lines to the fainter luminosities probed by our sample for a given redshift. This effect is commonly referred to as the Baldwin effect. In our case, we observe evidence of the Baldwin effect for the C IV and Mg II emission lines, if we compare the emission lines property of the SDSS composite spectra to our own composite spectra. When restricting ourselves to our own sample, we can establish this effect taking place in the case of the C IV emission line. The EW observed for the C IV, C III] and Mg II emission lines are otherwise consistent with the EW quoted in the recent literature for objects of the same luminosities but observed at lower redshifts.

- In the context of the study of the VVDS luminosity function and its evolution, our BLAGN sample has two specific properties: First, it is free of biases in the redshift range $2 < z < 3$, which will help to shed light on the change of QSO evolution occurring in this redshift range; Second, since no bias against low luminosity AGN is present in this sample, this will make easier the comparison of the evolution of low and high luminosity AGN, allowing a better understanding of the QSO-Seyfert connection. The first results on the binned luminosity function suggest a relatively steep faint end at low redshift ($1 < z < 1.5$), and in contrast a milder faint end at higher redshifts ($z > 1.5$) (Bongiorno et al. 2006, in preparation)

- Eventually we estimate the virial black-hole masses of our sample of AGN, using the scaling-relations calibrated from the reverberation mapping studies. Our preliminary results seem to contradict the current statement that AGN with low Eddington rate are rare. At the contrary, the bulk of our faint AGN are powered by black holes with moderate masses $M_{BH} \sim 10^8 \mathrm{M}\odot$ accreting at Eddintong rate $\lesssim$10%.

Currently the statistics of this sample is improved by a factor $\sim$ 2 with 230 BLAGN identified in the database and other important results are expected from this same sample of objects. In particular, from the parametric study of the luminosity function and the contribution of low luminosity AGN to the metagalactic UV-flux density.

Other deep AGN surveys are coming. One of them is the COSMOS survey which will collect $\sim$ 2000 X-ray selected AGN with spectroscopic confirmation and high resolution imaging, with the aim to study the black holes and their host galaxies co-evolution.

Conclusion (français)

Au cours de ce travail de thèse nous avons exploré plusieurs propriétés d'un échantillon de 130 AGN à raies d' émissions larges qui présente deux intérêts majeurs : (1) une fonction de sélection libre de tout biais de pré-sélection qui permet d' étudier de façon cohérente la population d'AGN de redshift 0 à 5 ; (2) une limite en magnitude très faible (respectivement $I_{AB} = 22.5$ et $I_{AB} = 24$ pour l' échantillon *wide* et *deep*) qui n'avait été jusqu' à présent atteinte pour un catalogue de cet taille uniquement par des études photométriques.

Les différents résultats obtenus au cours de cette thèse peuvent être listés de la façon suivante :

- La densité projetée d'AGN à raies d' émission larges sur le ciel est de 472 ± 48 objets par degré carré et la relation différentielle comptage-magnitude s'infléchit à $I_{AB} = 21.5$.
- En sélectionnant des AGN à des magnitudes plus faibles (en passant d'une limite en magnitude de $I_{AB} = 22.5$ à $I_{AB} = 24$), on ne sélectionne pas des AGN qui sont situés en moyenne à de plus forts redshifts mais des AGN intrinsèquement plus faibles.
- 35% des AGN du VVDS ont des magnitudes plus faible que $M_B = -23$, et offrent donc l'opportunité d' étudier une population d'AGN qui pénètre la fonction de luminosité des galaxies. Nous observons par ailleurs plusieurs propriétés pour nos objets que nous attribuons à la contamination par leur galaxie hôte : un AGN sur cinq semble spatialement résolu et pour un redshift inférieur à 1.6 cette fraction correspond à 40% ; les AGN les plus faibles sont également plus rouge et le spectre composite des AGN du VVDS est également plus rouge que celui du SDSS (Vanden Berk et al. 2001).
- Nous observons une anti-corrélation entre la luminosité et la largeur équivalente des raies d émission d' ionisation élevée. Cet effet est généralement appelé "effet Baldwin" (Baldwin 1977). Dans notre cas, nous pouvons mettre en évidence l'effet Baldwin pour les raies d' émission de C IV et de Mg II, si nous comparons les propriétés des raies d' émission du spectre composite du SDSS à celles de notre propre spectre composite. En se limitant à notre propre échantillon, nous pouvons observer cet effet pour la raie d' émission C IV. Les largeurs de raies équivalentes observées pour les raies d émissions C IV, C III] et Mg II sont en accords avec celles mentionées dans la littérature récente pour des objets de même luminosité mais observés à des redshifts inférieurs.
- Notre échantillon à deux avantages majeurs pour explorer la fonction de luminosité des AGN faiblement brillants. Premièrement, il est très peu biaisé dans l intervalle de redshift de 2 à 3 marqué dans les échantillons plus brillants par une inversion de l évolution des AGN de type 1. Dautre part, il couvre un intervalle de luminosité qui permet de caractériser la connexion QSO-Seyfert. On peut par contre prévoir un biais dans notre fonction de luminosité pour les objets de redshift inférieur à 1,5 où la contamination lumineuse des galaxies hôtes de nos AGN semble être appréciable. Des tests sont en cours pour

voir comment dissocier au mieux ces deux composantes. Les résultats de ces travaux en cours seront bientôt présentés par Bongiorno et al. (2006).

– Finalement nous nous sommes intéressés à la nature des trous-noirs qui sont à l'origine de nos AGN. S'agit-il de petits trous noirs galactiques qui accrètent à un taux proche de leur limite d'Eddington ? Ou bien, au contraire, de trous noirs galactiques de grande masse accrétant faiblement. Les résultats présentés ici sont encore préliminaires et doivent être confortés. Ces premiers résultats suggèrent qu'il existe un nombre non-négligeable d'AGN accrétant à des taux d'Eddington faibles et que nos objets correspondent en moyenne à des trous noirs de masses intermèdiaires ($\sim 10^8 M\odot$) accrétant à des taux d'Eddington modeste ($\lesssim 10\%$).

Actuellement, les statistiques de cet échantillon sont améliorées par un facteur d' environ 2 avec 230 BLAGN identifiés dans la base de données et d'autres résultats importants sont attendus de ce même échantillon d'objets. En particulier, l' étude paramétrique de la fonction de luminosité et la contribution des AGN de faible luminosité devraient apporter des informations sur la densité du flux UV métagalactique.

D'autres projets vont bientôt permettre de mieux suivre l'histoire de l' accrétion sur les trous noirs super massifs et ainsi de mieux comprendre le lien entre l' évolution des galaxies et la croissance de leurs trous noirs centraux. L'un de ces projets est le sondage COSMOS qui collectera près de 2000 AGN sélectionnés en rayonnement X.

Bibliography

Abazajian, K., Adelman-McCarthy, J. K., Agüeros, M. A., et al. 2003, AJ, 126, 2081

Alexander, D. M., Bauer, F. E., Brandt, W. N., et al. 2003, AJ, 126, 539

Antonucci, R. 1993, ARA&A, 31, 473

Antonucci, R. R. J. 1982, Nature, 299, 605

Antonucci, R. R. J. & Miller, J. S. 1985, ApJ, 297, 621

Arnouts, S., Schiminovich, D., Ilbert, O., et al. 2005, ApJ, 619, L43

Arnouts, S., Vandame, B., Benoist, C., et al. 2001, A&A, 379, 740

Avni, Y. & Bahcall, J. N. 1980, ApJ, 235, 694A

Baganoff, F. K., Bautz, M. W., Brandt, W. N., et al. 2001, Nature, 413, 45

Baldwin, J. A. 1977, ApJ, 214, 679

Baldwin, J. A., Phillips, M. M., & Terlevich, R. 1981, PASP, 93, 5

Barger, A. J., Cowie, L. L., Capak, P., et al. 2003, AJ, 126, 632

Barger, A. J., Cowie, L. L., Mushotzky, R. F., & Richards, E. A. 2001, AJ, 121, 662

Barger, A. J., Cowie, L. L., Mushotzky, R. F., et al. 2005, AJ, 129, 578

Becker, R. H., White, R. L., Gregg, M. D., et al. 2001, ApJS, 135, 227

Becker, R. H., White, R. L., & Helfand, D. J. 1995, ApJ, 450, 559

Blandford, R. D. & McKee, C. F. 1982, ApJ, 255, 419

Bondi, M., Ciliegi, P., Zamorani, G., et al. 2003, A&A, 403, 857

Bongiorno et al. 2006, in preparation

Boroson, T. A. & Green, R. F. 1992, ApJS, 80, 109

Bottini, D., Garilli, B., Maccagni, D., et al. 2005, PASP, 117, 996

Boyle, B. J., Shanks, T., Croom, S. M., et al. 2000, MNRAS, 317, 1014

Brunzendorf, J. & Meusinger, H. 2002, A&A, 390, 879

Bruzual, G. & Charlot, S. 2003, MNRAS, 344, 1000

Chapman, S. C., Blain, A. W., Ivison, R. J., & Smail, I. R. 2003, Nature, 422, 695

Cimatti, A., Zamorani, G., & Marano, B. 1993, MNRAS, 263, 236

Cirasuolo, M., Celotti, A., Magliocchetti, M., & Danese, L. 2003, MNRAS, 346, 447

Colless, M., Dalton, G., Maddox, S., et al. 2001, MNRAS, 328, 1039

Comastri, A., Mignoli, M., Ciliegi, P., et al. 2002, ApJ, 571, 771

Condon, J. J., Cotton, W. D., Greisen, E. W., et al. 1998, AJ, 115, 1693

Contini et al. 2006, in preparation

Cristiani, S., Trentini, S., La Franca, F., et al. 1996, A&A, 306, 395

Croom, S. M., Rhook, K., Corbett, E. A., et al. 2002, MNRAS, 337, 275

Croom, S. M., Smith, R. J., Boyle, B. J., et al. 2004, MNRAS, 349, 1397

Davis, M., Faber, S. M., Newman, J., et al. 2003, in Discoveries and Research Prospects from 6- to 10-Meter-Class Telescopes II. Edited by Guhathakurta, Puragra. Proceedings of the SPIE, Volume 4834, pp. 161-172 (2003)., ed. P. Guhathakurta, 161–172

Dietrich, M., Hamann, F., Shields, J. C., et al. 2002, ApJ, 581, 912

Djorgovski, S. G., Mahabal, A. A., Brunner, R. J., et al. 2001, in ASP Conf. Ser. 225: Virtual Observatories of the Future, ed. R. J. Brunner, S. G. Djorgovski, & A. S. Szalay, 52–+

Edelson, R. A., Alexander, T., Crenshaw, D. M., et al. 1996, ApJ, 470, 364

Elitzur, M. 2005, ArXiv Astrophysics e-prints

Elvis, M., Wilkes, B. J., McDowell, J. C., et al. 1994, ApJS, 95, 1

Fan, X., Strauss, M. A., Richards, G. T., et al. 2006, AJ, 131, 1203

Fath, E. A. 1908, Lick Observatory Bulletin, 5, 71

Ferrarese, L. & Merritt, D. 2000, ApJ, 539, L9

Fiore, F., La Franca, F., Giommi, P., et al. 1999, MNRAS, 306, L55

Fiore, F., La Franca, F., Vignali, C., et al. 2000, New Astronomy, 5, 143

Floyd, D. J. E., Kukula, M. J., Dunlop, J. S., et al. 2004, MNRAS, 355, 196

Francis, P. J., Hewett, P. C., Foltz, C. B., et al. 1991, ApJ, 373, 465

Garilli et al. 2006, in preparation

Gavignaud, I., Bongiorno, A., Paltani, S., et al. 2006, A&A, 457, 79

Gebhardt, K., Bender, R., Bower, G., et al. 2000, ApJ, 539, L13

Gehrels, N. 1986, ApJ, 303, 336

Giacconi, R., Gursky, H., Paolini, F. R., & Rossi, B. B. 1962, Physical Review Letters, 9, 439

Giacconi, R., Zirm, A., Wang, J., et al. 2002, ApJS, 139, 369

Gilli, R., Salvati, M., & Hasinger, G. 2001, A&A, 366, 407

Granato, G. L., De Zotti, G., Silva, L., Bressan, A., & Danese, L. 2004, ApJ, 600, 580

Green, P. J., Schartel, N., Anderson, S. F., et al. 1995, ApJ, 450, 51

Hasinger, G., Miyaji, T., & Schmidt, M. 2005, A&A, 441, 417

Helfand, D. J., Stone, R. P. S., Willman, B., et al. 2001, AJ, 121, 1872

Hewett, P. C., Foltz, C. B., & Chaffee, F. H. 1995, AJ, 109, 1498

Ho, L. C., Filippenko, A. V., & Sargent, W. L. W. 1994, in IAU Symp. 159: Multi-Wavelength Continuum Emission of AGN, ed. T. Courvoisier & A. Blecha, 275–278

Hornschemeier, A. E., Brandt, W. N., Garmire, G. P., et al. 2001, ApJ, 554, 742

Ilbert, O., Tresse, L., Zucca, E., et al. 2005, A&A, 439, 863

Iovino, A., McCracken, H. J., Garilli, B., et al. 2005, A&A, 442, 423

Ivezić, Ž., Menou, K., Knapp, G. R., et al. 2002, AJ, 124, 2364

Jackson, C. A., Wall, J. V., Shaver, P. A., et al. 2002, A&A, 386, 97

Jaffe, W., Meisenheimer, K., Röttgering, H. J. A., et al. 2004, Nature, 429, 47

Jiang, L., Fan, X., Cool, R. J., et al. 2006, AJ, 131, 2788

Jones, B. J. T. & Jones, J. E. 1980, MNRAS, 193, 537

Kawaguchi, T., Mineshige, S., Umemura, M., & Turner, E. L. 1998, ApJ, 504, 671

Kellermann, K. I., Sramek, R., Schmidt, M., Shaffer, D. B., & Green, R. 1989, AJ, 98, 1195

Kellermann, K. I., Sramek, R. A., Schmidt, M., Green, R. F., & Shaffer, D. B. 1994, AJ, 108, 1163

Kewley, L. J., Groves, B., Kauffmann, G., & Heckman, T. 2006, ArXiv Astrophysics e-prints

Khachikian, E. Y. & Weedman, D. W. 1974, ApJ, 192, 581

Kinney, A. L., Rivolo, A. R., & Koratkar, A. P. 1990, ApJ, 357, 338

Kollmeier, J. A., Onken, C. A., Kochanek, C. S., et al. 2006, ApJ, 648, 128

Krolik, J. H., Horne, K., Kallman, T. R., et al. 1991, ApJ, 371, 541

Kron, R. G. 1980, ApJS, 43, 305

La Franca, F., Fiore, F., Vignali, C., et al. 2002, ApJ, 570, 100

Lacy, M., Storrie-Lombardi, L. J., Sajina, A., et al. 2004, ApJS, 154, 166

Lamareille, F., Contini, T., Le Borgne, J.-F., et al. 2006, A&A, 448, 893

Le Fèvre, O., Mellier, Y., McCracken, H. J., et al. 2004, A&A, 417, 839

Le Fèvre, O., Guzzo, L., Meneux, B., et al. 2005a, A&A, 439, 877

Le Fèvre, O., Saisse, M., Mancini, D., et al. 2003, Instrument Design and Performance for Optical/Infrared Ground-based Telescopes.Masanori; Moorwood, Alan F. M. Proceedings of the SPIE, 4841, 1670

Le Fèvre, O., Vettolani, G., Garilli, B., et al. 2005b, A&A, 439, 845

Lonsdale, C. J., Smith, H. E., Rowan-Robinson, M., et al. 2003, PASP, 115, 897

Lynden-Bell, D. 1969, Nature, 223, 690

Magorrian, J., Tremaine, S., Richstone, D., et al. 1998, AJ, 115, 2285

Marconi, A. & Hunt, L. K. 2003, ApJ, 589, L21

Marconi, A., Risaliti, G., Gilli, R., et al. 2004, MNRAS, 351, 169

Marinoni, C., Le Fèvre, O., Meneux, B., et al. 2005, A&A, 442, 801

Markarian, B. E. 1967, Astrofizika, 3, 24

Marshall, H. L. 1985, ApJ, 299, 109

Martínez-Sansigre, A., Rawlings, S., Lacy, M., et al. 2005, Nature, 436, 666

Mathez, G. 1976, A&A, 53, 15

Matthews, T. A. & Sandage, A. R. 1963, ApJ, 138, 30

McCracken, H. J., Radovich, M., Bertin, E., et al. 2003, A&A, 410, 17

McLure, R. J. & Dunlop, J. S. 2001, MNRAS, 327, 199

McLure, R. J. & Dunlop, J. S. 2004, MNRAS, 352, 1390

Miller, P., Rawlings, S., & Saunders, R. 1993, MNRAS, 263, 425

Miyaji, T., Hasinger, G., & Schmidt, M. 2000, A&A, 353, 25

Morrissey, P., Schiminovich, D., Barlow, T. A., et al. 2005, ApJ, 619, L7

Netzer, H. 1990, in *Active Galactic Nuclei*, p. 137 (Blandford, R. D., Netzer, H., Woltjer,L., Courvosier,T. J.-L., & Mayor, M. Saas-Fee Advanced Course 20. Lecture Notes 1990. Swiss Society for Astrophysics and Astronomy, XII, Springer-Verlag Berlin Heidelberg New York)

Norman, C., Hasinger, G., Giacconi, R., et al. 2002, ApJ, 571, 218

Onken, C. A., Ferrarese, L., Merritt, D., et al. 2004, ApJ, 615, 645

Osmer, P. S. 1982, ApJ, 253, 28

Osterbrock, D. E. 1981, ApJ, 249, 462

Page, M. J., Mason, K. O., McHardy, I. M., Jones, L. R., & Carrera, F. J. 1997, MNRAS, 291, 324

Peterson, B. M., Ferrarese, L., Gilbert, K. M., et al. 2004, ApJ, 613, 682

Pierre, M., Valtchanov, I., Altieri, B., et al. 2004, Journal of Cosmology and Astro-Particle Physics, 9, 11

Pollo, A., Meneux, B., Guzzo, L., et al. 2005, A&A, 439, 887

Radovich, M., Arnaboldi, M., Ripepi, V., et al. 2004, A&A, 417, 51

Rees, M. J. 1984, ARA&A, 22, 471

Rengstorf, A. W., Mufson, S. L., Abad, C., et al. 2004, ApJ, 606, 741

Richards, G. T., Croom, S. M., Anderson, S. F., et al. 2005, MNRAS, 360, 839

Richards, G. T., Fan, X., Newberg, H. J., et al. 2002, AJ, 123, 2945

Richards, G. T., Lacy, M., Storrie-Lombardi, L. J., et al. 2006a, ApJS, 166, 470

Richards, G. T., Strauss, M. A., Fan, X., et al. 2006b, AJ, 131, 2766

Richstone, D., Ajhar, E. A., Bender, R., et al. 1998, Nature, 395, A14+

Rix, H.-W., Barden, M., Beckwith, S. V. W., et al. 2004, ApJS, 152, 163

Sajina, A., Lacy, M., & Scott, D. 2005, ApJ, 621, 256

Salpeter, E. E. 1964, ApJ, 140, 796

Schade, D., Crampton, D., Hammer, F., Le Fèvre, O., & Lilly, S. J. 1996, MNRAS, 278, 95

Schechter, P. 1976, ApJ, 203, 297

Schiminovich, D., Ilbert, O., Arnouts, S., et al. 2005, ApJ, 619, L47

Schlegel, D. J., Finkbeiner, D. P., & Davis, M. 1998, ApJ, 500, 525

Schmidt, M. 1963, Nature, 197, 1040

Schmidt, M. 1968, ApJ, 151, 393

Schmidt, M. & Green, R. F. 1983, ApJ, 269, 352

Schödel, R., Ott, T., Genzel, R., et al. 2003, ApJ, 596, 1015

Schödel, R., Ott, T., Genzel, R., et al. 2002, Nature, 419, 694

Scodeggio, M., Franzetti, P., Garilli, B., et al. 2005, A&A, 000, 00

Seyfert, C. K. 1943, ApJ, 97, 28

Shapiro, S. L. & Teukolsky, S. A. 1983, Black holes, white dwarfs, and neutron stars: The physics of compact objects (Research supported by the National Science Foundation. New York, Wiley-Interscience, 1983, 663 p.)

Slipher, V. M. 1917, Lowell Observatory Bulletin, 1, 59

Smith, M. G. 1975, ApJ, 202, 591

Steffen, A. T., Strateva, I., Brandt, W. N., et al. 2006, AJ, 131, 2826

Steidel, C. C., Adelberger, K. L., Giavalisco, M., Dickinson, M., & Pettini, M. 1999, ApJ, 519, 1

Strateva, I. V., Brandt, W. N., Schneider, D. P., Vanden Berk, D. G., & Vignali, C. 2005, AJ, 130, 387

Strittmatter, P. A., Hill, P., Pauliny-Toth, I. I. K., Steppe, H., & Witzel, A. 1980, A&A, 88, L12

Szokoly, G. P., Bergeron, J., Hasinger, G., et al. 2004, ApJS, 155, 271

Tananbaum, H., Avni, Y., Branduardi, G., et al. 1979, ApJ, 234, L9

Treister, E., Urry, C. M., Van Duyne, J., et al. 2006, ApJ, 640, 603

Tremonti, C. A., Heckman, T. M., Kauffmann, G., et al. 2004, ApJ, 613, 898

Urry, C. M. & Padovani, P. 1995, PASP, 107, 803

Vanden Berk, D. E., Richards, G. T., Bauer, A., et al. 2001, AJ, 122, 549

Vanden Berk, D. E., Schneider, D. P., Richards, G. T., et al. 2005, AJ, 129, 2047

Vanden Berk, D. E., Wilhite, B. C., Kron, R. G., et al. 2004, ApJ, 601, 692

Veron-Cetty, M. P. & Veron, P. 2006, VizieR Online Data Catalog, 7248, 0

Vestergaard, M. & Peterson, B. M. 2006, ApJ, 641, 689

Vestergaard, M. & Wilkes, B. J. 2001, ApJS, 134, 1

Vignali, C., Brandt, W. N., & Schneider, D. P. 2003, AJ, 125, 433

Wandel, A., Peterson, B. M., & Malkan, M. A. 1999, ApJ, 526, 579

White, R. L., Becker, R. H., Gregg, M. D., et al. 2000, ApJS, 126, 133

Wilkes, B. J., Tananbaum, H., Worrall, D. M., et al. 1994, ApJS, 92, 53

Wisotzki, L., Christlieb, N., Bade, N., et al. 2000, A&A, 358, 77

Wolf, C., Wisotzki, L., Borch, A., et al. 2003, A&A, 408, 499

Zakamska, N. L., Strauss, M. A., Krolik, J. H., et al. 2003, AJ, 126, 2125

Zamorani, G., Marano, B., Mignoli, M., Zitelli, V., & Boyle, B. J. 1992, MNRAS, 256, 238

Zel'Dovich, Y. B. & Novikov, I. D. 1964, Doklady Akad. Nauk. SSSR 164, 158, 311

Zucca, E., Ilbert, O., Bardelli, S., et al. 2005, ArXiv Astrophysics e-prints

Appendix A

Catalog Tables

Table A.1: BLAGN with secure redshift (flags 14 and 13).

Object ID	α_{J2000}	δ_{J2000}	z	$flag$	I_{AB}	B_{AB}	V_{AB}	R_{AB}	$Morphology^{(*)}$
CDFS:	deep mode	10 AGN							
000037103	$03^h32^m37.47^s$	$-27^o40^m00.33^s$	0.6656	14	21.84	–	–	–	–
000037399	$03^h32^m38.14^s$	$-27^o39^m45.02^s$	0.8366	14	20.44	–	–	–	–
000073509	$03^h32^m02.47^s$	$-27^o46^m00.53^s$	1.6199	$14^{(S)}$	23.62	–	–	–	–
000023526	$03^h32^m43.25^s$	$-27^o49^m14.38^s$	1.9199	$14^{(S)}$	22.17	–	–	–	–
000028880	$03^h33^m03.62^s$	$-27^o45^m18.97^s$	1.2574	14	22.71	–	–	–	–
000029274	$03^h32^m30.23^s$	$-27^o45^m04.75^s$	0.7352	14	21.62	–	–	–	–
000018607	$03^h32^m18.26^s$	$-27^o52^m41.42^s$	2.8010	14	23.91	–	–	–	–
000025363	$03^h32^m59.85^s$	$-27^o47^m48.42^s$	2.5673	14	21.95	–	–	–	–
000033629	$03^h32^m25.17^s$	$-27^o42^m19.05^s$	1.6207	14	22.14	–	–	–	–
000031947	$03^h32^m00.37^s$	$-27^o43^m19.85^s$	1.0401	$14^{(S)}$	22.12	–	–	–	–
0226-04	deep mode	56 AGN							
020176565	$02^h25^m28.06^s$	$-04^o36^m41.59^s$	1.5039	14	23.24	23.62	23.61	23.26	–
020158952	$02^h26^m17.81^s$	$-04^o39^m08.50^s$	0.8738	14	21.41	22.82	22.16	21.99	extended
020086859	$02^h26^m29.62^s$	$-04^o49^m14.41^s$	1.1921	13	20.97	22.98	21.97	21.43	point-like
020213000	$02^h26^m47.88^s$	$-04^o31^m35.20^s$	1.2250	13	21.44	22.30	22.02	21.76	point-like
020212038	$02^h26^m08.40^s$	$-04^o31^m43.15^s$	2.2082	$14^{(F)}$	21.46	22.91	22.27	22.02	extended
020131908	$02^h26^m51.04^s$	$-04^o42^m56.55^s$	2.7813	14	22.34	23.08	22.75	22.76	extended
020210524	$02^h27^m07.55^s$	$-04^o32^m02.98^s$	1.5150	14	20.41	21.03	20.90	20.64	point-like
020120394	$02^h26^m59.92^s$	$-04^o44^m30.32^s$	1.6120	14	20.38	21.27	20.96	20.78	point-like
020114448	$02^h27^m00.99^s$	$-04^o45^m16.83^s$	1.6140	13	22.24	23.39	23.35	22.97	point-like
020118986	$02^h26^m54.53^s$	$-04^o44^m37.72^s$	3.3018	14	23.57	25.42	23.98	23.97	–
020118483	$02^h27^m36.06^s$	$-04^o44^m41.89^s$	1.2606	13	22.86	23.82	23.44	23.30	–
020188089	$02^h25^m25.68^s$	$-04^o35^m09.45^s$	2.1384	14	20.66	21.12	20.94	20.95	point-like
020147295	$02^h25^m29.19^s$	$-04^o40^m44.16^s$	1.5562	$14^{(F)}$	22.59	23.87	23.44	22.84	–
020169816	$02^h25^m45.04^s$	$-04^o37^m35.95^s$	3.5893	$14^{(F)}$	22.14	24.67	22.95	22.64	point-like
020190479	$02^h25^m45.55^s$	$-04^o34^m45.18^s$	0.1524	14	21.33	21.99	21.55	21.64	point-like
020268754	$02^h26^m09.63^s$	$-04^o24^m37.74^s$	2.7187	14	20.59	20.56	20.60	20.75	point-like
020164607	$02^h25^m32.46^s$	$-04^o38^m18.63^s$	2.9220	14	23.11	23.92	23.46	23.21	–
020179116	$02^h25^m34.98^s$	$-04^o36^m16.46^s$	3.3080	$14^{(F)}$	23.89	25.18	23.94	23.84	–
020237445	$02^h25^m57.38^s$	$-04^o28^m46.04^s$	1.2138	14	22.43	23.92	23.53	23.06	extended
020223153	$02^h26^m17.52^s$	$-04^o30^m29.27^s$	1.4777	$14^{(F)}$	20.65	21.18	21.05	20.94	point-like
020163018	$02^h26^m45.20^s$	$-04^o38^m30.58^s$	1.3208	$14^{(F)}$	23.11	23.89	23.62	23.29	–
020180665	$02^h26^m45.46^s$	$-04^o36^m15.43^s$	3.2619	14	18.14	21.09	19.32	19.03	point-like
020177875	$02^h26^m53.87^s$	$-04^o36^m27.21^s$	1.6821	13	22.53	24.01	23.65	23.36	–
020234610	$02^h26^m58.99^s$	$-04^o29^m06.02^s$	2.1645	13	23.87	26.05	25.11	24.74	–
020159510	$02^h27^m09.85^s$	$-04^o39^m02.21^s$	1.9309	14	21.97	22.73	22.41	22.44	point-like
020218399	$02^h27^m31.34^s$	$-04^o30^m50.26^s$	2.2255	14	22.19	22.91	22.39	22.53	point-like
020254511	$02^h27^m36.93^s$	$-04^o26^m31.30^s$	1.7466	14	20.66	20.76	20.84	20.85	point-like
020243922	$02^h27^m47.33^s$	$-04^o27^m53.20^s$	1.1203	14	21.29	22.02	21.71	21.60	point-like
020165108	$02^h26^m59.85^s$	$-04^o38^m12.68^s$	1.3219	13	23.09	24.70	24.04	23.78	–
020179225	$02^h27^m02.15^s$	$-04^o36^m15.96^s$	1.3860	13	22.39	23.90	23.50	23.01	point-like
020195823	$02^h27^m24.10^s$	$-04^o33^m55.72^s$	2.4250	$14^{(F)}$	23.38	24.19	23.61	23.85	–
020254576	$02^h25^m27.23^s$	$-04^o26^m31.02^s$	3.8527	14	21.15	23.33	21.78	21.44	point-like
020200020	$02^h25^m50.40^s$	$-04^o33^m24.00^s$	2.7373	13	21.91	21.95	22.10	21.73	point-like
020329650	$02^h26^m08.71^s$	$-04^o16^m34.53^s$	1.0498	14	20.84	21.52	21.14	20.96	point-like
020232397	$02^h26^m26.04^s$	$-04^o29^m27.88^s$	1.6280	$14^{(F)}$	22.69	23.72	23.31	23.15	–
020461765	$02^h26^m35.95^s$	$-04^o23^m21.81^s$	3.2831	14	22.89	24.62	23.01	22.87	–
020466135	$02^h26^m46.99^s$	$-04^o18^m37.56^s$	1.5806	14	21.13	21.29	21.56	21.05	point-like
020467962	$02^h26^m59.17^s$	$-04^o16^m55.89^s$	3.3247	13	23.59	25.22	23.96	23.80	–
020461459	$02^h27^m04.25^s$	$-04^o23^m37.77^s$	1.8211	13	21.60	23.50	22.92	22.41	point-like
020465339	$02^h27^m06.44^s$	$-04^o19^m24.30^s$	3.2852	14	21.09	21.77	21.31	20.99	point-like
020467628	$02^h27^m04.06^s$	$-04^o17^m09.77^s$	1.3582	13	21.35	21.97	21.82	21.61	point-like

Table A.1: continued.

Object ID	α_{J2000}	δ_{J2000}	z	$flag$	I_{AB}	B_{AB}	V_{AB}	R_{AB}	$Morphology^{(*)}$
020205812	$02^h27^m23.84^s$	$-04^o32^m31.69^s$	2.8922	14	23.87	24.77	24.36	24.52	–
020208084	$02^h27^m29.24^s$	$-04^o32^m27.51^s$	2.2850	$14^{(F)}$	19.04	19.34	19.10	19.12	point-like
020277536	$02^h27^m53.85^s$	$-04^o23^m20.10^s$	3.6260	14	23.55	25.25	23.88	23.60	–
020278210	$02^h27^m40.00^s$	$-04^o23^m17.43^s$	1.7574	13	21.36	22.68	21.87	22.28	point-like
020239945	$02^h27^m31.14^s$	$-04^o28^m22.83^s$	2.4247	$14^{(F)}$	22.90	23.65	23.13	23.14	–
020351846	$02^h26^m30.84^s$	$-04^o13^m26.09^s$	3.5680	$14^{(F)}$	22.80	25.05	23.71	23.24	–
020367106	$02^h26^m34.71^s$	$-04^o11^m33.98^s$	1.3973	$14^{(F)}$	22.42	23.28	23.02	22.55	extended
020351277	$02^h25^m57.41^s$	$-04^o13^m39.43^s$	0.6061	14	19.83	20.60	20.39	20.32	extended
020258622	$02^h26^m20.06^s$	$-04^o25^m54.51^s$	1.3386	14	22.74	24.45	23.84	23.46	–
020286836	$02^h26^m22.17^s$	$-04^o22^m21.62^s$	2.0060	14	18.51	19.28	19.11	19.05	point-like
020291309	$02^h26^m31.23^s$	$-04^o21^m28.87^s$	1.9930	14	22.89	23.95	23.56	23.81	–
020465540	$02^h26^m44.48^s$	$-04^o19^m16.76^s$	2.7372	14	23.58	24.15	23.94	23.81	–
020302785	$02^h26^m24.63^s$	$-04^o20^m02.14^s$	2.2357	14	21.01	21.42	21.26	21.34	point-like
020364478	$02^h26^m49.41^s$	$-04^o11^m53.30^s$	1.1573	14	21.74	22.94	22.74	22.25	extended
020463196	$02^h27^m00.65^s$	$-04^o21^m49.00^s$	1.3875	14	23.27	24.49	24.42	23.91	–
1003+01	wide mode	18 AGN							
100122852	$10^h02^m11.17^s$	$+01^o22^m28.58^s$	1.8007	14	19.86	–	–	–	point-like
100110223	$10^h02^m48.14^s$	$+01^o20^m02.29^s$	1.8255	13	21.30	–	–	–	point-like
100210521	$10^h03^m27.33^s$	$+01^o35^m50.91^s$	1.1723	14	21.59	22.05	21.73	21.56	point-like
100139500	$10^h02^m57.37^s$	$+01^o25^m40.38^s$	1.2478	13	20.96	–	–	–	point-like
100126868	$10^h03^m08.80^s$	$+01^o23^m16.56^s$	2.3302	14	20.34	–	–	–	point-like
100105943	$10^h03^m46.33^s$	$+01^o19^m11.04^s$	3.5553	13	21.15	–	–	–	point-like
100290682	$10^h03^m11.33^s$	$+01^o47^m01.56^s$	1.5487	$14^{(F)}$	21.45	–	–	–	extended
100327652	$10^h03^m13.81^s$	$+01^o52^m13.97^s$	1.2173	14	22.39	23.85	23.43	22.90	extended
100232259	$10^h03^m30.37^s$	$+01^o38^m51.18^s$	1.7647	14	21.09	21.37	21.30	21.33	point-like
100190464	$10^h04^m25.14^s$	$+01^o33^m07.74^s$	1.0760	14	21.66	22.98	22.38	22.41	extended
100168207	$10^h04^m36.55^s$	$+01^o30^m05.86^s$	2.7152	14	22.40	22.38	21.84	22.14	point-like
100113463	$10^h04^m07.25^s$	$+01^o20^m38.90^s$	1.8436	14	20.47	–	–	–	point-like
100123590	$10^h04^m46.72^s$	$+01^o22^m39.10^s$	2.0963	13	21.47	–	–	–	point-like
100343840	$10^h04^m32.08^s$	$+01^o54^m24.12^s$	2.3666	$14^{(F)}$	19.75	20.68	20.40	20.15	point-like
100338914	$10^h04^m13.45^s$	$+01^o53^m41.38^s$	1.1584	14	19.73	20.15	19.80	19.78	extended
100245809	$10^h04^m00.36^s$	$+01^o40^m45.74^s$	3.0789	14	21.62	22.71	22.01	21.94	point-like
100241696	$10^h04^m11.84^s$	$+01^o40^m06.47^s$	1.1112	13	21.95	22.59	21.89	22.19	point-like
100451895	$10^h04^m38.01^s$	$+02^o09^m25.07^s$	1.7806	13	20.03	20.46	20.31	20.36	point-like
2217+00	wide mode	31 AGN							
220586430	$22^h14^m34.82^s$	$+00^o19^m24.18^s$	1.0285	14	20.35	–	–	–	point-like
220568559	$22^h14^m43.23^s$	$+00^o14^m16.29^s$	1.4980	13	22.10	–	–	–	point-like
220566905	$22^h14^m02.39^s$	$+00^o13^m49.58^s$	1.5285	13	22.28	–	–	–	point-like
220554336	$22^h14^m44.17^s$	$+00^o10^m02.54^s$	0.4470	14	21.02	–	–	–	point-like
220001963	$22^h13^m51.58^s$	$+00^o25^m01.30^s$	2.6801	14	22.19	–	–	–	point-like
220010371	$22^h14^m28.40^s$	$+00^o27^m32.40^s$	3.6952	14	21.79	–	–	–	point-like
220056847	$22^h14^m48.77^s$	$+00^o41^m16.67^s$	3.0015	14	21.38	–	–	–	point-like
220567825	$22^h15^m08.48^s$	$+00^o14^m04.38^s$	1.1601	13	21.07	–	–	–	point-like
220576817	$22^h15^m09.17^s$	$+00^o16^m42.38^s$	3.0957	14	21.81	–	–	–	point-like
220536609	$22^h15^m31.65^s$	$+00^o04^m18.31^s$	0.4970	14	21.10	–	–	–	extended
220041929	$22^h15^m09.54^s$	$+00^o36^m39.11^s$	1.4751	13	18.24	–	–	–	extended
220090821	$22^h15^m46.25^s$	$+00^o50^m58.51^s$	1.8326	13	20.40	–	–	–	point-like
220082140	$22^h15^m32.40^s$	$+00^o48^m36.29^s$	1.8484	$14^{(F)}$	20.58	–	–	–	point-like
220055529	$22^h15^m54.10^s$	$+00^o40^m55.47^s$	3.5941	13	21.42	–	–	–	point-like
220567863	$22^h16^m27.06^s$	$+00^o14^m02.32^s$	2.1610	14	20.80	–	–	–	point-like
220567224	$22^h16^m44.02^s$	$+00^o13^m48.54^s$	5.0042	14	20.07	–	22.90	–	point-like
220591287	$22^h16^m49.05^s$	$+00^o20^m46.27^s$	1.2968	$14^{(F)}$	22.30	23.47	23.32	–	extended
220580912	$22^h15^m56.66^s$	$+00^o17^m52.28^s$	3.0432	13	22.11	–	–	–	point-like
220107230	$22^h16^m56.10^s$	$+00^o56^m00.77^s$	1.0937	13	21.64	–	–	–	point-like

Table A.1: continued.

Object ID	α_{J2000}	δ_{J2000}	z	$flag$	I_{AB}	B_{AB}	V_{AB}	R_{AB}	$Morphology^{(*)}$
220575888	$22^h17^m36.55^s$	$+00^o16^m23.09^s$	3.0755	14	21.25	22.16	21.50	–	point-like
220556037	$22^h17^m05.53^s$	$+00^o10^m19.85^s$	2.7422	14	19.46	20.52	20.29	–	point-like
220542377	$22^h17^m10.42^s$	$+00^o06^m04.72^s$	1.3097	13	21.12	22.24	21.95	–	point-like
220554600	$22^h17^m36.64^s$	$+00^o10^m05.86^s$	1.3689	$14^{(F)}$	20.65	21.21	21.00	–	point-like
220544855	$22^h17^m39.71^s$	$+00^o06^m52.80^s$	2.2934	$14^{(F)}$	20.91	21.97	21.61	–	extended
220044408	$22^h17^m34.47^s$	$+00^o37^m33.52^s$	2.9096	$14^{(F)}$	21.18	21.65	21.54	–	point-like
220093875	$22^h17^m48.64^s$	$+00^o51^m50.39^s$	1.3365	$14^{(F)}$	21.83	–	–	–	point-like
220081925	$22^h18^m00.42^s$	$+00^o48^m31.41^s$	1.2167	13	21.68	22.79	22.40	–	extended
220609820	$22^h18^m29.04^s$	$+00^o20^m24.32^s$	1.4794	$14^{(F)}$	21.52	22.04	21.86	–	extended
220610034	$22^h18^m14.20^s$	$+00^o20^m49.73^s$	1.5135	$14^{(F)}$	20.54	20.77	20.86	–	extended
220613346	$22^h18^m33.73^s$	$+00^o27^m09.76^s$	1.2530	$14^{(F)}$	20.39	21.63	21.25	–	extended
220098629	$22^h18^m01.51^s$	$+00^o53^m19.83^s$	2.5790	$14^{(F)}$	21.71	–	–	–	point-like

$^{(*)}$ Morphological classification for objects with $I_{AB} < 22.5$. Objects in the VVDS-CDFS field are not classified. See Sect. 3.5.1;

$^{(F)}$ AGN re-observed in the 3800-6500 range with FORS1 in our follow-up program;

$^{(S)}$ Redshift confirmed by matching the catalog from Szokoly et al. (2004).

Object ID	α_{J2000}	δ_{J2000}	λ_{BL}	*z solutions*	I_{AB}	B_{AB}	V_{AB}	R_{AB}	*Morphology*$^{(*)}$
CDFS:	deep mode	2 AGN							
000031270	$03^h32^m57.74^s$	$-27^o43^m50.12^s$	7319.	$0.1150^a\ 1.6150^b$	23.52	–	–	–	–
000017025	$03^h31^m54.30^s$	$-27^o53^m49.58^s$	6500.	$1.3220^b\ 2.4050^c\ 3.1960^d$	23.70	–	–	–	–
0226-04 :	deep mode	6 AGN							
020137737	$02^h26^m47.76^s$	$-04^o42^m04.06^s$	6320.	$1.2580^b\ 2.3110^c\ 3.0800^d$	23.78	24.58	24.14	24.16	–
020225567	$02^h27^m06.42^s$	$-04^o30^m14.34^s$	6558.	$1.3430^b\ 2.4350^c$	23.07	24.65	24.26	23.74	–
020281035	$02^h26^m12.30^s$	$-04^o22^m51.63^s$	6805.	$0.0370^a\ 1.4310^b\ 2.5650^c\ 3.3930^d$	23.93	25.06	24.39	24.07	–
020375508	$02^h25^m48.99^s$	$-04^o10^m28.04^s$	5963.	$1.1300^b\ 2.1240^c\ 2.8500^d$	22.54	23.25	22.98	23.04	–
020293248	$02^h26^m25.92^s$	$-04^o21^m12.73^s$	7335.	$0.1180^a\ 1.6210^b$	23.25	24.79	24.54	24.13	–
020469530	$02^h26^m49.92^s$	$-04^o15^m17.44^s$	6701.	$0.0210^a\ 1.3940^b\ 2.5100^c\ 3.3260^d$	23.50	24.69	24.35	24.28	–
2217+00:	wide mode	7 AGN							
220593613	$22^h14^m11.61^s$	$+00^o21^m29.15^s$	6893.	$0.0500^a\ 1.4630^b\ 2.6110^c$	21.90	–	–	–	extended
220056092	$22^h13^m53.81^s$	$+00^o41^m06.90^s$	6100.	$1.1790^b\ 2.1950^c$	22.08	–	–	–	point-like
220583713	$22^h15^m34.70^s$	$+00^o18^m42.01^s$	7352.	$0.1200^a\ 1.6270^b$	21.88	–	–	–	point-like
220548678	$22^h15^m02.71^s$	$+00^o08^m10.56^s$	6766.	$0.0310^a\ 1.4170^b\ 2.5440^c$	21.97	–	–	–	point-like
220023681	$22^h17^m46.44^s$	$+00^o31^m26.58^s$	6956.	$0.0600^a\ 1.4850^b\ 2.6440^c$	21.71	24.33	23.25	–	point-like
220551735	$22^h18^m05.78^s$	$+00^o09^m12.66^s$	8056.	$0.2270^a\ 1.8780^b$	21.12	21.73	21.72	–	point-like
220234909	$22^h18^m13.40^s$	$+00^o48^m54.05^s$	6407.	$1.2890^b\ 2.3560^c\ 3.1360^d$	21.88	23.40	22.55	–	extended

Table A.2: AGN with a single emission line detected (flag 19).

$^{(*)}$ Morphological classification for objects with $I_{AB} < 22.5$. Objects in the VVDS-CDFS field are not classified. See Sect. 3.5.1

^{a} Emission line identified as Hα.

^{b} Emission line identified as MgII.

^{c} Emission line identified as C III].

^{d} Emission line identified as CIV .

Appendix B

Spectra

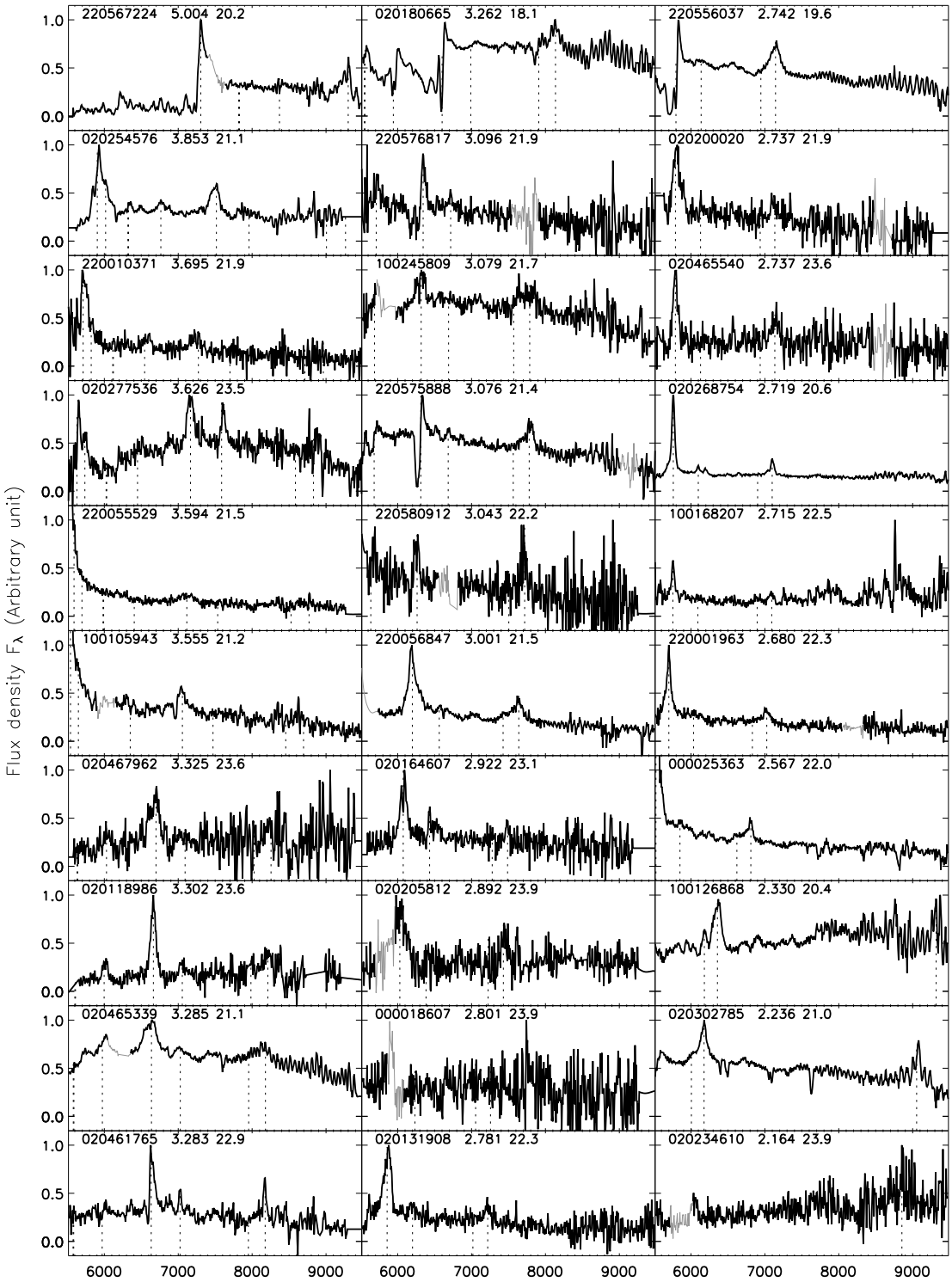

Figure B.1: Spectra of AGN with a secure redshift (page 1/3). Spectra are not re-binned. Wavelength ranges contaminated by a zeroth-order are plotted in light gray.

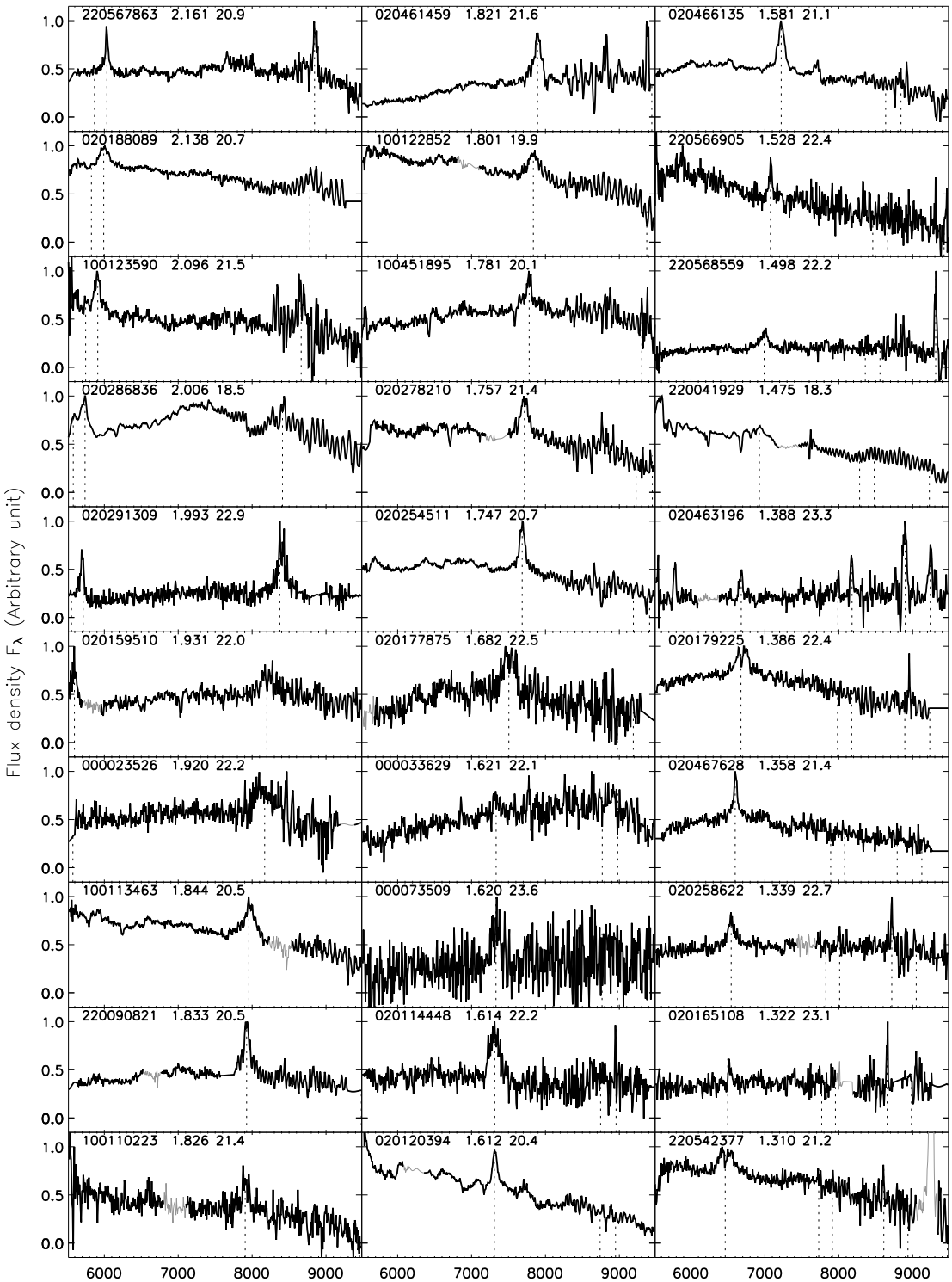

Figure B.1 Spectra of AGN with a secure redshift (page 2/3).

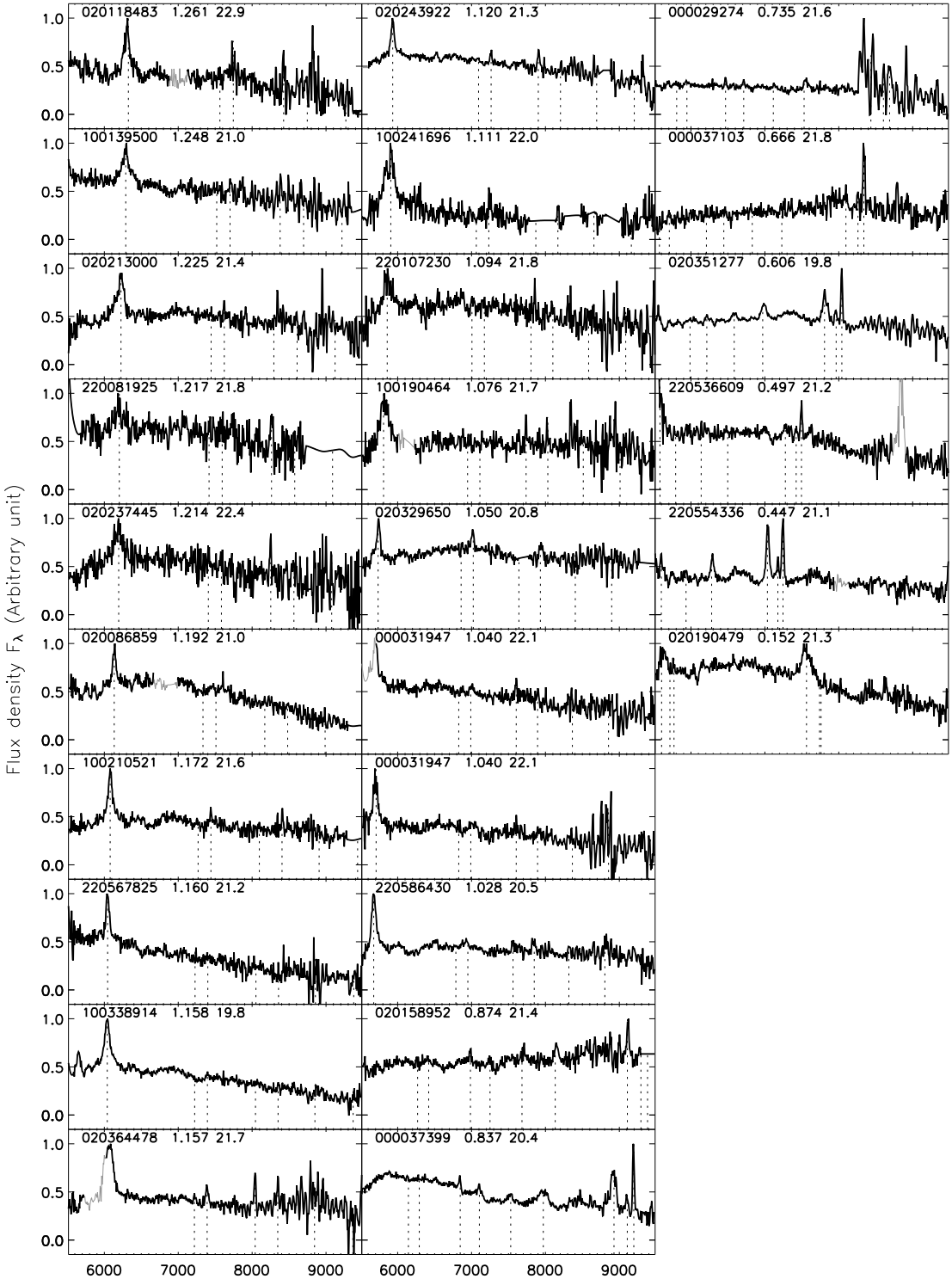

Figure B.1 Spectra of AGN with a secure redshift (page 3/3).

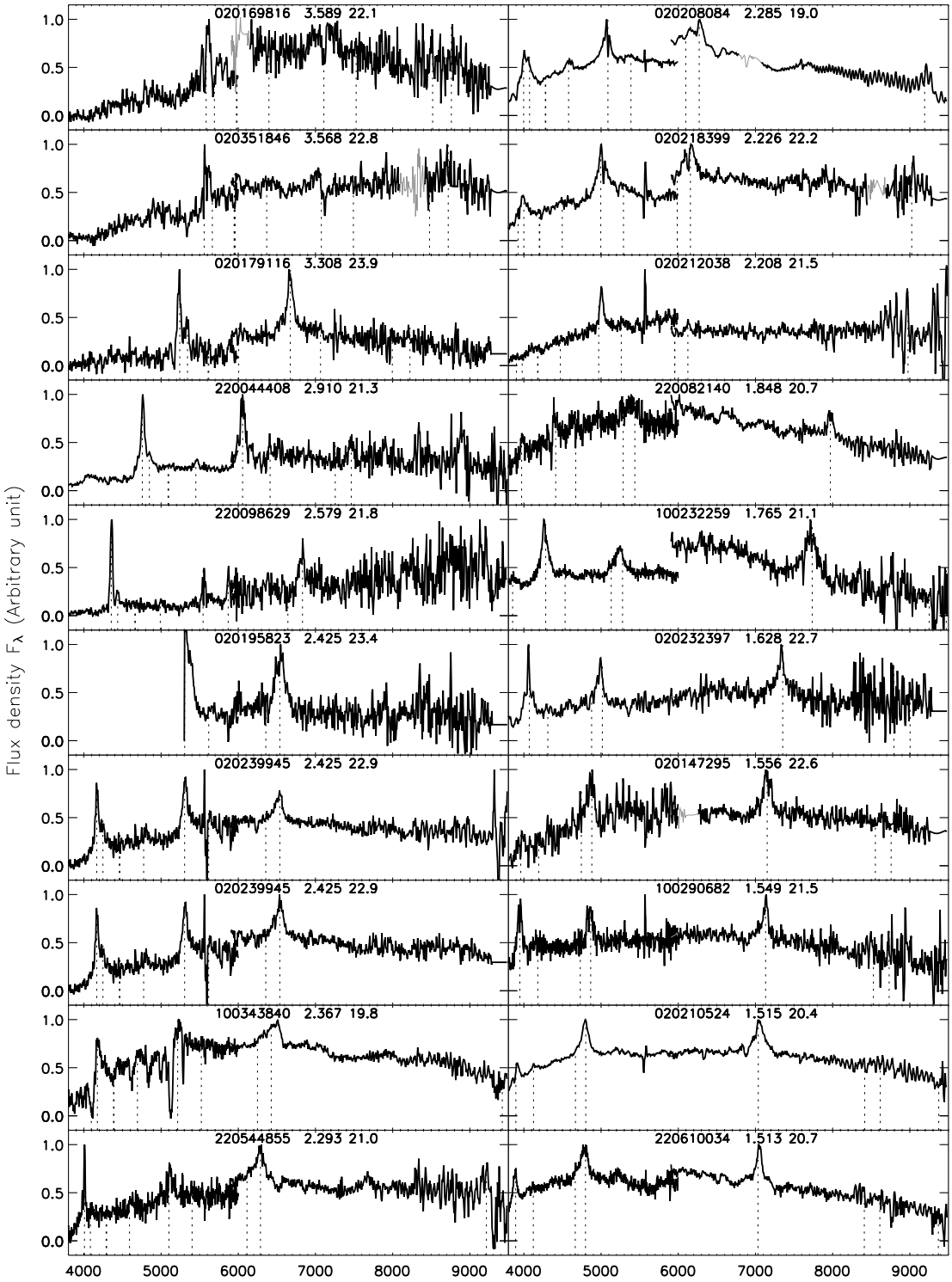

Figure B.2: Spectra of AGN for which the redshift was resolved with FORS re-observation (page 1/2). FORS spectra are rebinned to 5 pixels.

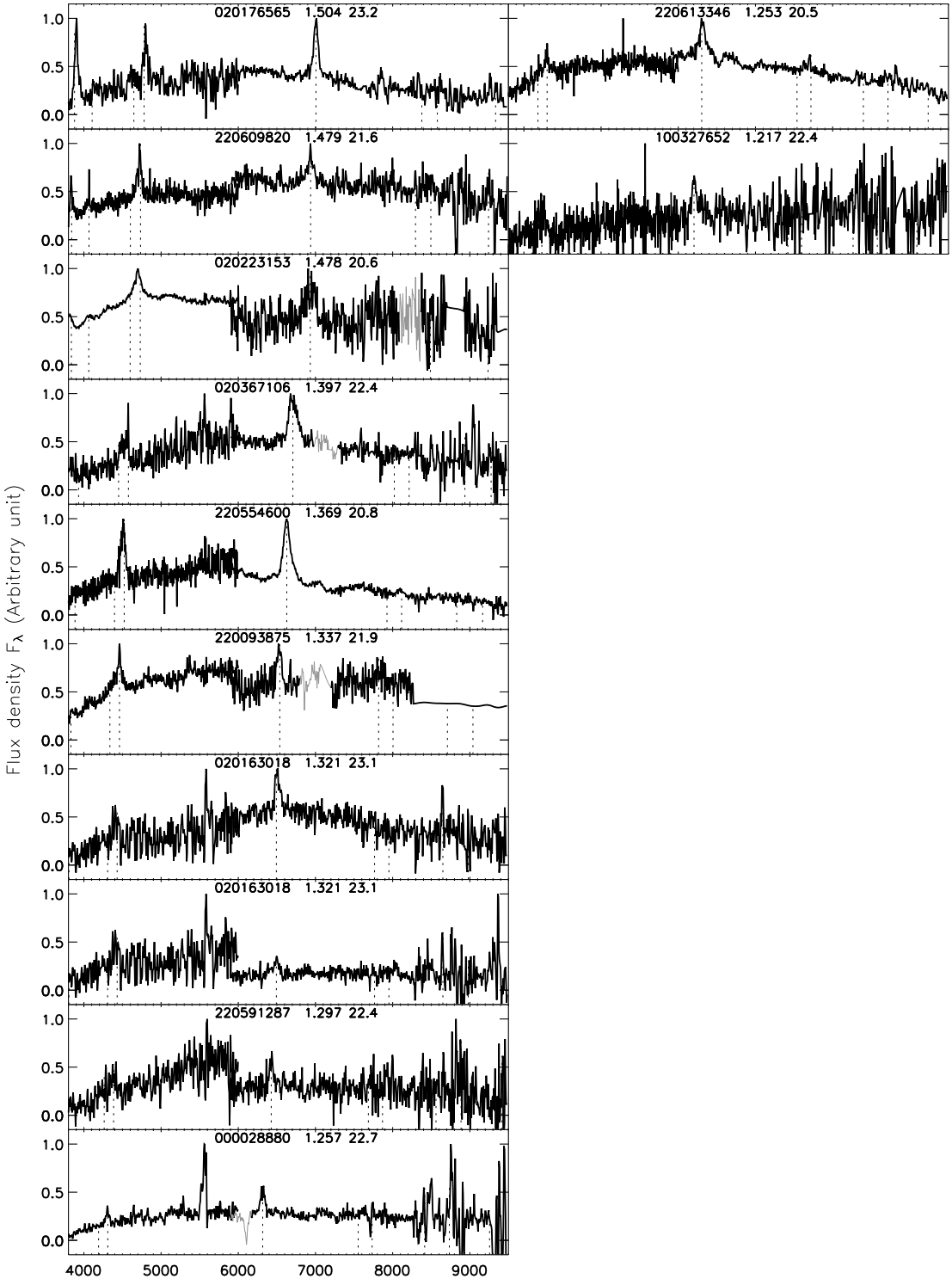

Figure B.2 Spectra of AGN for which the redshift was resolved with FORS re-observation (page 2/2).

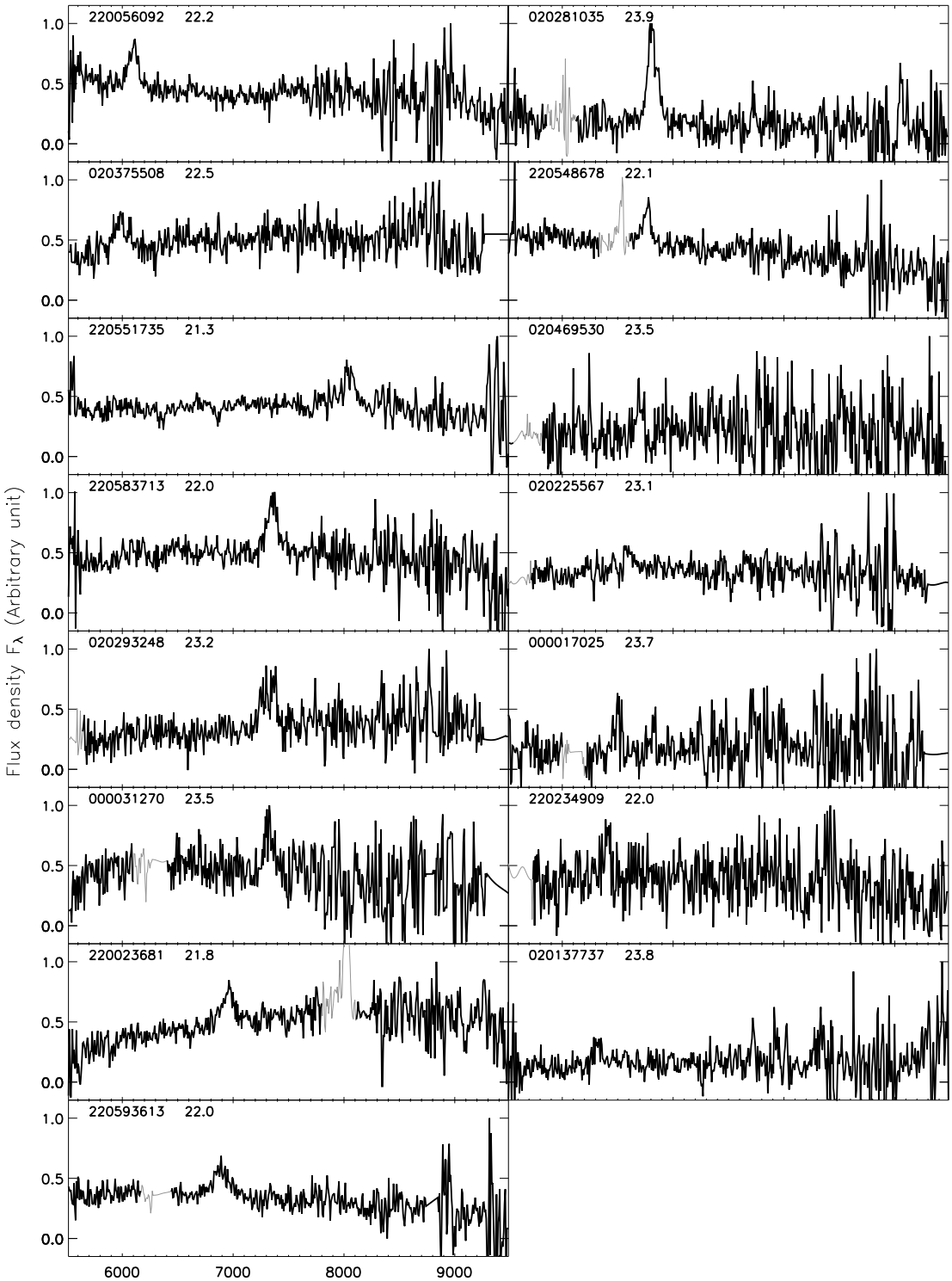

Figure B.3: Spectra of AGN remaining with a degenerate redshift. Spectra are not re-binned. Wavelength ranges contaminated by a zeroth-order are plotted in light grey.

Appendix C

Theoretical S/N threshold to recognize a resolved emission line

In the VVDS sample most of the AGN where manually classified. Therefore there is no formal S/N threshold from which a broad emission line will be recognized as such by the reducer. However, we can try to estimate such a threshold with reasonable hypothesis:

First we assume, a Gaussian emission line profile. For a normalized spectrum and after subtraction of the continuum, the flux of a Gaussian emission line profile is described as following:

$$f(\lambda) = \frac{EW}{\sigma\sqrt{2\pi}} exp\left(-\frac{1}{2}\left(\frac{\lambda-\lambda_0}{\sigma}\right)^2\right)$$

$$\text{Half of the maximum flux is: } f_{FWHM} = \frac{EW}{2\sigma\sqrt{2\pi}} \quad \text{(C.1)}$$

$$\text{and } FWHM = 2\sigma\sqrt{2ln2} \quad \text{(C.2)}$$

Second, we consider that a resolved line will be picked out if the flux in the emission line core (we consider here the wavelength range enclosed by the FWHM) exceed 3.5 times the noise level of the continuum. This noise level is adjusted for the oversampling of the broad emission line with a factor $1/\sqrt{n}$ (n is the number of pixel covered by the line core). This condition can be written as following:

$$f_{FWHM} > \frac{3.5}{S/N\sqrt{n}} \quad \text{(C.3)}$$

d being the number of pixels per Ångström, we have $n = d \times FWHM$.

Introducing this relation with equation C.1 and C.2 in the inequality C.3 , we obtain a theoretical S/N threshold to detect a line:

$$\frac{EW}{2\sigma\sqrt{2\pi}} > \frac{3.5}{S/N\sqrt{d \times FWHM}}$$

$$\frac{EW\sqrt{ln2}}{FWHM\sqrt{\pi}} > \frac{3.5}{S/N\sqrt{d \times FWHM}}$$

$$S/N > \frac{3.5\sqrt{\pi}}{\sqrt{ln2}} \frac{\sqrt{\frac{FWHM}{d}}}{EW}$$

$$\text{finally: } \boxed{S/N_{limit} \sim 7.5 \frac{\sqrt{\frac{FWHM}{d}}}{EW}}$$

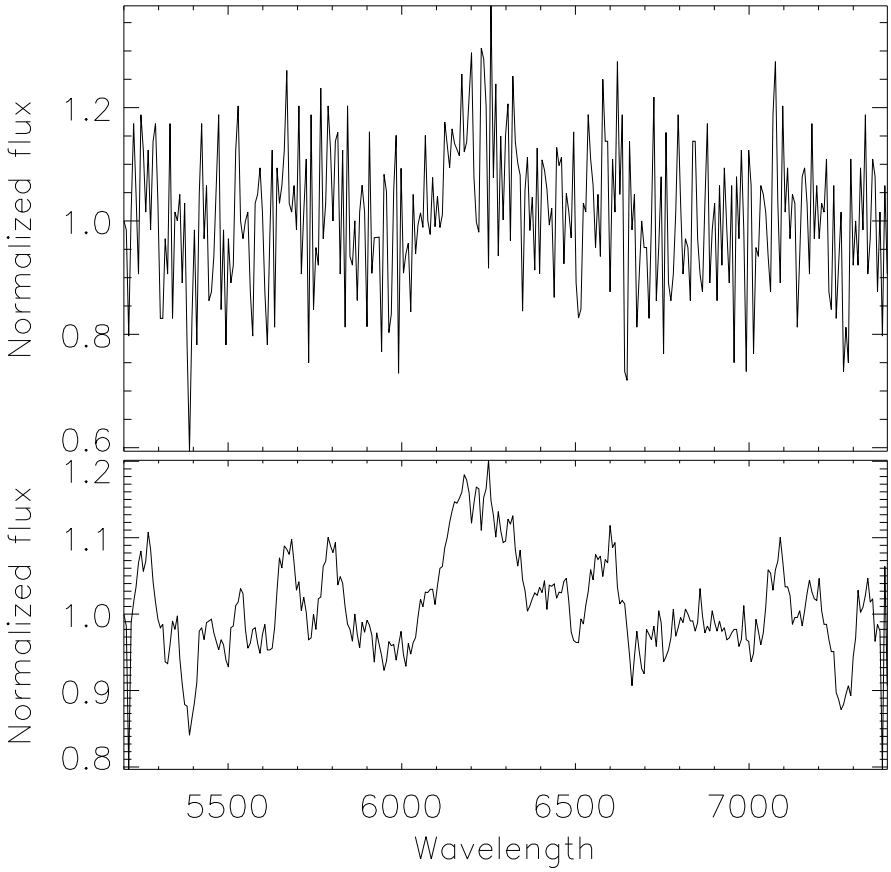

Figure C.1: Top panel: Gaussian emission line simulated for our theoretical detection limit. Bottom panel: The same after smoothing with a 7 pixel window. The parameters considered in this example are: $S/N = 8; z = 3.5$; $\lambda_{0,rest} = 1500.$Å; $EW_{rest} = 9.1$Å; $\sigma_{rest} = 3000\mathrm{km\,s^{-1}}$. The noise obeys to a normal distribution.

Appendix D

Emission lines properties

Table D.1: Spectral parameters of the C IV emission lines.

Object ID	EW [Å]	FWHM [km s^{-1}]	σ_l [km s^{-1}]	SN	$\log \frac{L_{BOL}}{1\ erg.s^{-1}}$	$\log \frac{M_{BH}}{M_\odot}$
020254576	44.7	5980.	3234.	12.4	45.6920	8.35
220010371	40.4	6181.	3301.	2.5	45.5200	8.27
020277536	42.9	4779.	3275.	8.0	44.4434	7.70
220055529	25.8	8723.	3379.	5.7	45.6911	8.38
020169816	27.4	15206.	5006.	5.2	45.2876	8.52
020351846	$>$ 13.1	13008.	-99.	10.1	-99	-99
100105943	$>$ 27.0	4854.	-99.	9.5	-99	-99
020467962	88.0	7349.	3404.	2.5	44.2517	7.63
020179116	66.3	3849.	3473.	5.5	44.4174	7.73
020118986	145.1	2891.	2420.	3.1	44.3722	7.39
020465339	31.1	8868.	3800.	121.4	45.5656	8.42
020461765	$>$ 58.0	3226.	-99.	12.5	-99	-99
020180665	$>$ 5.6	3242.	-99.	-99.0	-99	-99
220576817	$>$ 33.8	3711.	-99.	3.6	-99	-99
100245809	25.6	6776.	3592.	11.7	45.2977	8.23
220575888	$>$ 15.8	6781.	-99.	-99.0	-99	-99
220580912	$>$ 33.3	3760.	-99.	2.5	-99	-99
220056847	86.4	4489.	3363.	14.1	45.4302	8.24
020164607	77.8	5285.	2925.	3.5	44.7175	7.74
220044408	68.4	3181.	2819.	3.6	45.3895	8.07
020205812	119.5	8166.	4241.	1.8	44.2665	7.83
000018607	31.6	5090.	2365.	2.3	44.3187	7.34
020131908	120.9	6213.	3323.	3.6	45.0521	8.03
220556037	$>$ 16.4	5908.	-99.	-99.0	-99	-99
020200020	75.6	4807.	2730.	4.2	45.3187	8.00
020465540	65.8	3328.	1709.	2.8	44.4395	7.11
020268754	91.2	2601.	2218.	42.1	45.5830	7.95
100168207	42.1	2232.	2804.	6.5	44.7202	7.70
220001963	83.0	3004.	2899.	7.4	45.0159	7.89

Table D.2: Spectral parameters of the C III] emission lines.

Object ID	EW [Å]	FWHM [km s^{-1}]	σ_l [km s^{-1}]	SN
020461765	36.6	1571.	1783.	3.4
100245809	27.6	10309.	3901.	9.1
220575888	28.2	4127.	3087.	11.5
220580912	45.8	3455.	2605.	2.5
220056847	51.1	5464.	3526.	8.1
020164607	11.0	1429.	2931.	3.1
220044408	10.2	3442.	1533.	4.0
020205812	30.6	4033.	1617.	2.6
020131908	31.3	2827.	3201.	3.1
220556037	38.5	5993.	3248.	31.7
020200020	47.7	2700.	3535.	2.5
020465540	41.0	4200.	2240.	2.6
020268754	25.3	2111.	2467.	28.9
220001963	35.1	4266.	3246.	7.2
220098629	24.5	2820.	5033.	3.7
000025363	33.6	3458.	3385.	18.7
020195823	83.7	5968.	2691.	3.4
020239945	26.7	4868.	2950.	15.1
100343840	21.7	9326.	3866.	40.6
100126868^m	54.9	5724.	3524.	23.8
220544855	27.9	6469.	3266.	18.3
020208084^m	26.8	10051.	3733.	171.1
020302785	36.5	4505.	3359.	45.0
020218399	28.4	8951.	3562.	15.3
020212038	9.5	-99.	-99.	9.5
020234610	27.3	4783.	1065.	3.1
220567863	23.6	2128.	2769.	18.5
020188089	13.8	6788.	2720.	70.7
100123590	28.6	3769.	3396.	8.1

^{m}continuum manually adjusted.

Table D.3: Spectral parameters of the Fe II emission lines. complex.

Object ID	EW [Å]	SN
020239945	36.2	4.8
100343840	29.3	11.5
020212038	-0.8	7.0
020234610	62.2	2.6
220567863	37.5	14.3
100123590	45.6	8.7
020286836	85.5	39.7
020291309	118.4	3.3
000023526	17.1	8.9
100113463	27.5	37.6
220090821	38.6	18.8
100110223	14.3	5.3
020461459	47.7	17.7
100122852	18.7	33.3
100451895	15.5	14.0
100232259	43.2	8.9
020278210	$>$ 38.4	8.9
020254511	44.4	58.1
020177875	44.1	5.6
020232397	39.0	6.5
000033629	37.0	5.1
000073509	218.1	0.7
020114448	40.0	5.3
020120394	55.0	24.1
020466135	38.9	31.0
020147295	28.4	8.5
220566905	73.5	9.1
020210524^m	29.9	41.2
020176565	51.9	10.3
220568559	97.1	5.3
220609820	80.2	6.5

^{m}continuum manually adjusted.

Table D.4: Spectral parameters of the Mg II emission lines.

Object ID	EW [Å]	FWHM [km s^{-1}]	σ_l [km s^{-1}]	SN	$\log \frac{L_{BOL}}{1\ erg.s^{-1}}$	$\log \frac{M_{BH}}{M_\odot}$
020291309	154.3	3195.	3919.	3.5	44.6262	7.44
020159510	41.8	7831.	4483.	7.6	44.9934	8.48
000023526	72.1	14148.	5391.	5.4	44.8309	8.90
220082140	30.1	3223.	4455.	10.9	45.4235	7.95
100113463	43.8	5381.	3022.	13.5	45.4467	8.43
220090821	68.8	4321.	3109.	6.1	45.5021	8.26
100110223	75.8	6498.	4685.	3.1	45.1329	8.40
020461459	73.4	2983.	3467.	10.6	45.0927	7.67
100122852	27.4	5736.	2968.	10.2	45.7197	8.65
100451895	37.8	2476.	3787.	13.9	45.6664	7.84
100232259	72.6	5257.	2923.	5.5	45.2091	8.26
020278210	71.0	7907.	4648.	9.7	45.1026	8.56
020254511	71.5	3342.	4375.	14.3	45.3529	7.94
020177875	74.8	9127.	3444.	4.2	44.5949	8.37
020232397	80.2	2911.	4636.	5.8	44.4799	7.26
000033629	29.0	7882.	4398.	7.2	44.7514	8.33
000073509	94.4	7884.	3052.	1.6	44.1248	7.95
020114448	93.6	7463.	3498.	5.6	44.6190	8.20
020120394	68.0	4100.	5374.	22.1	45.4604	8.19
020466135	65.9	4150.	3472.	46.1	45.1797	8.03
020147295	56.7	5387.	3625.	9.0	44.5481	7.87
100290682	39.2	3002.	2443.	8.7	45.0067	7.62
220566905	25.9	1815.	2582.	6.5	44.6845	6.91
020210524	36.3	6388.	3485.	36.4	45.4140	8.56
220610034	40.8	3348.	3260.	16.8	45.3331	7.93
020176565	93.0	3361.	4189.	9.9	44.2762	7.27
220568559	72.9	4900.	3837.	7.5	44.6464	7.85
220609820	29.4	3394.	2905.	8.1	44.8975	7.67
020223153	49.0	7410.	2402.	3.4	45.1338	8.52
220041929[m]	> 37.4	-99.	-99.	53.6	-99	-99
020367106	92.6	7021.	4488.	7.8	44.5514	8.11
020463196	40.5	2563.	1224.	5.1	44.0302	6.86
020179225	39.2	8336.	4179.	20.4	44.6002	8.29
220554600	130.7	4844.	3752.	13.7	45.2421	8.21
020467628	66.1	2271.	4830.	12.1	45.0113	7.35
020258622	43.0	4253.	3558.	10.5	44.3131	7.51
220093875	54.0	3929.	5010.	5.0	44.7574	7.72
020165108	31.2	1977.	5143.	5.4	44.1926	6.70
020163018	36.1	3626.	1759.	7.2	44.3012	7.36
220542377	39.9	11261.	4699.	20.0	44.9629	8.78
220591287	53.2	2498.	4590.	3.1	44.3146	7.01

[m] continuum manually adjusted.

Table D.4: Spectral parameters of the Mg II emission lines ... continued.

Object ID	EW [Å]	FWHM [km s^{-1}]	σ_l [km s^{-1}]	SN	$\log \frac{L_{BOL}}{1\ erg.s^{-1}}$	$\log \frac{M_{BH}}{M_\odot}$
020118483	56.4	3723.	1002.	8.3	44.3004	7.38
000028880	46.6	3728.	7664.	6.9	44.2759	7.37
220613346	46.1	4075.	3592.	17.4	45.2696	8.08
100139500	45.7	4424.	3780.	14.9	45.0258	7.99
020213000	75.2	6533.	4383.	9.8	44.7933	8.19
100327652	74.8	3105.	2468.	1.9	44.2753	7.20
220081925	20.0	5177.	5387.	7.7	44.7075	7.93
020237445	64.7	6566.	4643.	6.3	44.4569	7.99
020086859	41.8	2792.	3155.	13.1	45.0971	7.61
100210521	78.4	3874.	3913.	15.8	44.7041	7.67
220567825	57.9	2833.	4270.	10.5	45.0189	7.57
100338914	87.0	4253.	4545.	13.0	45.5114	8.26
020364478	94.8	7447.	2000.	12.9	44.6123	8.20
020243922	49.1	3247.	4635.	22.4	44.8035	7.57
100241696	224.5	7610.	4735.	2.4	44.5640	8.19
220107230	112.2	7856.	5406.	6.6	44.5672	8.22
100190464	148.6	5896.	4885.	4.4	44.4619	7.90

^{m}continuum manually adjusted.

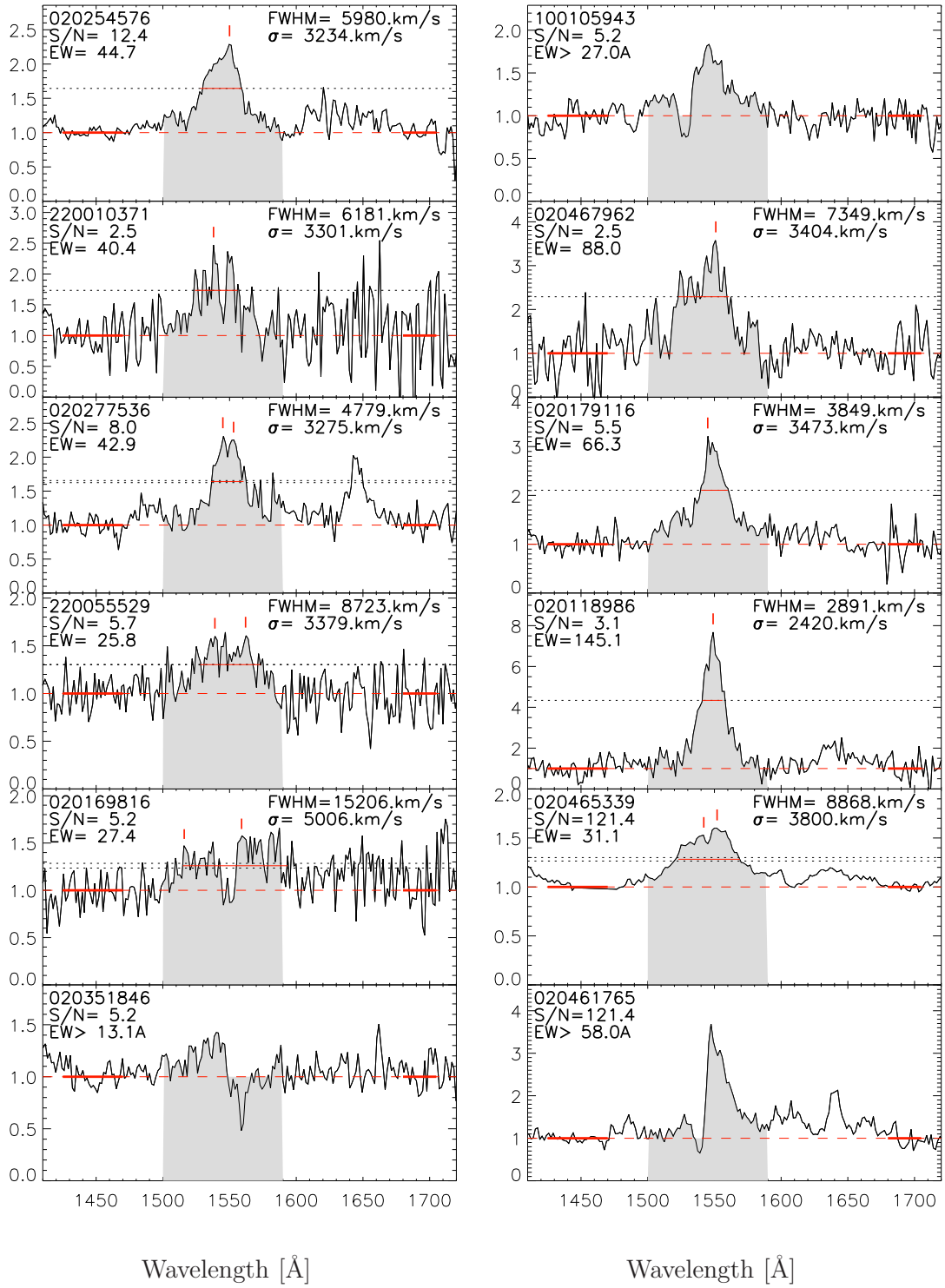

Figure D.1: Normalized C IV emission line profile. Spectra with the lowest S/N have been rebinned to 5 pixels.

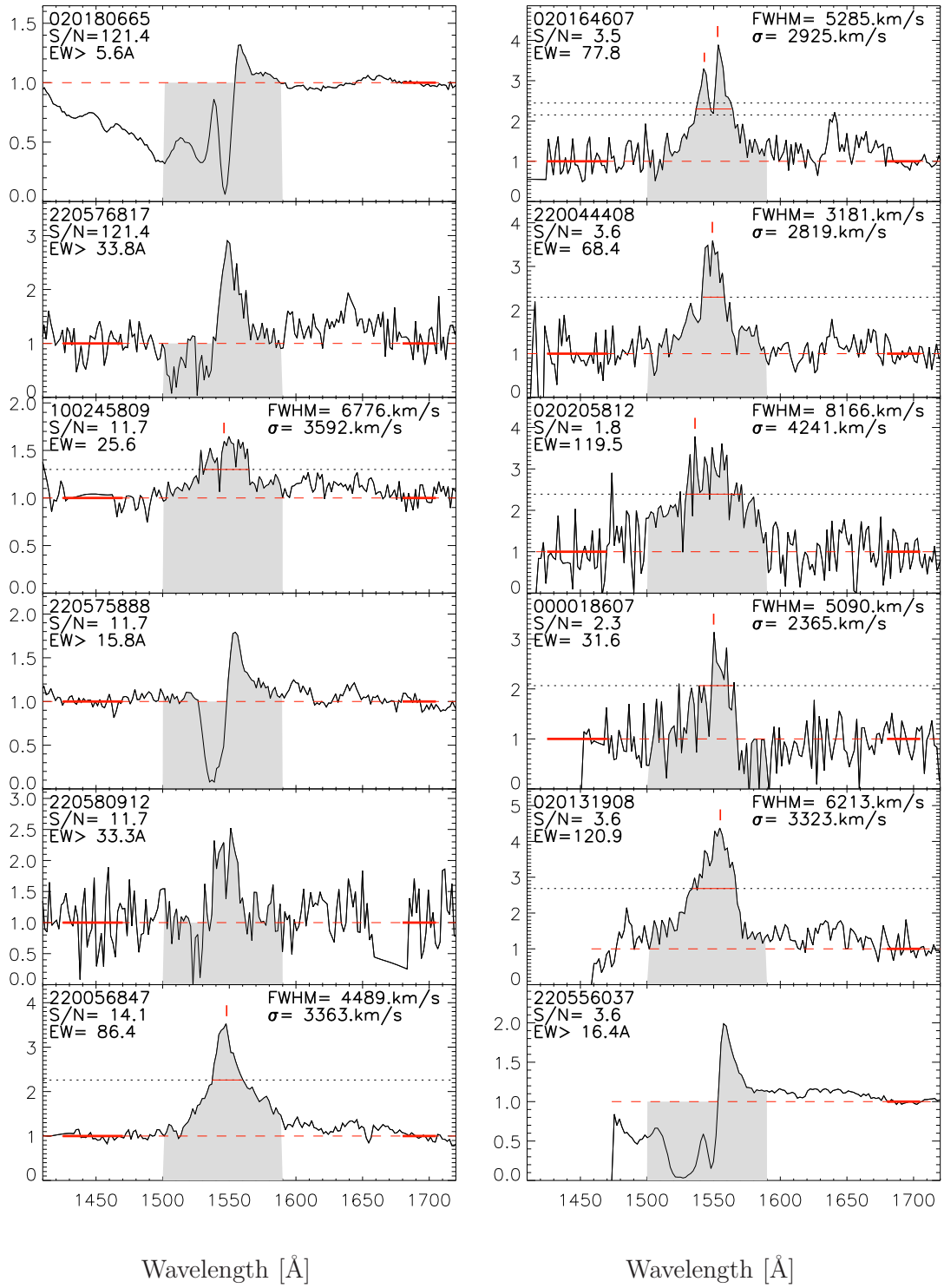

Figure D.1 Normalized C IV emission line profile. Spectra with the lowest S/N have been rebinned to 5 pixels.

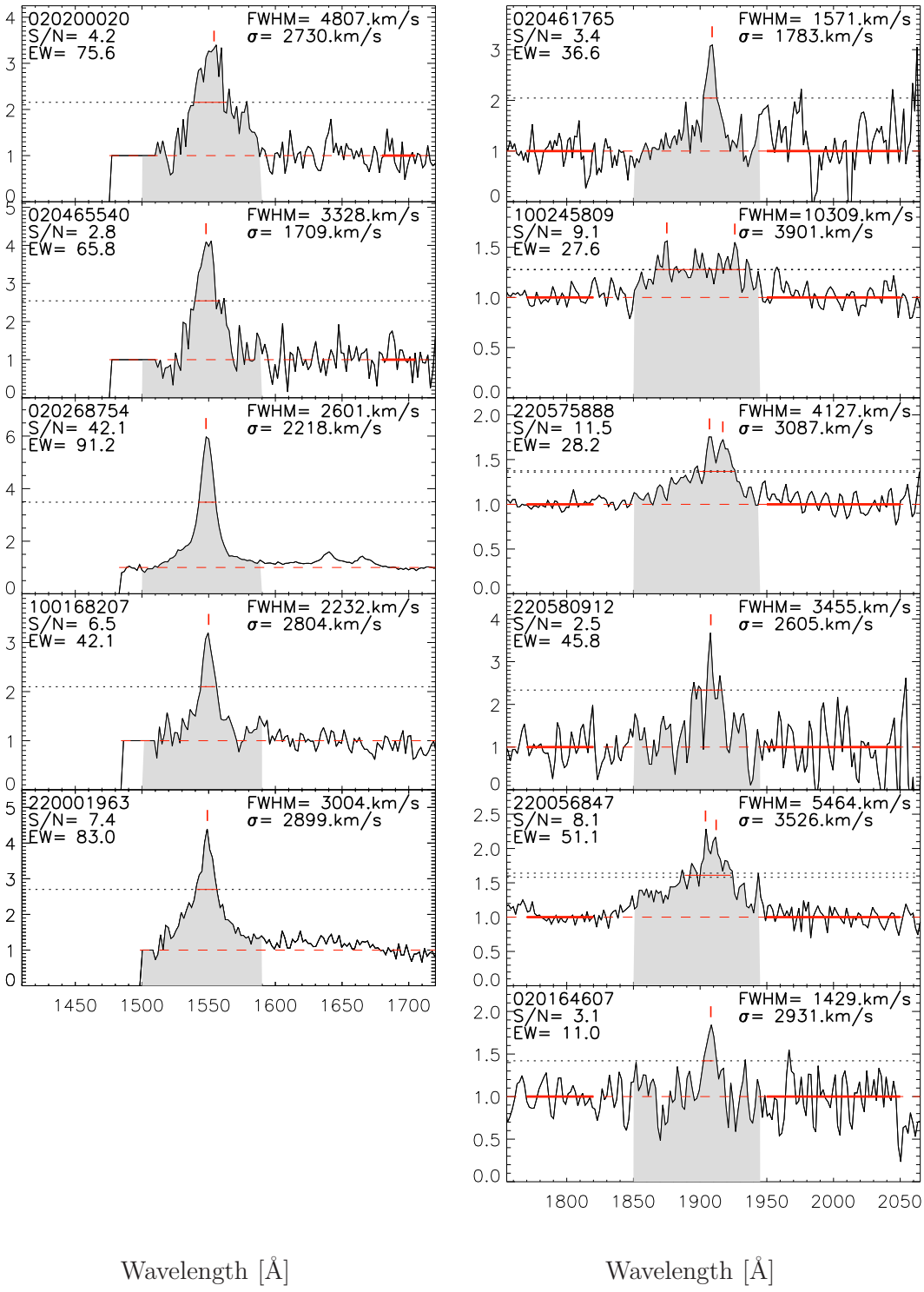

Figure D.1 Normalized C IV (left) and C III] (right) emission line profile. Spectra with the lowest S/N have been rebinned to 5 pixels.

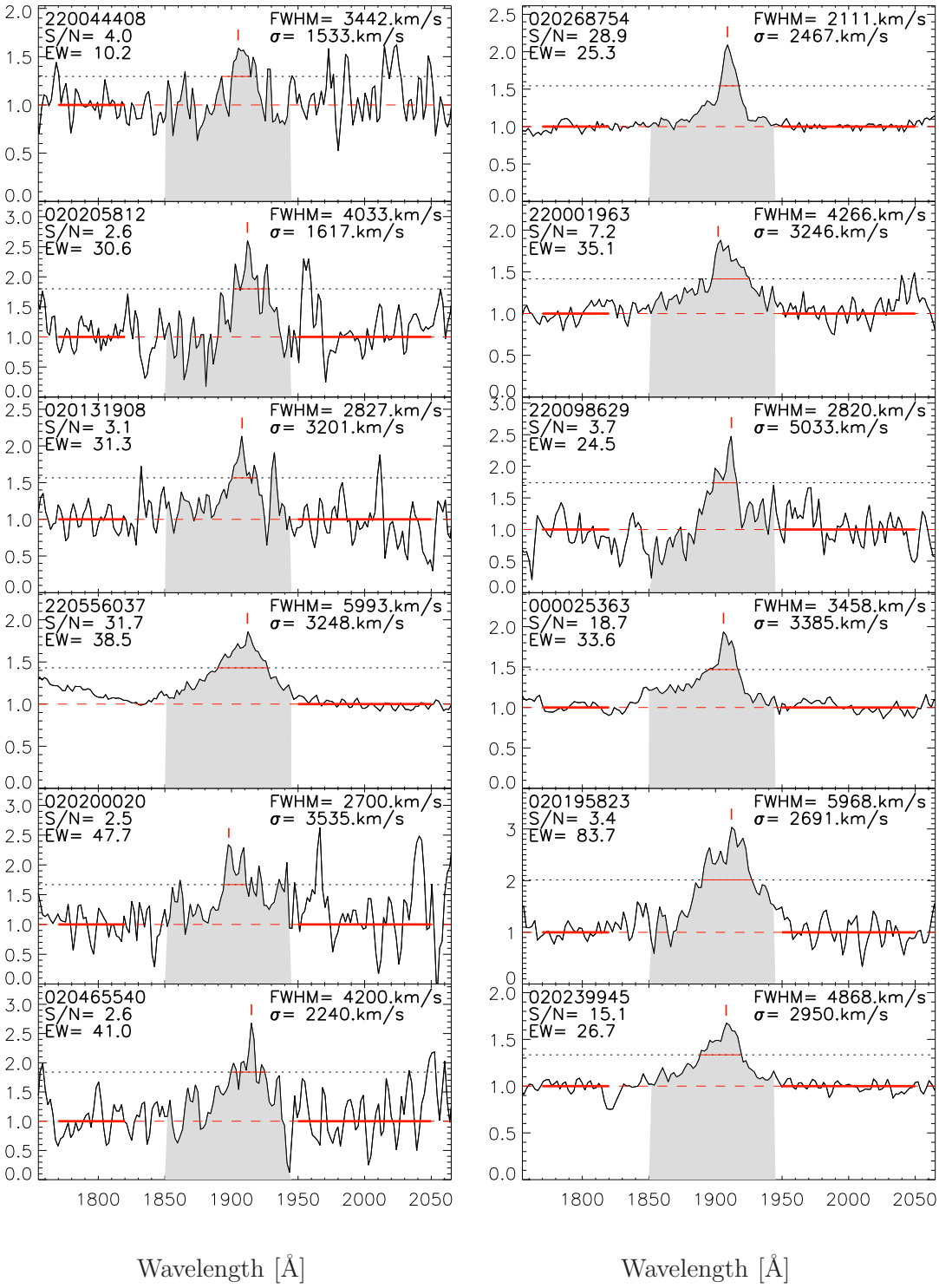

Figure D.1 Normalized C III] emission line profile. Spectra with the lowest S/N have been rebinned to 5 pixels.

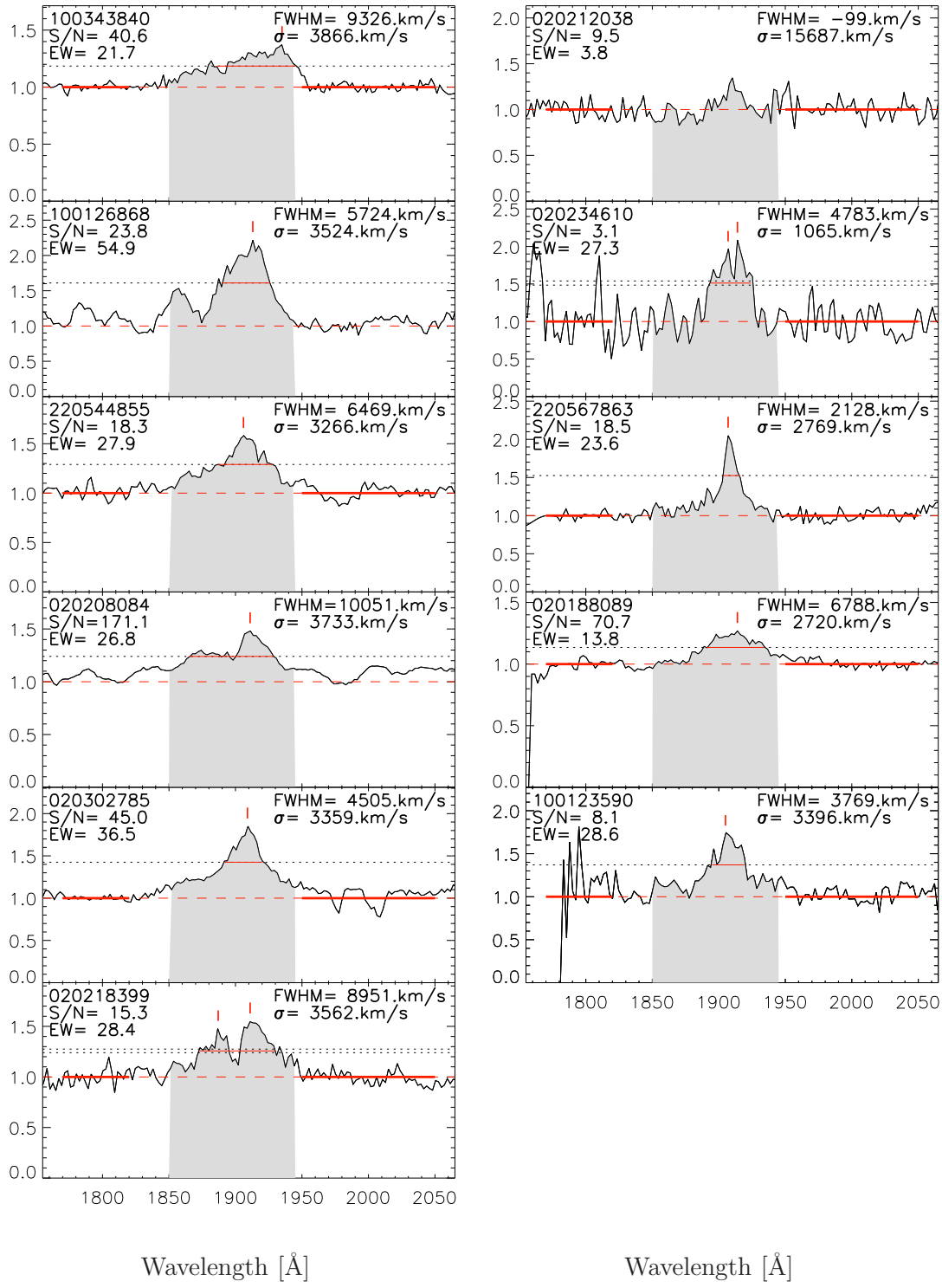

Figure D.1 Normalized C III] emission line profile. Spectra with the lowest S/N have been rebinned to 5 pixels.

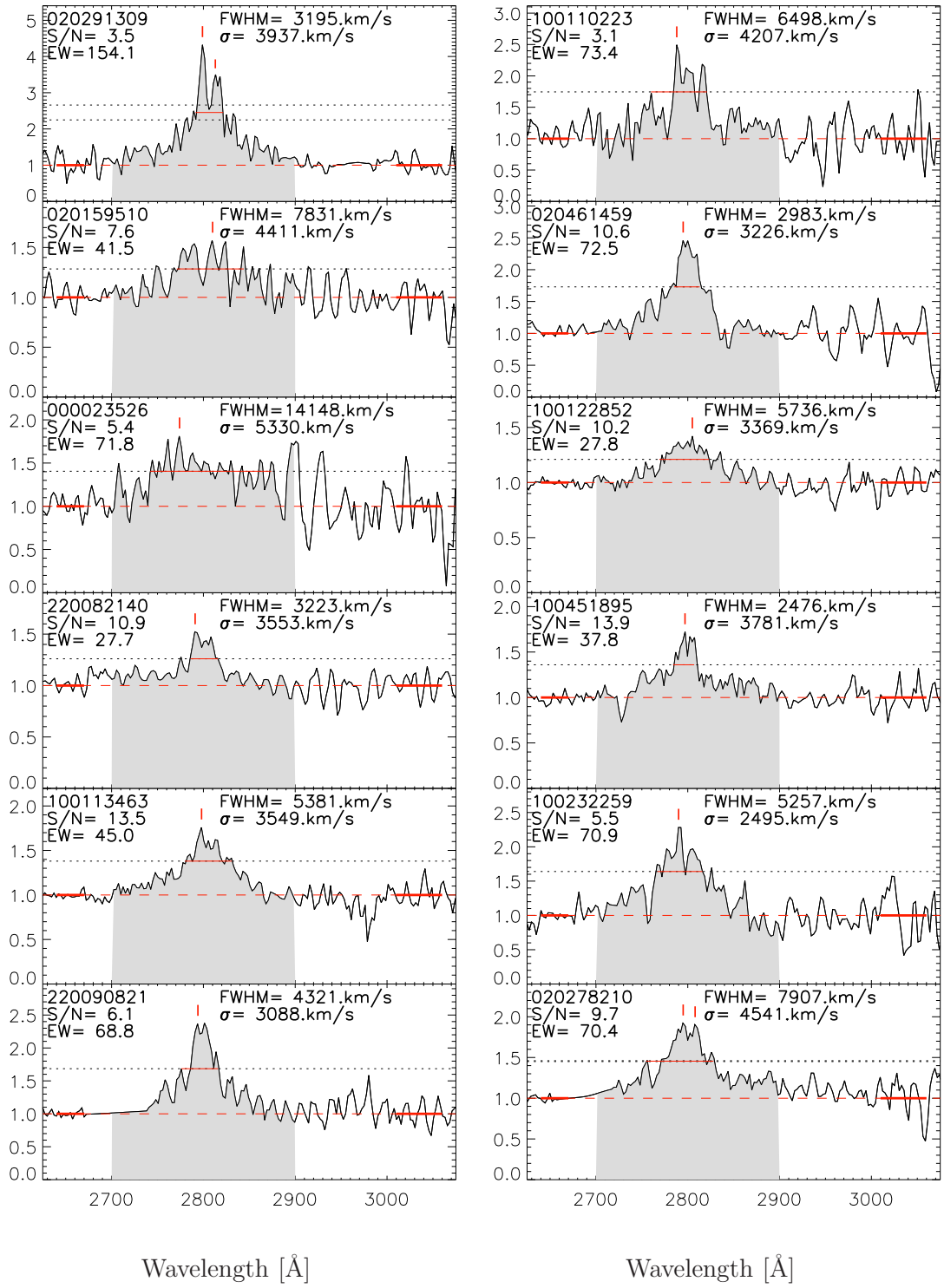

Figure D.1 Normalized Mg II emission line profile. Spectra with the lowest S/N have been rebinned to 5 pixels.

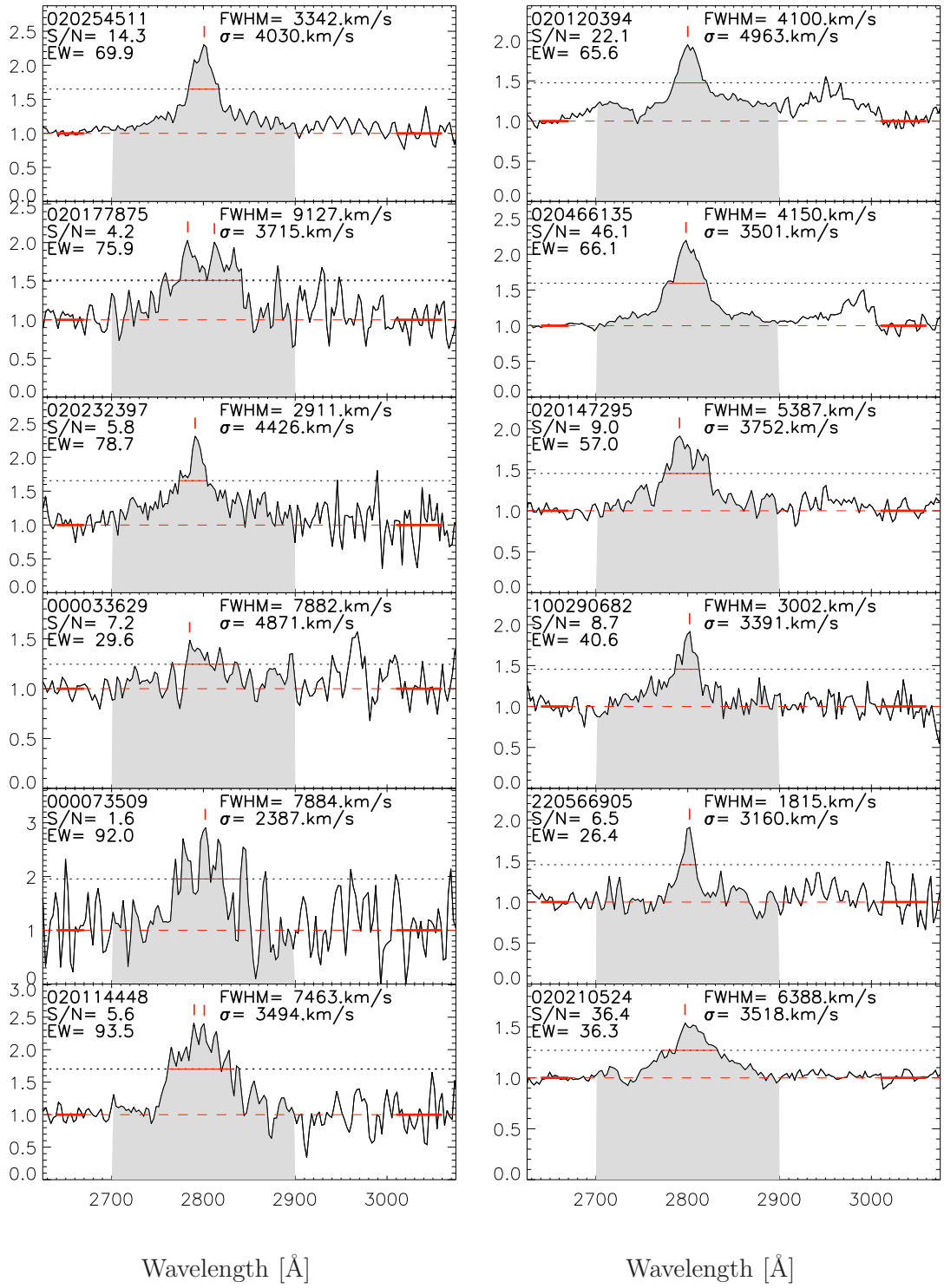

Figure D.1 Normalized Mg II emission line profile. Spectra with the lowest S/N have been rebinned to 5 pixels.

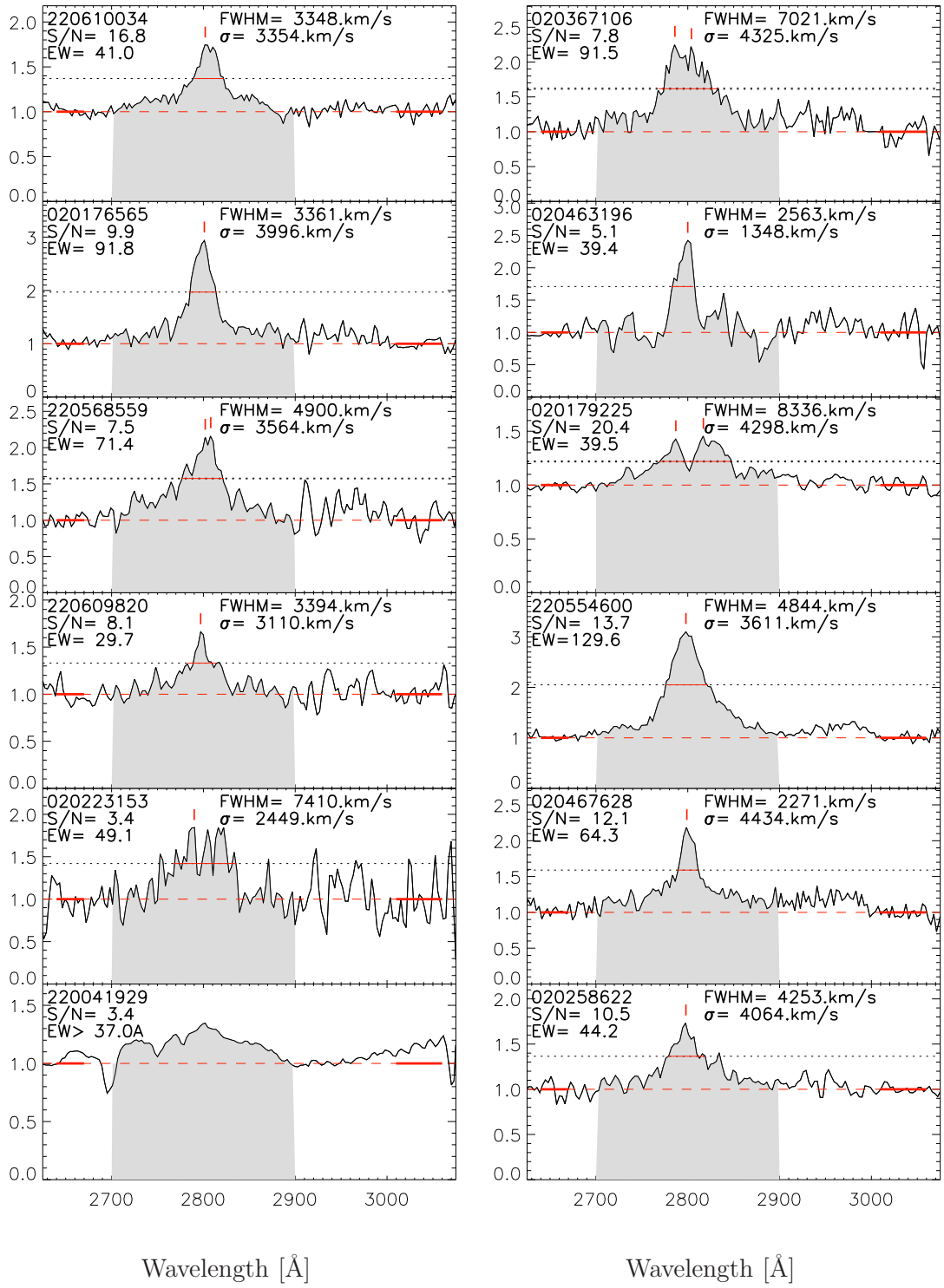

Figure D.1 Normalized Mg II emission line profile. Spectra with the lowest S/N have been rebinned to 5 pixels.

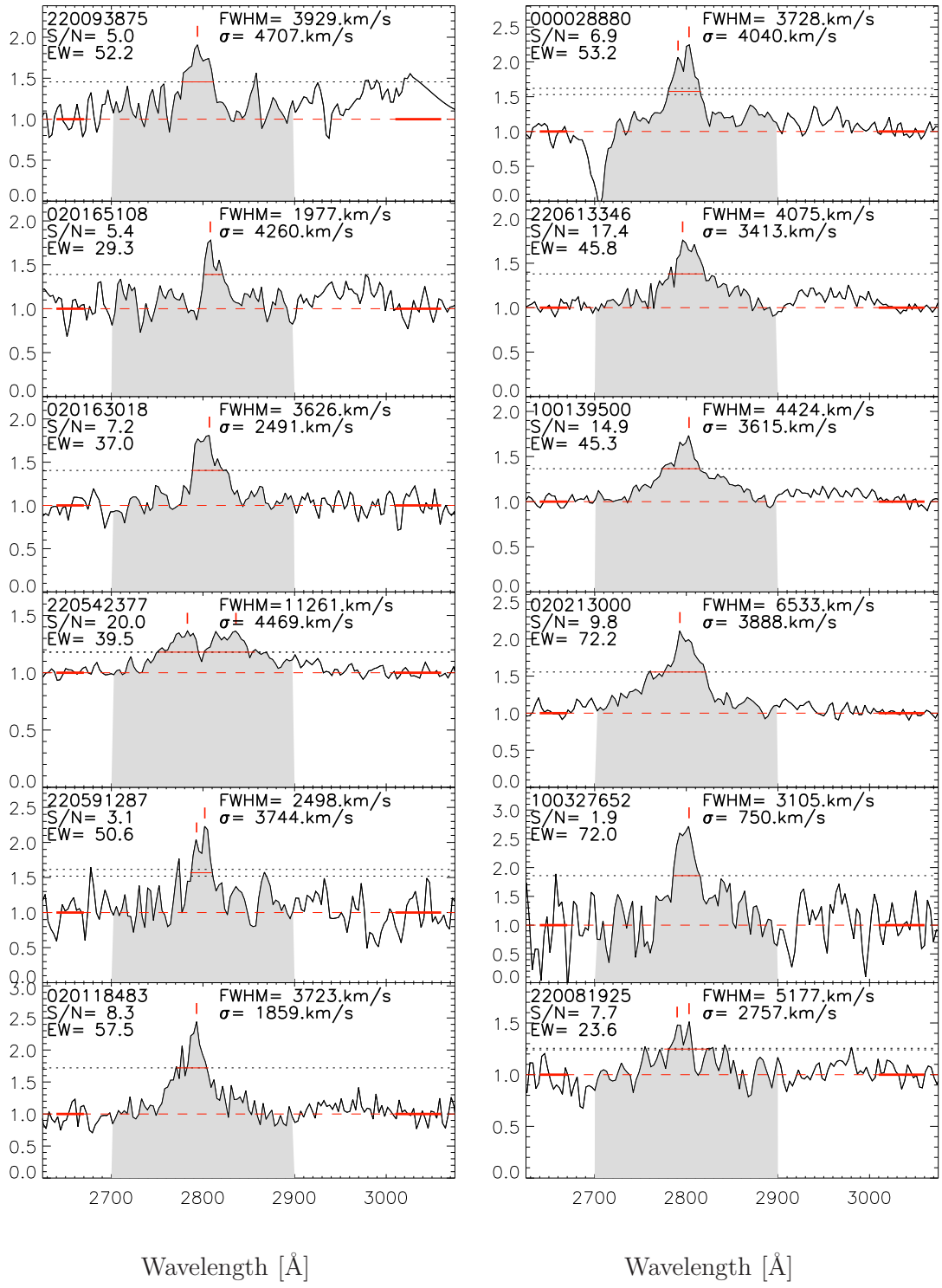

Figure D.1 Normalized Mg II emission line profile. Spectra with the lowest S/N have been rebinned to 5 pixels.

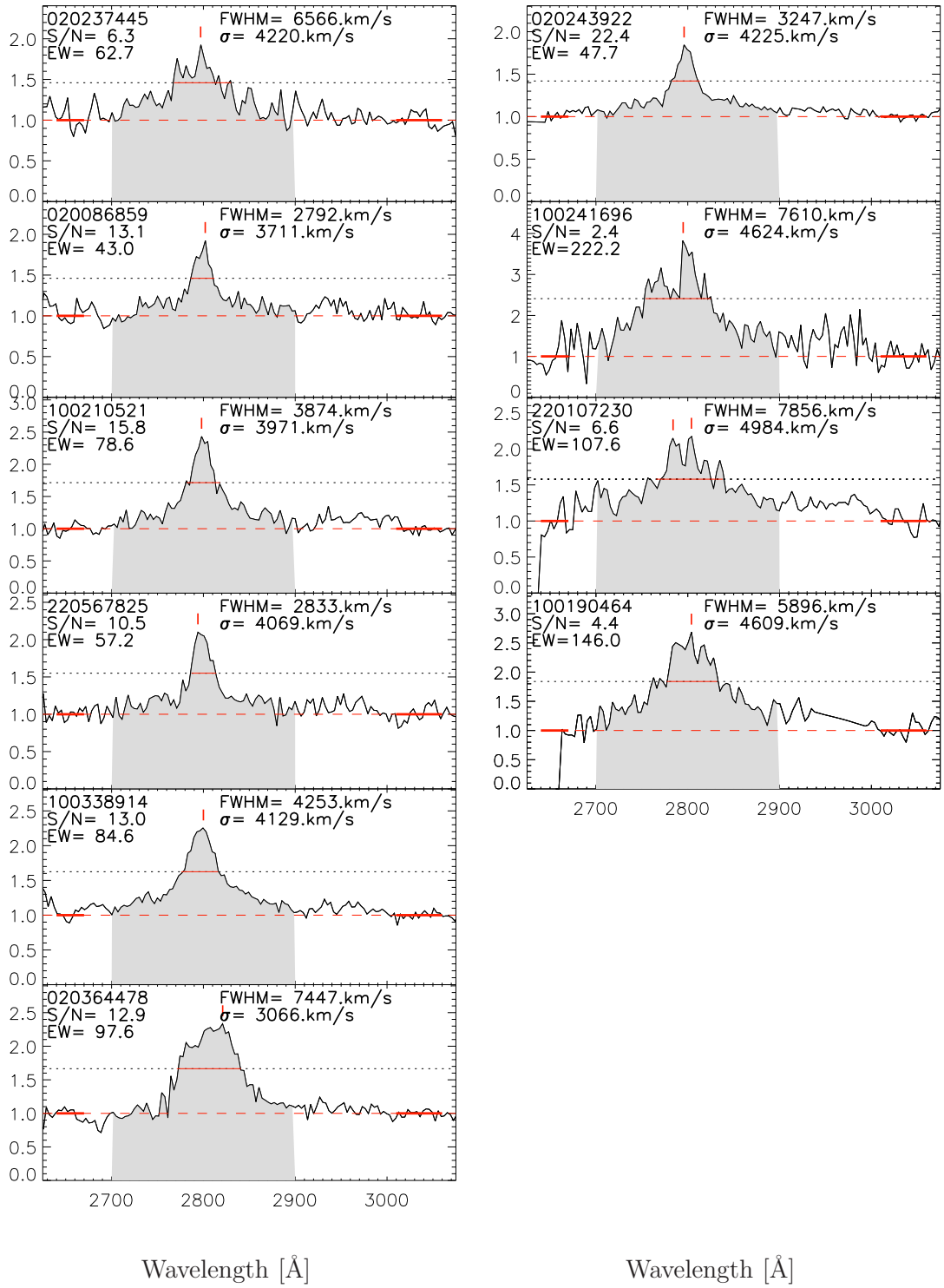

Figure D.1 Normalized Mg II emission line profile. Spectra with the lowest S/N have been rebinned to 5 pixels.

Refereed papers

As a first author:

- **The VIMOS VLT Deep Survey: the faint type-1 AGN sample**, I. Gavignaud, A. Bongiorno, S. Paltani, G. Mathez, G. Zamorani, P. Møller, J.P. Picat, V. Le Brun, B. Marano, O. Le Fèvre, and 43 co-authors, 2006, A&A, 457, 79-90

As a co-author:

- **The VIMOS-VLT Deep Survey. Luminosity dependence of clustering at** $z \simeq 1$, Pollo, A. et al. (48 co-authors), 2006, A&A, 451, 409
- **Compact structures in the CDFS: dynamical state and content**, Adami, C. et al. (49 co-authors), 2005, A&A, 443, 805
- **The VIMOS VLT Deep Survey - Evolution of the non-linear galaxy bias up to z=1.5**, Marinoni et al. (49 co-authors), 2005, A&A, 442, 801
- **The VIRMOS deep imaging survey. IV. Near-infrared observations**, Iovino et al. (51 co-authors), 2005, A&A, 442, 423
- **The VVDS-VLA Deep Field. II. Optical and near infrared identifications of VLA** $\mathbf{S_{1.4GHz}} > 80\mu$**Jy sources in the VIMOS VLT Deep Survey VVDS-02h field**, Ciliegi et al. (49 co-authors), 2005, A&A, 441, 879
- **A large population of galaxies 9 to 12 billion years back in the history of the Universe**, Le Fèvre et al. (48 co-authors), 2005, Nature, 437, 519L
- **The VIMOS VLT Deep Survey. Computing the two point correlation statistics and associated uncertainties**, Pollo et al. (49 co-authors), 2005, A&A, 439, 887

- **The VIMOS VLT Deep Survey. The evolution of galaxy clustering to $z \sim 2$ from first epoch observations**, Le Fèvre et al. (49 co-authors), 2005, A&A, 439, 877
- **The VIMOS-VLT Deep Survey: Evolution of the galaxy luminosity function up to $z = 2$ in first epoch data**, Ilbert et al. (47 co-authors), 2005, A&A, 439, 863
- **The VIMOS VLT Deep Survey. First epoch VVDS-Deep survey: 11564 spectra with $17.5 < I_{AB} < 24$, and the redshift distribution over $0 \leq z \leq 5$**, Le Fèvre et al. (48 co-authors), 2005, A&A,439,845
- **The GALEX-VVDS Measurement of the Evolution of the Far-Ultraviolet Luminosity Density and the Cosmic Star Formation Rate**, Schiminovich et al. (63 co-authors), 2005, 619L, 47
- **The GALEX VIMOS-VLT Deep Survey Measurement of the Evolution of the 1500 Å Luminosity Function**, Arnouts et al. (64 co-authors), 2005, ApJ, 619L, 43A
- **The VIMOS VLT Deep Survey. Public release of 1599 redshifts to $I_{AB} \leq 24$ across the Chandra Deep Field South**, Le Fèvre et al. (49 co-authors), 2004, A&A, 428,1043

Abstract

In the recent years, majors surveys have been collecting several ten thousands of QSO spectra, demonstrating the high efficiency of optical color pre-selection techniques and providing a new level of statistics in describing the properties of the QSO population. The drawback of these pre-selection techniques is that some subset of the underlying QSO population may be under-represented in these survey thereby possibly biasing our current understanding.

This ph D thesis is devoted to the study of the properties of the faint population of type-1 AGN. For this purpose we use a spectroscopic sample of 130 broad line AGN, extracted from a large galaxy survey, the VIRMOS VLT Deep Survey (VVDS). This AGN sample present two-major interests: (1) a selection function free of pre-selection biases, which enables us to census the population of optical type-1 AGN from redshift 0 to 5 in a coherent way; (2) a very faint limiting magnitude (respectively $I_{AB} = 22.5$ and $I_{AB} = 24$ for the *wide* and *deep* sample) that was previously reached for catalogs of this size only by photometric studies.

Our measured surface density ($\sim 472 \pm 48$ BLAGN per square degree with $I_{AB} \leq 24$) is significantly higher than that of any other optically selected sample of BLAGN with spectroscopic confirmation.

Because of the contamination of the AGN light by their host galaxy at the faint magnitude explored by our sample, we observe that a significant fraction of AGN in our sample would be missed by the usual UV excess and morphological criteria used for the pre-selection of optical QSO candidates.

This contamination is as well seen in our composite spectrum. We observe an extension of the anti-correlation between luminosity and equivalent-width of high-ionization emission-lines to the fainter luminosities probed by our sample for a given redshift (Baldwin effect).

The luminosity function derived from this sample shows a relatively steep faint end at low redshift ($1 < z < 1.5$), and in contrast a flatter faint end at higher redshifts ($z > 1.5$). This behaviour fit into the picture of an anti-hierarchical growth of galactic black holes, as it was first suggested by X-ray selected AGN studies.

Preliminary results on the black hole mass estimates of our objects suggest that most of faint optical AGN are triggered by intermediate-mass galactic black-holes ($\sim 10^8 M_\odot$) accreting at relatively low Eddington rates ($\lesssim 10\%$).

Résumé

Ces dernières années les principaux relevés cosmologiques ont collectés plusieurs dizaines de milliers de spectres de noyaux actifs de galaxies (connus aussi sous l'abréviation anglaise AGN), illustrant ainsi la grande éfficacité des techniques de pré-sélections optiques de candidat AGN. Ils ont ainsi permis une étude statistique détaillée de la population d'AGN. Le revers de ces techniques de pré-sélection est que certaines catégories de la population globale des AGN optiques sont peut-être sous-représentées dans ces échantillons, biaisant notre compréhension actuelle de l'évolution de ces objets.

Cette thèse de doctorat est dédiée à l'étude des propriétés des AGN de type 1 de faible luminosité. Dans ce but nous utilisons un échantillon spectroscopique de 130 AGN à raies d'émission larges, extrait d'un grand relevé de galaxie : le VIRMOS VLT Deep Survey (VVDS). Cet échantillon présente un intérêt unique, de part la simplicité des critères de pré-sélection de ces objets (une simple limite en magnitude) ainsi que par la profondeur en magnitude atteinte : il fournit d'une part un aperçu des propriétés des AGN de type 1 à des magnitudes encore peu explorées spectroscopiquement (les AGN étudiés ici sont jusqu'à cent fois plus faibles que ceux du SDSS) et il permet d'autre part de quantifier les biais qui seraient introduits par des critères classiques de sélection.

Nous mesurons une densité sur le ciel d'environ 470 AGN par degré carré à notre magnitude limite ($I_{AB} = 24$). Une fraction importante des AGN que nous observons ne serait pas sélectionée par les techniques de sélections morphologiques et d'excès d'UV classiquement appliquées. Nous attribuons cet effet à la contamination de nos AGN par leur galaxie hôte, vue leur faible luminosité. La fonction de luminosité des AGN montre qu'il y a relativement plus d'AGN de faible luminosité à bas redshift qu'á plus grand redshift. Cette observation corrobore le scénario de croissance anti-hierarchique de trous-noirs galactiques suggéré par les echantillons d'AGN sélectionnés en rayons-X. Finalement nous nous sommes intéressés à la nature des trous noirs qui sont à l'origine de nos AGN. S'agit-il de petits trous noirs galactiques ou bien, au contraire, de trous noirs de grandes masses accrétant faiblement ? Nos résultats, encore préliminaires, suggèrent que nos AGN correspondent en moyenne à des trous noirs galactique de masses intermediaires ($\sim 10^8 M_\odot$) accrétant à des taux d'Eddington modeste ($\lesssim 10\%$).